Redesign of the Micromechanical Flying Insect in a Power Density Context

Erik Edward Steltz

Electrical Engineering and Computer Sciences
University of California at Berkeley

Technical Report No. UCB/EECS-2008-56
http://www.eecs.berkeley.edu/Pubs/TechRpts/2008/EECS-2008-56.html

May 19, 2008

Redesign of the Micromechanical Flying Insect in a Power Density Context

by

Erik Edward Steltz

B.S. (The Pennsylvania State University) 2002
M.S. (University of California, Berkeley) 2004

A dissertation submitted in partial satisfaction of the
requirements for the degree of
Doctor of Philosophy

in

Engineering-Electrical Engineering and Computer Sciences

in the

GRADUATE DIVISION
of the
UNIVERSITY OF CALIFORNIA, BERKELEY

Committee in charge:
Professor Ronald S. Fearing, Chair
Professor Seth R. Sanders
Professor Robert Dudley

Spring 2008

The dissertation of Erik Edward Steltz is approved:

Chair Date

Date

Date

University of California, Berkeley

Spring 2008

Redesign of the Micromechanical Flying Insect in a Power Density Context

by

Erik Edward Steltz

Abstract

Redesign of the Micromechanical Flying Insect in a Power Density Context

by

Erik Edward Steltz

Doctor of Philosophy in Engineering-Electrical Engineering and Computer Sciences

University of California, Berkeley

Professor Ronald S. Fearing, Chair

The Micromechanical Flying Insect (MFI) project aims to create a 25 mm, 100 mg flapping micro air vehicle. A maximum of 1400 μN of lift force by a single transmission/wing of the MFI has been produced on a test stand with oversized actuators. To achieve takeoff on a lightweight composite airframe, this high thrust must be produced using at-scale actuators. Previous attempts at MFI takeoff have suffered from low flapping amplitude and hence low thrust, which can be seen as a lack of power delivered to the wing. Power density of the actuators and structure used to drive the wing is of critical importance, especially for flapping flight. In this work, a design framework using power density as a metric is formulated not only for the MFI but for millirobots in general. The power density of an MFI 10 mg piezoelectric bending actuator is directly measured for the first time with a custom dynamometer and found to be 467 W/kg at 275 Hz. It is mathematically shown that adopting an actuator geometry that places a uniform strain profile on the piezoelectric element rather than a bending geometry can provide 2.6 times the energy delivered for the same volume of piezoelectric material. A new thorax (actuator/transmission) design is introduced which couples a single, uniform strain flextensional actuator to 2 wings. A key concept of the thorax design is using carbon fiber side beams near their singularities to provide the necessary transmission ratio. Two

iterations of flextensional MFI designs are presented, finally obtaining 42^o of total wing stroke at 225 Hz. An important limitation of the structure is serial compliance in its transmission stages, which absorbs useful motion preventing proper power transmission from the actuator. Despite the low stroke amplitude stroke due to serial compliance, 37.5 mg of thrust was produced from the design using all at-scale components. Future improvements to the new MFI structure design are discussed, which through iteration can eventually yield an autonomous flying vehicle.

Professor Ronald S. Fearing
Dissertation Committee Chair

To those whom I have lost while in my graduate studies: my grandfather Lawrence and my best childhood friend Joel Withers. You will always be in my thoughts.

Contents

List of Figures

List of Tables

Acknowledgments

There are almost too many individuals to name that have helped me throughout my graduate career. First and foremost I must thank my advisor, Professor Ron Fearing. His constant optimism, perseverance, and openness to new ideas has made my graduate research constantly exciting and rewarding. I hope to have the privilege of working with him throughout my career. Along with Ron, other lab members were very helpful especially when I first joined the lab, including Rob Wood, Srinath Avadhanula, and Ranjana Sahai. Also thanks to Professor Richard Groff who helped with various research challenges and Aaron Hoover whom I have had the privilege of working with recently. I would like to thank Michael Seeman and Prof. Seth Sanders for designing the hybrid boost/switched capacitor circuit for driving piezoelectric actuators in Appendix B.

Thanks to truly constructive and supportive thesis committee members, Prof. Seth Sanders and Prof. Robert Dudley (and of course Prof. Fearing) whose comments and suggestions made the thesis much stronger. Thanks also to the Army Research Lab who sponsored my first three years of graduate study through a National Defense Science and Engineering Graduate Fellowship, and NSF which funded the research thereafter through Grant No. IIS-0412541.

To my fellow graduate students and roommates, notably: Dan Ceperley, Dan Hazen, Joanna Lai, Elaine Cheong, and Dave Nguyen. You have all helped me not only stay sane in stressful times but also enjoy the best times. Your continued friendship is truly valued.

Finally, to my family and loved ones. To my parents Edward and Linda, you have been thoroughly supportive of my graduate studies even if some of my decisions were by your standards unorthodox. Your pressure to eventually "get a real job" has kept me properly motivated; also to my sister Nicole and her many care packages. You balanced me in the opposite direction to "stay in school as long as possible." And last but certainly not least to my love Sarah; your unwavering love and support has probably had the most influence on my continual maturation as a person.

Chapter 1

Introduction

Millirobots (robots <20 g) have great potential for search and rescue, ad hoc sensor networking, or reconnaissance among other fields. Dynamic millirobots, or those with dynamic mobility like animals in nature as opposed to slow static locomotion, enable even more interesting behaviors and the ability to operate in a wide variety of environments.

The Micromechanical Flying Insect (MFI) is one such dynamic millirobot. The MFI is a 25mm, 100mg flapping air vehicle. Consisting of only small amounts of material, the MFI could be manufactured very inexpensively, meaning a swarm of flyers could be used to address the problem at hand without need for each vehicle to perform perfectly. The goal of this work is to improve the MFI to achieve autonomous flight; specifically, the power plant is redesigned to achieve a greater thrust to weight ratio. By moving the MFI design from bending piezoelectric actuators to axially displacing piezoelectric elements, the overall power transmitted to the wing can be increased. With proper changes to wing kinematics, lift forces can be improved, leading to an autonomous, mobile flying platform.

1.1 Underlying Aerodynamic Theory

A flapping wing micro air vehicle (MAV) can offer unmatched maneuverability for use in cluttered or indoor environments. Insects themselves can take off backwards, fly sideways, and even land upside down. Small flapping wing MAVs such as the MFI can hopefully not only maneuver like insects, but with characteristic dimensions in only the millimeter range can operate virtually unnoticed.

The aerodynamic mechanisms allowing the high lift forces and maneuverability of insect flight were first addressed in hawkmoths by Ellington in [17]. Later, Dickinson addressed and modeled three separate aerodynamic lift mechanisms in fruitflies [12]. These mechanisms have been named 1) delayed stall, 2) rotational lift, and 3) wake capture. Delayed stall is a leading edge vortex on the wing due to a high angle of attack that would eventually cause the wing to stall. However, before stall occurs, a large increase in lift force is observed. Since the wing soon reverses direction, the leading edge vortex does not separate (stall). Rotational lift occurs when the wing is simultaneously translating and rotating; the effect is similar to top spin on a tennis ball. Finally, wake capture occurs when the wing reverses direction; since it has rotated, when the wing now meets the vortex that was attached to the wing during the previous stroke, a significant inertial lift spike is observed.

1.2 MAV Platforms

Several researchers have created small flapping MAVs. Some of these platforms, dubbed ornithopters (meaning that they have flapping wings), fly similar to birds in which the wings function as static lifting surfaces similar to conventional airplanes. Flapping is used along with changing angle of attack to generate forward thrust. One of the first flapping MAVs with static lifting surface wings was Caltech/Aerovironment's microbat [49]; this MAV indeed flew like a bird though some claims of wake capture have been made for the vehicle. Vehicles that flap like large birds are generally not

capable of hovering; forward velocity is necessary to maintain flight.

Researchers at Delft University of Technology in the Netherlands have created a micro UAV they have termed DelFly [7]. The latest version, Delfly II is a 30cm device and can fly horizontally at 15m/s but can also hover [33]. Delfly's performance is certainly noteworthy but with such a large vehicle, constrained indoor flight is still difficult due to maneuverability issues. Kawamura has made a miniaturized, 2.3g version of DelFly [40] capable of forward flight and hover. The vehicle flaps at 35Hz (when hovering) and, like DelFly, utilizes a clap-and-fling mechanism for increased lift. To the author's knowledge, this vehicle is the smallest and highest performance untethered UAV.

On the insect scale, Robert Wood at Harvard has used MFI technology to achieve takeoff of a tethered 60mg flapping vehicle [67]. Wood's vehicle used the SCM (Smart Composite Microstructures) process [70] and flapped at approximately 110Hz, taking off on guide posts for stability. Though the vehicle was tethered and uncontrolled, it is the first vehicle of its size to produce thrust greater than its weight.

1.3 Previous MFI Technology

The MFI has been an active research project since 1998 and has seen many design revisions but has yet to achieve untethered takeoff. The earlier MFI version before the work herein utilized piezoelectric bending actuators to drive two independent flapping wings. Piezoelectric actuators were chosen for their high bandwidth, light weight, and ease of integration into the MFI platform. However, piezoelectric actuators have very small displacements, so their motion must be amplified to achieve adequate wing flapping amplitude. The original goal of the MFI project wing trajectory was 120^o of flapping at 150Hz.

To amplify the piezoelectric actuator motion, fourbar linkages were utilized, fabricated with the SCM process that uses composites as stiff links and polymers as flexure materials. Two actuators drive each wing (shown in Fig. 1.1 as δ_1 and δ_2); both are amplified via identical fourbar linkages.

The output of the two fourbar linkages (θ_1 and θ_2 in the Figure) is connected via a differential. If the two actuators driving the wing move in phase, pure flapping is achieved. If the actuators move out of phase, wing rotation due to the spherical five bar mechanism of the differential is achieved (angle ψ in the diagram). A full kinematic and dynamic analysis of the mechanism is presented in [2].

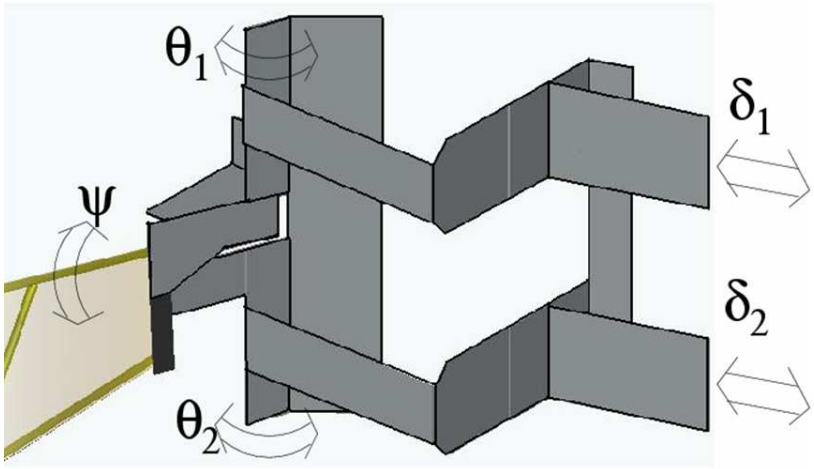

Figure 1.1: Diagram of mechanical wing transmission.

This basic design for the MFI has been iterated on since 1998. By 2006, the highest lift force produced from the design was 1400 μN from a single wing [55]; this device used oversized actuators on a plastic test base (not an airframe). A prototype of the MFI from 2006 is shown in Fig. 1.2.

1.4 Results and Problems with Current Technology

Although the absolute force produced by the MFI is significant, there are several known problems with the design. Most importantly, when the full 4DOF fly is manufactured with scaled, 10mg actuators, wing amplitude suffers significantly compared with the large test base structure that produced high lift. Consequently, it has never taken off, even tethered. A shortage of power could be from either losses in the mechanical structure or poor performance of the scaled actuators;

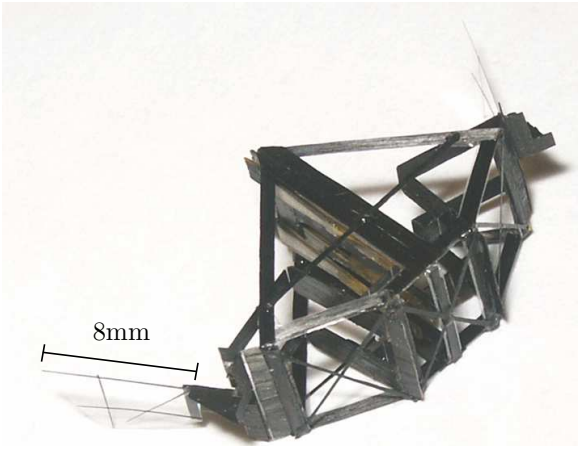

Figure 1.2: MFI prototype from 2006.

the determination of this is addressed in this thesis.

Another secondary problem is that the two wings are independent resonant systems. Considering the structure is assembled by hand, the resonant frequencies of the two wings are very difficult to match. The resulting structure has to operate at a drive frequency averaged from the resonant frequencies of the two wings; this results in less than optimal wing flapping angle for both wings. Finally, the airframe for the structure is not adequate to completely isolate effects from one wing to the other. When trying to control wings independently, some of the control action from one wing influences the other due to airframe vibrations, which makes control very difficult.

1.5 Contributions and Outline

The contributions of this work are as follows:

- **Power density framework for millirobots** - Most millirobots in the literature have limited mobility because they were not optimized in terms of power density of the robot. Chapter 2 presents a framework for designing millirobots in terms of power density of the power plant of the robot. Several actuators, batteries, and drive electronics are compared to show the strength and weakness of each actuation method and how to choose a technology given a locomotion

method.

- **Measurement of PZT power output** - Although estimated from DC measurements in previous work [73], the actual power output for the optimized piezoelectric bending actuator of the MFI is not known. The limited flapping amplitude and hence inadequate power delivered to the wing in the MFI platform has brought the DC extrapolations of power density into question. In Chapter 3, a custom dynamometer is constructed and used to measure the actual power output of the miniature bending actuators. To the author's knowledge, this is the first high frequency measurement of real power output from a piezoelectric bending actuator.

- **Redesign of the MFI** - In the context of the power density framework and results of the dynamometer power output measurements, the entire MFI platform is redesigned in Chapter 4 using axial rather than bending mode PZT actuators. A total kinematic model of the redesigned structure is presented here.

- **Construction of the Redesigned MFI** - In Chapter 5 new construction technology is developed and used to realize the design proposed in Chapter 4. Results of the first design iteration are used to propose a revision which is likewise constructed and tested. Flapping amplitude and frequency results are presented with a measurement of lift from the structure.

- **Improved Manufacturing Processes for SCM** - In Appendix A improved manufacturing processes revolving around vacuum bagging composite parts are presented, allowing the newest MFI design to utilize kapton flexures and carbon fiber with lower dissipation than previous structures. This is an enabling technology for the MFI redesign.

- **Autonomous Millirobot Power and Control Board** - Finally in Appendix B miniature power and control electronics are presented to enable autonomy for mobile millirobots. Lightweight power supplies for piezoelectric and shape memory alloy driven millirobots are presented along with a processing, sensing, and control board with wireless transmission capability.

The MFI has not been significantly redesigned for over 5 years, when it was moved to composite materials. The MFI redesign analyzed and presented here is a significant departure for the vehicle considering that it does not utilize a bending actuator because of power losses; instead it uses a straight axial actuation scheme. This requires significant changes to all the linkages of the design. The final revision of the design as is laid out in Chapter 5 is shown in Fig. 1.3.

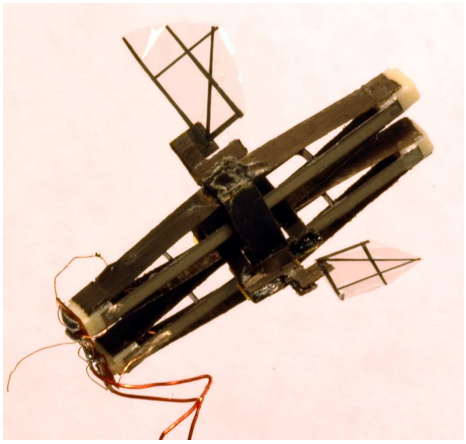

Figure 1.3: Revised MFI using an extensional PZT actuator.

Chapter 2

Power Density Framework for Millirobots

Many biologically inspired mobile millirobots have been built at UC Berkeley and elsewhere, such as walking/crawling millirobots [24][15][75][41][27], flying millirobots [66][33][10], swimming millirobots (numerous but a representative design is in [6]), or more conventional wheeled millirobots [8]. Often, the robots do not carry onboard power or processing and the designers are therefore not concerned with overall efficiency or power use. However, if the robot is to be untethered, power use and efficiency are of tremendous concern. For those few robots that are untethered, most experiments result in only modest success with robots moving statically (as opposed to dynamically) as in [51][41], though one exception is the flying and hovering 2.3g robot of Kawamura et al in [40]. For the work here, the focus is on millirobots that can locomote in a dynamic way more like animals in nature.

Here, a novel design metric for dynamic mobile millirobots is presented (it also applies to larger robots). Millirobots are often built around their actuation technology, which is chosen first. Instead, it is argued that the "power plant" of the robot is an integrated piece of the robot including the power source, power electronics, and actuators that should be optimized as a whole rather than

separately. The performance metric for the power plant should be power or energy density of the integrated system, and should be chosen on a case by case basis based on such design criteria as the frequency of operation, size scale, and operation duration.

2.1 Power/Energy Density as a Mobile Millirobot Performance Metric

A good mobility metric for the locomotion ability of a millirobot is power density of the entire robot (or of its power plant). Considering different locomotion schemes (such as running, flying, or swimming), the general metric of a robot's power density allows comparison of behavior and costs among different locomotion schemes. Power density information is also available from nature from metabolic studies of locomotion. These values can be used as a known target point for any potential millirobot.

2.1.1 Muscle Power Density Values

To determine reasonable power density values to compare a robot's power plant power density, power density of muscle in animals and insects was examined. Accurately determining animal muscle power density is difficult due to many factors such as temperature dependence or peak vs. sustained output values. However, some values can be presented as representative for different locomotion methods.

It is widely known that not all locomotion methods have the same energetic cost; the most extreme demands are for hovering animals, especially hummingbirds [65]. One gram crawling or running animals in fact have aerobic capacities that are 28 times lower than those of 1 gram fliers [22]. Therefore, power density of muscles in flying animals (especially hovering animals) is expected to be the highest.

Shown in Table 2.1 are muscle output power densities for several representative animals.

Power density values were extracted both from work loops (in the case of the cockroach and fish) or from estimated output power from kinematics and an aerodynamic model (for the hummingbird and hawkmoth). Power densities are for muscles operating at or near 25^oC except for the fish operating at 10^oC. It is important to note that these power densities are for muscle power output, not for measured power input from oxygen consumption. Also, these values contain information about muscle efficiency since this is power outputted by the muscles, not the input power from the animal's power source. Muscle efficiency measurements vary significantly but for instance in insects range from roughly 2-34% [14] depending on the percent of energy recovery in the mechanical system. Considering that a loss in efficiency must correspond to an increase in power going into the muscle, efficiency is as important as muscle power density.

Animal	Type	Locomotion Conditions	Normal Muscle Power Density	Maximal Muscle Power Density
Lampornis clemenciae	hummingbird	Hovering	75W/kg[9]	309W/kg[9]
Manduca sexta	moth	Hovering	35W/kg[58]	90W/kg[58]
Blaberus discoidalis	cockroach	Running	6.5W/kg[23][1]	19-25W/kg[22][3]
Stenotomus chrysops	fish	Swimming	6W/kg[50][2]	28W/kg[50][3]

Table 2.1: Animal/insect muscle power densities for different locomotion techniques.
[1]Extrapolated for 13Hz running at 0.5m/s
[2]Extrapolated from muscle work loop data for 7.5Hz muscle contraction frequency in 10^oC water
[3]From work loop experiments

It is not difficult to argue that these animals are indeed dynamic rather than static locomoters; for instance, the cockroach *Blaberus discoidalis* can run up to 0.66m/s. Therefore, the power density numbers for the power plant (muscle) of these animals can be good design targets for the power plant (battery+electronics+actuator) for a dynamic millirobot. Obviously, the kinematics and dynamics of the motion are likewise important; more power does not mean better locomotion behavior if the robot's kinematics are grossly incorrect. Kinematics for any given locomotion technique will not be discussed here; since many millirobots suffer from low power density resulting in poor locomotion regardless of their locomotion efficiency, the focus is on new power density design goals for millirobots to solve this problem.

2.2 Components of a Mobile Millirobot

A mobile millirobot (or actually any robot in general) can be broken down into several key components. These are shown in Fig. 2.1; they are the power source (often a battery in millirobots), power electronics (power conditioning for the actuator that is chosen), the actuator(s) and finally the mechanical transmission, which includes linkages and frame elements.

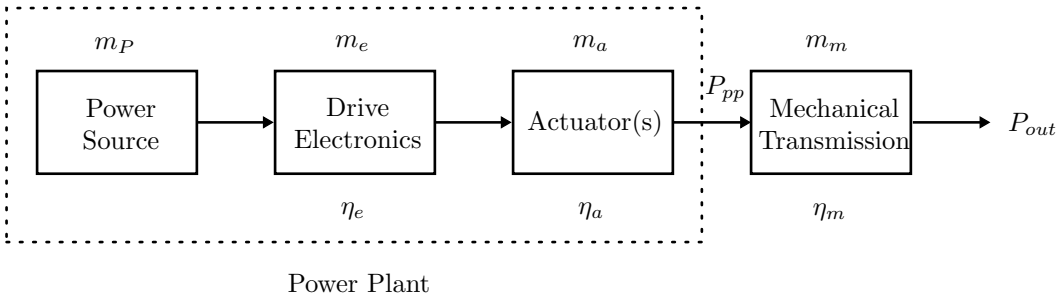

Figure 2.1: Power block diagram of a mobile robot.

The power density of the power plant of the robot diagrammed in Fig. 2.1 is given by

$$\gamma_{pp} = \frac{P_{pp}}{m_b + m_e + m_a} \tag{2.1}$$

Again, the mechanical transmission is not addressed here. With P_{out} being the power introduced to the environment by the robot and

$$P_{out} = \eta_m P_{pp} \tag{2.2}$$

where P_{pp} is the power output of the power plant of the robot (dashed box in 2.1), with sufficiently low η_m the robot would not perform dynamically. However, the focus here is on optimizing the power density of the power plant, leaving the locomotion scheme and kinematics to the designer and the specific utility of the robot.

2.2.1 Power Source

Power sources that have been used to drive untethered millirobots include solar cells [26], batteries (many robots), and combustion of chemical fuels (a MEMS Wankel engine in [19] and a gas turbine in [18]). Among these, the combustion engine solutions have the most promise because the energy density of octane fuel is approximately 35 times higher than a lithium battery. However, both the MIT MEMS turbine and the MEMS Wankel engine are still active research projects and have not yet been experimentally verified. Solar cells have been used as power sources for millirobots such as in [26]; however, solar cells need to have large surface areas for significant power production and are thus generally very large and heavy compared with equal power capacity lithium batteries (the solar cells in [26] have a peak power density of 43W/kg). For its high energy density, ease of integration, and the fact that it is mature technology, the only power source considered here is a lithium polymer battery.

Lithium Polymer Battery Energy Density

Energy densities for several miniature lithium polymer batteries (Full River brand) are shown in Fig. 2.2. Energy density clearly drops as the battery weight drops due to a larger percentage of the battery weight needed for packaging; around 170 Wh/kg is the asymptotic value for energy density for large batteries though it varies by brand and use.

Maximum discharge rate for lithium ion batteries is also important and is dependent on the internal resistance of the battery and its heat dissipation abilities. A plot of power density for the miniature batteries shown in Fig. 2.2 for various discharge rates is shown in Fig. 2.3. One can see that many of the batteries have a maximum discharge rate of 10C, which limits their peak power density. At 5C, the batteries last 12 minutes; at 20C, they last 3min. These energy and power density characteristics must be considered in designing a high power density power plant for a millirobot.

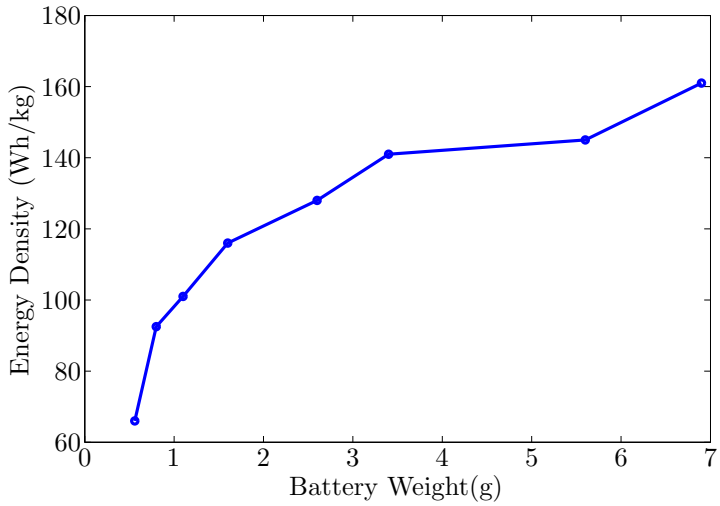

Figure 2.2: Energy density for several miniature lithium polymer batteries available from [31]

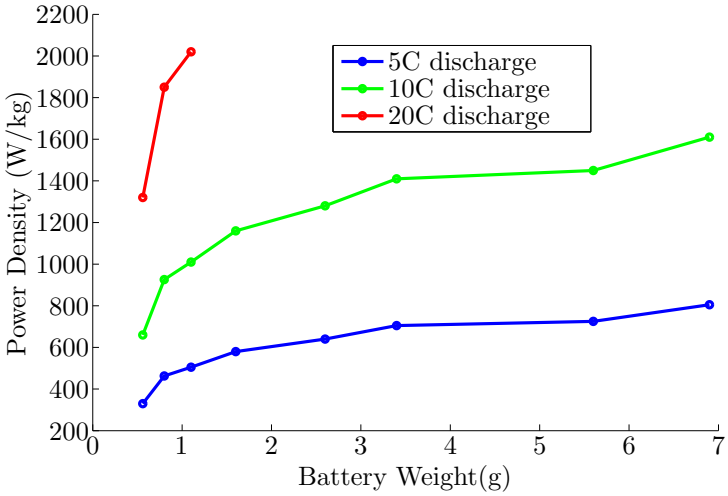

Figure 2.3: Power density for several miniature lithium polymer batteries available from [31]. The power outputs are theoretical assuming a nominal output voltage of 3.7V for all discharge rates.

2.2.2 Actuation

Actuation will be addressed next since drive electronics are determined by the actuator chosen. There have been many actuation technologies used for millirobots and microrobots, including shape memory alloy, piezoelectric elements, DC brushed and brushless motors, MEMS capacitive actuators, and EAPs (electroactive polymers) which include but are not limited to dielectric elas-

tomer (DE) and IPMC (ionic polymer metal composite) actuators. If maximizing the power density of the power plant of a robot is the goal, the mass, power density, and efficiency of the actuator all are critical design criteria. The frequency dependent operation of the actuator is also of critical importance; for many actuators the energy density cannot be simply multiplied by the frequency to find power density due to losses in power output even below the bandwidth of the actuator.

Shape Memory Alloy

The most common type of shape memory alloy is nickel titanium wire, though many other alloys exist. Heating a shape memory alloy wire causes a phase transformation of the metal, from an initial martensite phase to an austenite phase. This causes a contraction in the wire (typically 3-5% but even up to 8% [35]). As it cools down, the wire relaxes to its initial length. The phase transformation also causes other material changes such as a significant change in Young's modulus (from around 28-40GPa in the cool phase to 83GPa in the high temperature phase) that makes the SMA difficult to control. Therefore, SMA actuators are usually used in a binary off/on mode.

Nickel titanium shape memory alloy wire is commercially available from Dynalloy, Inc under the brand name Flexinol [35]. Flexinol is claimed to have 8.5% recoverable strain and operates at 5% efficiency [35]. Wire diameters are available from 1 mil (25μm) to 20 mil (500μm); due to the small diameter of the wire, compared with other actuation technology SMA is exceptionally light. However, the power density of shape memory alloy is not easily found in the literature. Power density testing of Flexinol wire has been done by Aaron Hoover (currently unpublished) at UC Berkeley; results for preliminary runs are shown in Table 2.2. Since SMA is a thermal actuator, waiting for it to cool down to return to its martensite state is a slow process (although this occurs faster as wire diameter decreases). In this testing, the smallest wire diameter of 25μm has a bandwidth of 6Hz.

Wire Diameter	Max Power Drive Frequency	Power Density
1.0 mil	6Hz	7491W/kg
1.5 mil	3.5Hz	2487W/kg

Table 2.2: Power output data for Flexinol SMA wires (unpublished data from Aaron Hoover, 2008)

Shape memory alloy wire can also be made into springs to achieve more actuator stroke at the cost of force [64]; however this does not change the power density of the material.

Miniature DC Motors

Miniature DC motors exist for various control and power applications such as miniature control servos or for the vibrate function on current cellular phones. Several of these motors are sold by Didel [34] for hobbyists, usually for miniature RC aircraft. Power output data and power density numbers for several representative motors appear in Table 2.3.

Motor	Weight	Max Power Output	RPM@Max Power	Power Density	Efficiency
MK04-24	0.7g	64mW	24720	91W/kg	27%
MK06-10	1.4g	118mW	14340	84W/kg	43%
MK06L-09	2.1g	330mW	17400	157W/kg	37%
MK07-08	3.1g	450mW	24000	145W/kg	40%
MS08-12	4.5g	445mW	8460	99W/kg	49%
MK10-10	4.8g	323mW	14580	67W/kg	45%

Table 2.3: Power output data for various miniature DC motors from [34]

However, the motor alone is difficult to integrate into a robot because of the high RPM required to achieve maximum output power. A gearbox is necessary for these motors; Didel sells several different gearboxes for these motors, from 1:4 to 1:26.6 gear ratios. Weights for these complete gearbox sets range from 0.5g to 0.75g. When the gearbox is included in power density calculation as is necessary, one achieves the characteristics in Table 2.4 (assuming a 90% efficient gearbox weighing 0.6g as is claimed by Didel, but 50% may be more realistic).

Motor	Motor+Gearbox Weight	Total Power Density	Efficiency
MK04-24	1.3g	49W/kg	24%
MK06-10	2.0g	59W/kg	39%
MK06L-09	2.7g	122W/kg	33%
MK07-08	3.7g	122W/kg	36%
MS08-12	5.1g	87W/kg	44%
MK10-10	5.4g	60W/kg	41%

Table 2.4: Power output data for various miniature DC motors with gearboxes attached [34]

There are many other existing small DC motors; some are outer rotation motors which may

in fact not need a gearbox or could use a lighter, more efficient gearbox with low step down ratio. One such motor is the Mighty Midget Nano which weighs 1.5g [36]; however, no power output or efficiency data is currently available for that motor, though data for heavier outer rotation motors from the same manufacturer is available in [29].

Piezoelectric Actuators

Piezoelectric actuators utilize materials that distort when an electric field is applied (the inverse piezoelectric effect). Piezoelectric materials are most often ceramics whose structure has no center of symmetry. Their displacement is due to separation between positive and negative charge sites in the crystal material leading to a net polarization [62]. Piezoelectric actuators are classified generally into two classes: stack actuators and bending actuators. The challenge in using piezoelectric actuators is their low stroke; approximately 0.1% strain in the d_{31} mode and 0.3% strain in the d_{33} mode. Stack actuators utilize the crystal's d_{33} mode for actuation; bending actuators usually utilize the smaller d_{31} mode along with a mechanical amplifier (bending) to produce larger displacement. More about piezoelectric actuator geometry can be found in Chapter 4.

Literature quantifying power output for piezoelectric actuators is not common. Often, piezoelectric materials are used as sensors (such as in sonar) and not as actuators. For those applications using piezoelectric materials as an actuation source, often power output is not analyzed or power output is extrapolated from DC measurements. Piezoelectric bending actuators were chosen as the actuation source for the Micromechanical Flying Insect project at UC Berkeley [69] because of their high bandwidth and light weight. These actuators were specially optimized using composite materials and novel geometries [73]. However, until the work contained here, only DC extrapolations of power output of these actuators were available and are contained in Table 2.5.

Mass	Length	Displacement	Blocked Force	Energy Density
11.75mg	10mm	520μm	123mN	2.73J/kg

Table 2.5: Optimized piezoelectric bending actuator performance predicted in [73]

DC extrapolations of energy density are most likely overestimates of piezoelectric power output due to hysteresis, internal damping, and many other effects (further discussed in Chapter 3). The first AC measurements of the power output of these actuators is presented in this work in Chapter 3. The prediction here from DC measurements would be a power density of 819W/kg for the actuator operating at 300Hz (piezoelectric power densities are best at high drive frequencies).

Electroactive Polymers (EAPs)

Electroactive polymers are materials that displace or change size when subject to electric stimulation, sometimes even producing over 100% strain. Many of their characteristics make them the closest engineering solution to natural muscle. EAPs can be generally classified into two classes [4]:

- **Electronic EAPs:** These EAPs produce large strain when subject to an electrostatic field. Unfortunately, due to thickness of the material and fields required, these actuator often require several kV of potential to actuate. The most common type of electronic EAPs are dielectric elastomer (DE) actuators.

- **Ionic Electroactive Polymers:** These EAPs (the most common of which is IPMC or ionic polymer metal composites) also respond to an electric field, but the fields are much lower and the displacement is activated by the movement of ions and hence a change in pH. In fact voltage levels around 2V can be used to drive an IPMC actuator. Due to their need for mobile ions, IPMCs are commonly used in a liquid (e.g. water) environment.

These are not the only types of EAPs. Several others include ferroelectric polymers, electrostrictive graft elastomers, electrostrictive paper, electroviscoelastic elastomers, etc, but dielectric elastomers and IPMCs are the most common EAPs in use. A good review of current EAP technology including all the types listed here can be found in [4].

EAPs are most often compared to muscle because 1) they are polymer actuators and 2) they have low elastic stiffness (unlike piezoelectric materials which are usually stiff ceramics). Like other actuator technologies, very few researchers have explored the power output and power density of the materials, but some efficiency and power output values are available for DE and IPMC actuators.

Meijer and Full [42] did work loop tests on several dielectric elastomer EAPs and extracted peak power output of the materials. Their results are summarized in Table 2.6.

EAP	Frequency at Max Power (Hz)	Max Power Density
VHB 4910 Acrylic	4	35.28 W/kg
CF19-2186 silicone	10	20.37 W/kg
P(VDF-TrFE) unstretched	2	0.51W/kg

Table 2.6: Three dielectric elastomer EAP power output results from [42].

Maximum efficiency for dielectric elastomer EAPs has been reported in [47] as 18%, but this is not the operation point at which maximum power is produced by the actuator. In fact, the actuator efficiency is as low as 1% at the maximum power output point. The best reported efficiency of IPMC actuators is 3% in [53]. IPMC actuators also have very slow response (on the order of fractions of a second [5]).

Summary

The actuators described in this section vary widely in performance and specialization. Some are high speed, low stroke actuators (piezoelectrics) while others are very high stroke and low speed (EAPs). The power density of shape memory alloy actuators make them initially very attractive; however, these actuators are quite slow, inefficient, and have only 5% strain. DC motors have good power density, speed, and efficiency, but if actuators much less than 1g are necessary they are not an available technology. Piezoelectrics, EAPs, and SMAs on the other hand scale very well for very lightweight applications. Piezoelectrics are stated here to have high power density, but this assumes they are being driven at high frequency (>100Hz). These behaviors have been summarized qualitatively in Table 2.7. It can easily be seen here that there is no dominant actuation technology

at the milli-scale as gasoline engines and electric motors are dominant at larger scales; choosing an actuator technology for each application is required.

Actuator	Stroke Length	Bandwidth	Efficiency	Power Density
piezoelectric stack	★	★★★★★	★★	★★★★
piezoelectric bender	★★	★★★★★	★★	★★★★
EAP - IPMC	★★★	★	★	★
EAP - DE	★★★★	★	★★	★★
DC motor (brushed)	★★★★	★★★	★★★	★★★
SMA (Flexinol)	★★	★	★	★★★★★

Table 2.7: Qualitative summary for millirobot actuator technologies.

2.2.3 Drive Electronics

Drive electronics as diagrammed in Fig. 2.1 are determined by the actuator chosen. Some actuators lend themselves to very minimal drive electronics (IPMC, SMA, and DC motors) while some require high voltages (piezoelectric stack and benders) or even very high voltages (dielectric elastomer EAP). Although a very aggressive power electronics design such as an ASIC has not been attempted for very small millirobots (besides for the solar cells in [26]), some attempts have been made for shape memory alloy, dc motors, and piezoelectric actuators. At Berkeley, both a lightweight piezoelectric power supply and a shape memory alloy power supply have been constructed for use on various millirobots [56][27].

Drive Electronics for Piezoelectric Actuators

For piezoelectric actuators, field levels of 2V/μm are often necessary; for a thin piezoelectric ceramic thickness of 125μm, this requires 250V potential. A DC to DC converter is necessary for boosting from the nominal battery voltage of 3.7V. A lightweight boost converter combined with a charge pump circuit was created for the piezoelectric bending actuators in [72] and is the lightest weight known piezoelectric power supply. This completed circuit weighs only 300mg and can output a maximum of 6.5mW (the board was customized for driving 2 very small piezoelectric benders). It operates at a peak electric efficiency of 62%. The power supply circuit is discussed in more detail in

Appendix B. Although an ASIC could provide a lighter and perhaps more efficient power supply, this PC board solution is currently the state of the art in lightweight piezoelectric supplies.

Drive Electronics for SMA

Shape memory alloy actuators can be actuated by passing current through them, heating the wire thereby initiating the phase transformation. The smallest 1 mil (25μm) diameter Flexinol wire has a resistance of 18 Ω/cm. The largest diameters have much lower resistances, (0.06 Ω/cm for 500 μm wire). For small diameters, nominal battery voltages (3.7V) are not high enough to produce high enough currents to quickly initiate the phase transformation. Therefore, a DC to DC converter must be used to drive them, adding weight and power loss to the system.

A lightweight boost converter to drive 1 mil shape memory alloy was constructed for actuating a 2.4g crawling robot [27]. More details including the specific design of the converter can be found in Appendix B. The boost converter along with its PC board and drive transistors weighs 340mg and can produce a maximum output power of 1.5W, operating at peak power at 83% efficiency. Again, it is possible to make a lighter, more efficient converter than this, but to the author's knowledge this converter is the lightest available to drive high resistance (170 Ω) shape memory alloy actuators.

Drive Electronics for EAPs

IPMC actuators are actuated by applying nominal voltages to the actuators while they are in the presence of a mobile ionic fluid. The drive voltage can be as low as 2V as in [39], lending themselves to be driven directly from battery voltages thus making IPMC actuators the easiest to electrically drive.

Dielectric elastomer EAPs, on the other hand, require very high drive fields and voltages, typically 150 V/μm or >1kV for common thicknesses [54]. Even though they require very low currents, using a lightweight DC to DC converter to generate over 1kV from nominal battery voltages

is difficult and most likely cannot be done efficiently for 1g or under. To the author's knowledge the only untethered dielectric elastomer robot is the large hexapod in [16].

Drive Electronics for DC Motors

Brushless DC motors, depending on the winding resistance, can usually be driven directly from the battery without a DC to DC converter. Although a speed controller is needed for most applications, a lightweight speed controller could most likely be built at a weight of 200mg for most applications; a brushless DC motor controller would most likely be around this weight also (the Micro Invent MBC3BL Controller from Bob Selman Designs is 220mg [31]).

2.2.4 Mechanical Transmission

As has already been briefly discussed, the mechanical transmission plays a critical role in the efficiency of transferring energy to the environment, particularly if it incorporates any energy saving mechanisms or runs at resonance. Choosing correct locomotion kinematics is not addressed here. However, it is important to address the transmission technology being using which is the SCM process utilizing composites and polymer flexures. Losses in the SCM process (besides stiffness and inertia losses which are not an issue at resonance) primarily come from damping in the polymer flexure joints. Through vacuum and air testing, the efficiency of a fourbar linkage made with SCM has been estimated in [56] at 90%. Compared with actuator and power electronics efficiencies, the transmission losses internal to the structure are therefore not an issue. The efficiency of a walking gait or flapping trajectory would also be a much larger source of loss.

2.3 Example Power Density Design for a Millirobot

Given the power density and efficiency values in the preceding sections, an example power density robot design is presented here. The design is for a <3cm crawling robot that has been

fabricated and published in [27]; presented here is the actuator selection process done before the robot was designed and manufactured.

The robot was made with the standard SCM process utilizing composites as stiff links and flexures as approximations of pin joints as described in [70]. For a 3cm size, the robot frame, mechanical transmission, and legs can be made with approximately 400mg of material. This is known from the experience of past designs.

The main choice in the power density context is the power plant of the robot, which includes the power source (lithium polymer battery), power electronics, and actuator. The target leg frequency is set at a reasonable 10Hz, and the target run time is 10min (meaning the battery is discharged at 6C). Table 2.8 is a best case performance comparison of the various actuators discussed here if they were to be used as the power plant to drive the robot for exactly 10 min.

Actuator	Power Density	Efficiency	Mass	Power Electronics Mass	Battery Mass
Dielectric Elastomer	20W/kg	18%	2.0g	1.5g	0.7g
SMA	3430W/kg	5%	6.5mg	0.32g	0.7g
DC Motor	49W/kg	24%	1.3g	0.2g	0.7g
Piezoelectric - Bending	27W/kg	10%[56]	1g	0.8g	0.7g

Table 2.8: Crawling robot actuator characteristics for power density design (assuming a 0.7g battery for all designs).

The data in Table 2.8 makes several simplifying assumptions. First, in order to run at 10Hz, the dielectric elastomer actuator chosen was a silicone actuator with power density of only 20W/kg (not the maximum of 35W/kg for an acrylic DE because this DE only operates at 4Hz for maximal power output). An estimation for the power electronics mass of 1.5g was made for the high voltage drive of the DE, operating at an assumed 50% efficiency.

For the shape memory alloy actuator, 1mil diameter wire was used with the power supply already built and discussed earlier. The SMA power density of 7491W/kg in Table 2.2 was reduced to 3430W/kg for the power density of the material at 10Hz (past its 3dB bandwidth). For the DC motor, the 0.7g MK04-24 from Didel was used with a 0.6g gearbox that is 50% efficient (considering the rather large stepdown ratio needed to run at 10Hz). And finally, the piezoelectric bending

actuator power density was scaled to 10Hz operating frequency and the power electronics scaled up to 0.8g for the large capacitive load of a 1g piezoelectric bending actuator. The piezoelectric step up power supply was still assumed to run at 63% efficiency with no charge recovery. Again, the power density value here is most likely an overestimate because it has been estimated from DC extrapolations of the piezoelectric actuator's behavior. IPMC actuators were not considered both because they are too slow and because the robot is operating in air, even though some attempts have been made to construct IPMC gel actuators incorporating the ionic fluid in an air-tight case with the actuator [21]. It can also be noted that some of these actuators lend themselves to be split into several separate actuation sources (like DE, Piezoelectrics, and SMA) where the DC motor is very heavy and only one can be incorporated.

With these assumptions, the power output and the power density of each power plant considered is shown in Table 2.9.

Actuator	Power Plant Output Power	Power Plant Power Density
Dielectric Elastomer	40mW	9.5W/kg
SMA	18mW	17.6W/kg
DC Motor	60mW	27W/kg
Piezoelectric - Bending	28mW	11W/kg

Table 2.9: Crawling robot power output and power density values for the design experiment.

Alternatively, one can consider a constant power density for the robot with different actuation schemes and compare the lifetime of the robot. If the power plant alone has a required power density of 9.5W/kg, the run time before the battery is depleted for the different design is shown in Table 2.10. If the robots are identical kinematically, the lifetime is also proportional to the total travel distance.

Actuator	Battery Lifetime @ 9.5W/kg
Dielectric Elastomer	10min
SMA	18min 30 sec
DC Motor	28min 25sec
Piezoelectric - Bending	11min 34sec

Table 2.10: Crawling robot design lifetime at a given power plant power density.

As one can see, the DC motor achieves the highest power plant power density, followed by shape memory alloy, piezoelectric bending actuators, and finally the dielectric elastomer. This example shows that all power densities, speeds, and efficiencies must be considered. It is difficult to predict the best actuator for a design by looking at only the power density, efficiency, or weight of each actuator alone.

Although the DC motor solution provides the most power to the system, the small crawling robot was designed and constructed first with shape memory alloy actuators. Since it is more difficult to incorporate a rotary actuator into SCM technology, the kinematics of motion were first verified in [27] with a working robot using SMA. Several design changes were made during construction for various reasons, such as using 1.5mil rather than 1.0 mil SMA and reducing the operating frequency to 3Hz. The overall untethered autonomous robot weighs 2.4g (including a 400mg control and processing board not included in the analysis here). The final power plant power density is ultimately limited by the length of SMA that can be fit into the current kinematic design of the robot, which is approximately 160mm of SMA wire (weighing 1.14mg). At 3Hz operation, a power density of 1.14W/kg is predicted for the overall robot and 2.74W/kg for the power plant alone. The battery lifetime is predicted to be over 11 minutes. Experimentally, the robot walks at 3 Hz for 9 min, 40 seconds. The power density of the robot is low and can be addressed by adding more SMA wire into the design (which is difficult kinematically) or switching to a DC motor driven design (which is currently underway).

Chapter 3

Verification of Piezoelectric Actuator Power Output

Piezoelectric bending actuators have been utilized for many years as the main actuation mechanism for the MFI. They have also been used by other researchers to actuate control surfaces for indoor slow fliers [71], and even as motors for legged microrobots [51],[24]. However, in dynamic robots where piezoelectric actuators are the main source of actuation such as in the MFI, the power output of these actuators was previously unknown. Using oversized piezoelectric bending actuators, sufficient lift forces have been generated by the MFI platform on a test bench setup [55]. However, when the actuators are scaled down to the true 10mg MFI size, flapping amplitude and rotational control are significantly reduced and high lift forces cannot be produced. This result casts doubt on the true power output of the miniature bimorph actuators, and before proceeding with further design improvements it is necessary to validate the power output capabilities of these actuators. For reference, estimates for hovering power for a 100mg MFI are approximately 5mW per wing [74], which is a minimum of 2.5mW per actuator for the current two actuator per wing MFI design.

Several researchers have addressed issues regarding power output and power density for

piezoelectric actuators. In the field of piezoelectric transformers, efficiency limitations are discussed in [20]. Pomirleanu [48] has reported power outputs for piezoelectric stack actuators, but only for quasi static conditions (which from experience is likely an overestimate). Near [43] has extrapolated constituent equations to predict power output for popular bimorph and other piezoelectric actuators (such as RAINBOW). In [73], energy densities for the 10mm, 10mg MFI bimorph actuators are predicted from DC measurements.

However, extrapolation techniques in all of these previous works are suspect. It is widely known that the properties of piezoelectric actuators (such as d_{31} and the Young's modulus) can change drastically when the actuators are subject to high fields or high displacements [60] [63]. In addition, extrapolating behaviors as simple as maximum strain in the piezoceramic (such as the large strain values found in [46]) is invalid since these values are for only internally induced strain; external mechanical strain can make the piezoceramic fail prematurely, especially when it is simultaneously stressed via an electric field. The effect of nonlinearities such as creep, hysteresis, saturation, etc. can also reduce power output of piezoelectric actuators, but to the author's knowledge this has not been quantified at sufficient field (only up to 0.1V/μm in [63]).

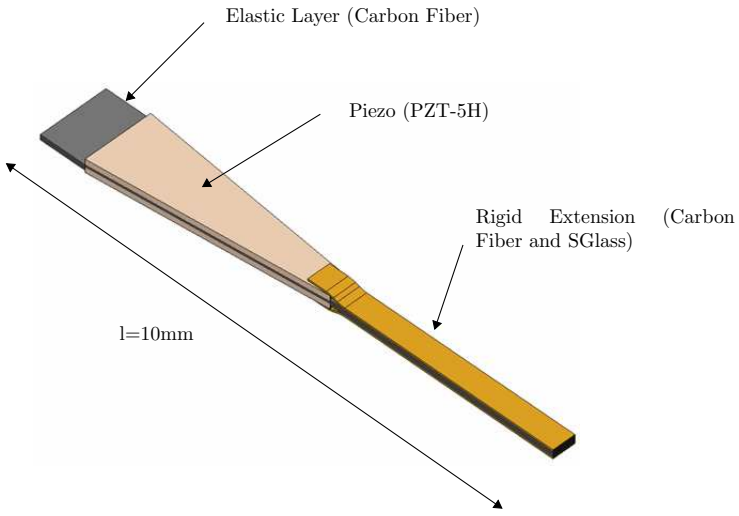

Figure 3.1: 10mg piezoelectric bending actuator.

This chapter focuses on measuring the power output of 10mm piezoelectric bending actu-

ators, specifically those reported in [73] optimized for the MFI. The actuators weigh approximately 10mg and are composed of PZT-5H actuation layers (from Piezo Systems, Inc) with a carbon fiber elastic layer and glass fiber/carbon fiber extension as shown in Fig. 3.1 (further details on the materials can be found in [73]). In order to measure the power output and delivered power density for these actuators, a tunable dynamometer was designed to actively measure force and displacement of an actuator and therefore compute power output. The dynamometer contains another actuator that can actively simulate various loads (varying stiffness, mass, and damping). The goal was to run the device under test (DUT actuator) at frequencies up to 100Hz and explore the actuator's behavior as frequency, displacement, and voltage drive level were varied. Even though only one specific size of actuator is tested, the goal is to be able to draw conclusions about piezoelectric materials such as PZT-5H in general as a possible actuation method for millirobots.

3.1 Dynamometer Design

To control the applied force on the DUT running up to 100Hz, another (larger) actuator (denoted the Driver actuator) is needed with a bandwidth above the desired operating frequency. In order for a piezoelectric actuator to run in a reasonably efficient way, it must be used as if it was driving a load at resonance [56]. In order to do so, the Driver actuator in the dynamometer must simulate various stiffnesses and masses for resonance, in addition to acting as a desired damping value. This allows the choice of both the resonant frequency and oscillation amplitude of the actuator under test.

A Driver actuator (another, larger piezoelectric bimorph) is attached to the DUT via a lightweight spring with a known spring constant. Custom optical position sensors accurate to about 1 μm are used to monitor the position of both actuators [57]. The setup appears in Fig. 3.2. It is important to note that the spring is not the load that the DUT sees; it merely functions as a force sensor.

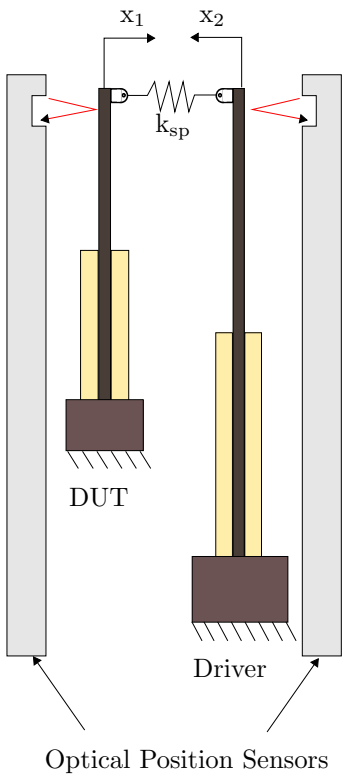

Figure 3.2: Schematic of proposed dynamometer.

3.1.1 Dynamic Model of Piezoelectric Bending Actuator

A piezoelectric bending actuator was modeled as a force source (representing the piezoelectric plate) in parallel with a spring (representing the elastic layer) [68]. At high frequencies, piezoelectric damping losses (coming from a variety of sources such as the matrix in the composite layers, hysteresis, and other piezoelectric nonlinearities) and mass of the actuator are included. In this case, the mass term is an equivalent mass derived from the distributed mass of the actuator.

This simple second order model is far from an exact model for the actuator in that it does not contain any direct expressions for creep, hysteresis or saturation. However, if the model is fit to the experimental frequency response of an actuator (with appropriate stiffness, mass, and damping via least squares in Table 3.1), Fig. 3.4 shows that the second order model is a fair approximation of the bending actuator when it is driven unloaded at low fields. The resonant peak

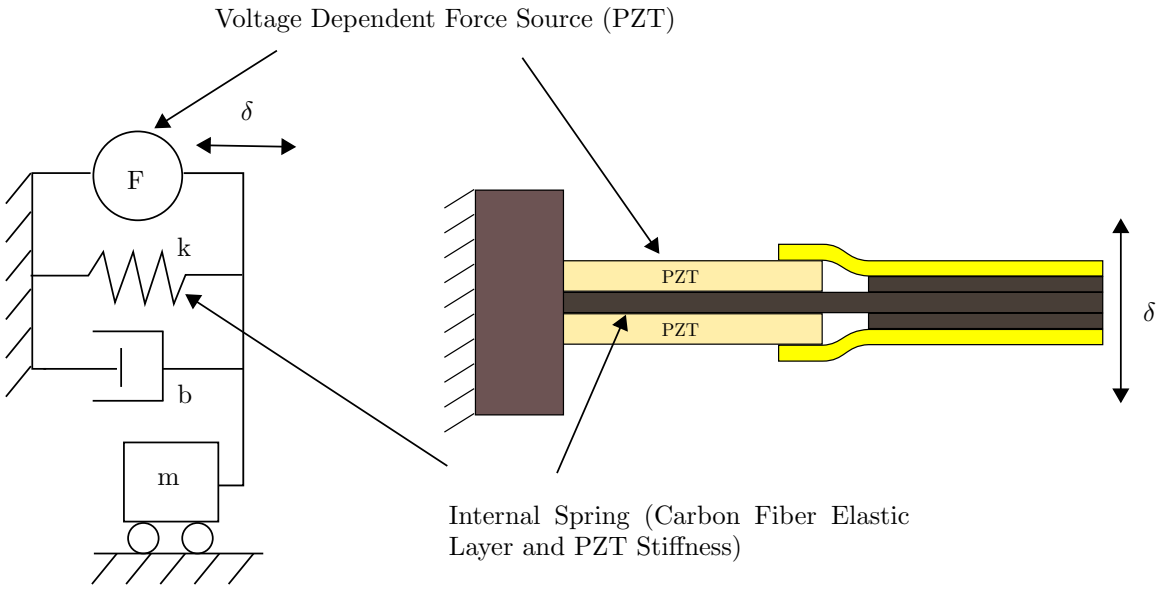

Figure 3.3: Second order model of a cantilever bending actuator.

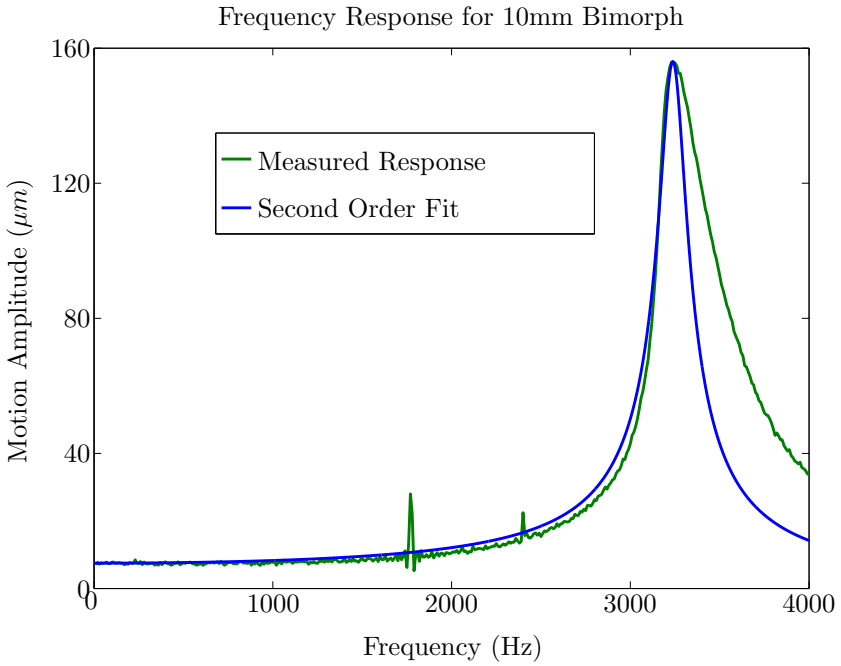

Figure 3.4: Frequency response (magnitude Bode plot) for 10mm bimorph (10V amplitude drive or 0.08V/μm).

Table 3.1: Second order best fit model parameters.

Parameter	Fit Value
k	$250N/m$
b	$5.9 * 10^{-4}Ns/m$
m	$6.0 * 10^{-7}kg$

of the actuator is significantly wider than the model's and slightly asymmetric; this can be explained by both softening in the actuator at high displacements, which the model does not account for, and nonlinear (frequency dependent) internal damping in the material. Up to the resonant peak, however, a second order model is sufficient to properly predict the frequency response of the actuator.

3.1.2 Dynamic Model of Entire Dynamometer

Using the simple model for a single piezoelectric bending actuator in Fig. 3.3 and applying it to the proposed dynamometer in Fig. 3.2 results in the complete model in Fig. 3.5. Here the mass and damping in the connecting spring (functioning as a force sensor) are included for completeness.

The work output of the DUT in the setup of Fig. 3.5 can be expressed as

$$W = \int_{x_0}^{x_f} F_{DUT} dx_1 \tag{3.1}$$

where F is the force output of the DUT. For periodic inputs (such as for a wing drive for the MFI), this can be expressed in terms of velocity and time as

$$W = \int_{t_0}^{t_f} F_{DUT} v_1 dt \tag{3.2}$$

where W is energy output per oscillation cycle. Representing the actuator positions x_1 and x_2 as the sum of their sinusoidal harmonics yields

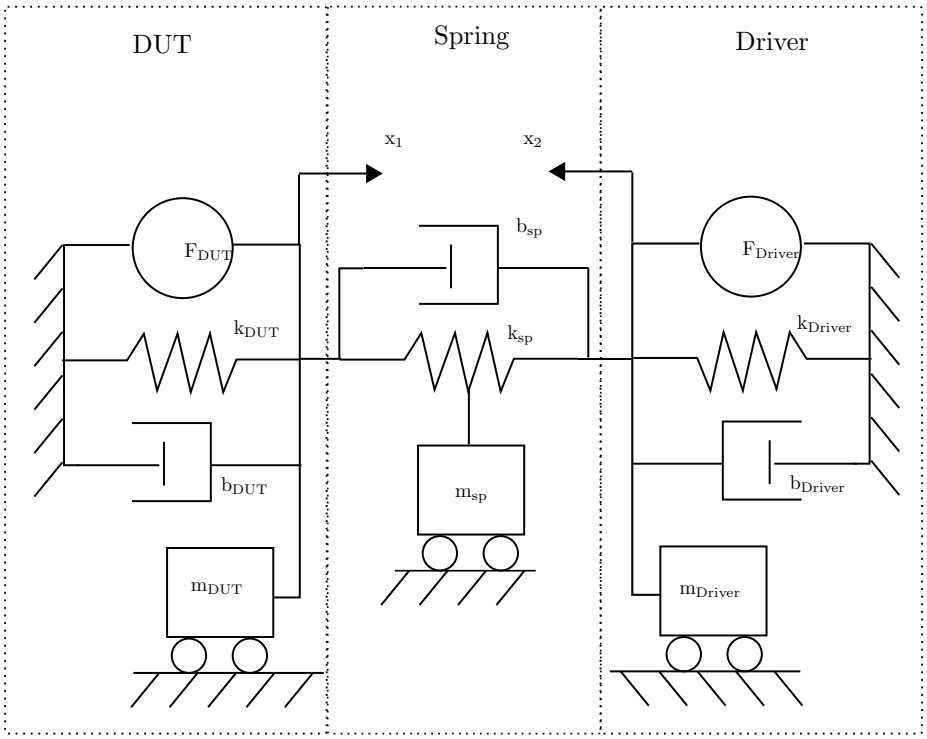

Figure 3.5: Block diagram of dynamometer.

$$x_1 = \sum_{n=1}^{\infty} A_n \sin(n\omega_o t + \phi_n) \tag{3.3}$$

$$x_2 = \sum_{n=1}^{\infty} B_n \sin(n\omega_o t + \psi_n) \tag{3.4}$$

$$v_1 = \dot{x_1} = \sum_{n=1}^{\infty} A_n n\omega_o \cos(n\omega_o t + \phi_n) \tag{3.5}$$

where ω_o is the fundamental drive frequency. The force output of the DUT can be expressed, in general, as

$$F = k_{sp}(x_1 + x_2) + b_{sp}(\dot{x_1} + \dot{x_2}) + m_{sp}(\ddot{x_1} + \ddot{x_2}) \tag{3.6}$$

Before deriving expressions for the work output of the DUT in terms of the variables defined

here, it is useful to look at a few simple examples that relate to the problem at hand. Shown in Fig. 3.6(a) is a simple example of a force source displacing a grounded spring. If the force source is driven sinusoidally, the position x_1 can be expressed as

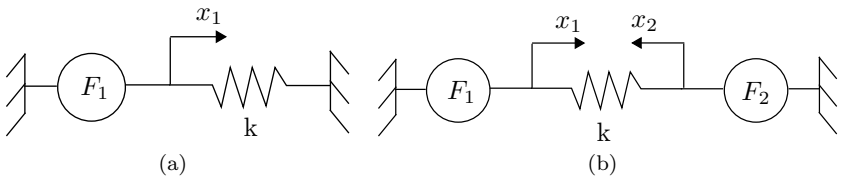

Figure 3.6: Work done by a force source on a spring examples

$$x_1 = A\sin(\omega t) \tag{3.7}$$

The work done per cycle by the force source on the spring is then given by

$$W = \int_0^T Fv dt = \int_0^T kx\dot{x}dt = A^2 k\omega \int_0^T \sin(\omega t)\cos(\omega t)dt = 0 \tag{3.8}$$

which is an obvious result considering that the initial and final position of the system are identical. An important difference can be seen in Fig. 3.6(b) where the spring is no longer grounded. If the two positions x_1 and x_2 are prescribed as sinusoidal but with different phases, or

$$x_1 = A\sin(\omega t + \phi_1) \tag{3.9}$$

$$x_2 = B\sin(\omega t + \phi_2) \tag{3.10}$$

the work per cycle of the entire system (the sum of the work per cycle of the two force sources) is again 0. However, the work done by just one of the force sources, say F_1, is not zero. The work per cycle of the source F_1 is given by

$$W = \int_0^T F_1 \dot{x_1} dt = \int_0^T k(x_1 + x_2)\dot{x_1} dt \tag{3.11}$$

$$= \int_0^T kA^2\omega \sin(\omega t + \phi_1)\cos(\omega t + \phi_1) + kAB\omega \sin(\omega t + \phi_2)\cos(\omega t + \phi_1) dt \tag{3.12}$$

$$= ABk\pi \sin(\phi_2 - \phi_1) \tag{3.13}$$

This result can be extended to the full dynamometer system shown in Fig. 3.5 with the expressions for x_1 and x_2 including higher harmonics in (3.5). The force source F_1 of 3.6(b) can be likened to the entire DUT side of the dynamometer separated with dashed lines in Fig. 3.5; the force source F_2 can be likened to the Driver side of the diagram. The connecting spring of the dynamometer is shown with mass and internal damping in addition to a linear spring for completeness.

The work done per cycle in harmonic n for the DUT is

$$W_n = W_{k,n} + W_{b,n} + W_{m,n} \tag{3.14}$$

where

$$W_{k,n} = A_n B_n \pi k_{sp} \sin(\phi_n - \psi_n) \tag{3.15}$$

$$W_{b,n} = A_n \pi n \omega_o b_{sp}(A_n + B_n \cos(\phi_n - \psi_n)) \tag{3.16}$$

$$W_{m,n} = A_n B_n \pi m_{sp} n^2 \omega_o^2 \sin(\phi_n - \psi_n) \tag{3.17}$$

$W_{k,n}$ is the energy per cycle provided by the DUT measured by the spring in harmonic n; $W_{b,n}$ and $W_{m,n}$ are additional energy that are dissipated by the damper and mass of the connecting spring in each harmonic n. Like the example with the ungrounded spring earlier, it is very important to note that $W_{k,n}$ is not zero because it is driven by another source (the Driver) rather than connected

to ground and only the work output of the DUT is included in the expression for $W_{k,n}$.

The total energy output per cycle of the main drive ω_o (W) and total power output P of the DUT can then be written as

$$W = \sum_{n=1}^{\infty} nW_n = \sum_{n=1}^{\infty} n(W_{k,n} + W_{b,n} + W_{m,n}) \tag{3.18}$$

$$P = \frac{W\omega_o}{2\pi} \tag{3.19}$$

The values of mass and damping in (3.16) and (3.17) are difficult to predict. If it is required that

$$k_{sp} >> \omega_o b_{sp}, \omega_o^2 m_{sp} \tag{3.20}$$

(where ω_o is the drive frequency) then $W_{b,n}$ and $W_{m,n}$ of 3.14 can be disregarded. Therefore, when constructing the force sensing spring, b_{sp} and m_{sp} must be small to run the system up to the goal of 100Hz. It is important to note that throughout this analysis and design, the Driver's damping, inertia, and spring properties did not enter in the energy delivery calculations. These parameters were very difficult to measure accurately.

3.2 Dynamometer Construction

The Driver actuator is constructed similarly to the DUT, except the size is scaled up. The connecting spring has several design requirements. Some were listed earlier in terms of its mass and damping and linearity. The spring also needs to connect to both actuators in such a way that their bending does not cause any type of binding in the system. In theory, this is simply achieved by putting pin joints at the attachment points of the two actuators (as is shown in Fig. 3.2), but in practice at this scale pin joints have hysteresis and friction and also weigh too much. Finally, the

spring needs to be removable from the DUT and Driver actuator so that the DUT can be repeatedly changed.

A model of the connecting spring is shown in Fig. 3.7; the actual constructed spring is shown in Fig. 3.8. The spring is made of carbon fiber bent around a mold during curing, then glued to two separate, smaller arcs cured in the same manner. The main span is the linear spring element; the two arcs at the end of the spring relieve the moment due to bending of the two actuators by employing Kevlar fiber, strung tightly between the arcs. The Kevlar fiber is very compliant to moments since it is made up of several threads that are wound together. Since the actuators are not perfectly parallel, the string also serves to allow small off-axis deflections. Stiff carbon fiber planks were glued permanently onto the Kevlar string to attach the planar ends of the actuators with a low melting point plastic, which serves as a removable mount through heating for different DUTs.

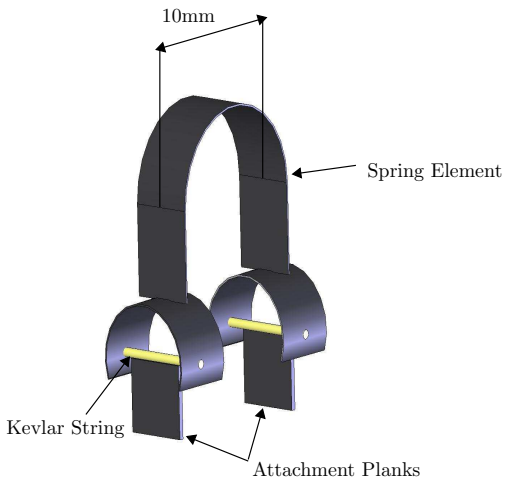

Figure 3.7: Schematic of custom dynamometer spring.

The entire dynamometer with both actuators, connecting spring, and position sensors is shown in Fig. 3.9. Both the Driver and DUT bimorph actuators were embedded at their base in fiber reinforced polyurethane for a solid ground. Horizontal and vertical micropositioning stages were employed to line up the spring prior to attachment. To calculate the spring constant of the connecting spring (which can vary slightly for different attachments), each DUT was actuated after

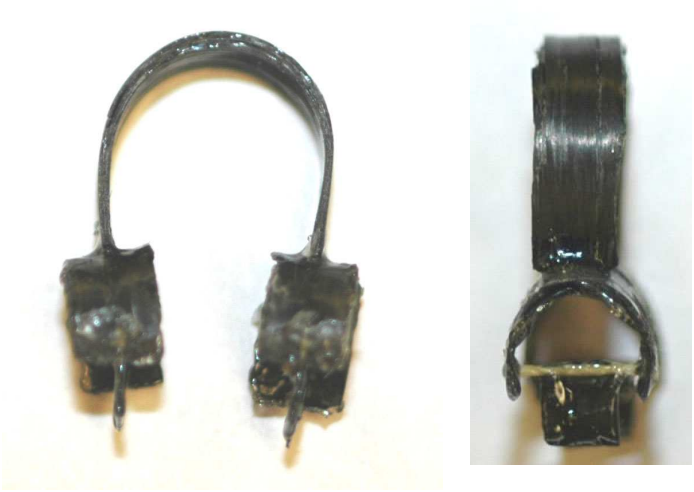

Figure 3.8: Front and side view of carbon fiber dynamometer spring.

it was connected to the setup and the Driver deflection was monitored. Since the same Driver was always used, its stiffness was measured a priori ($k_{Driver} = 475$ N/m at 125V, chosen to be the neutral position of the dynamometer). If the DUT tip displaced x_1 and the Driver displaced x_2 and had stiffness k_{Driver}, the stiffness of the connecting spring k_{sp} was

$$k_{sp} = \frac{k_{Driver} x_2}{x_1 - x_2} \tag{3.21}$$

Noticing that this expression requires the subtraction of two rather small displacements in its denominator, the stiffness of the connecting spring was matched to the Driver actuator so that the expression in (3.21) does not vary widely with small displacement errors (average $k_{sp} = 400$ N/m).

Estimations were made for the effective mass and damping of the spring through frequency analysis. It was found that the spring mass is on the order of 10^{-6} kg and the connecting spring damping is on the order of 10^{-5} Ns/m. For $\omega_o = 628 rad/s$ (100Hz), DUT amplitude $A_1 = 100\mu m$ and Driver amplitude of $B_1 = 150\mu m$, the energy per cycle measured by the spring is approximately 19 μJ. Up to the 10th harmonic (n=10), the sum of the energy input into the mass and damping of

the connecting spring is less than 10% of the energy measured by the spring, so both can be validly disregarded below a frequency of $n\omega_o = 6283 rad/s$.

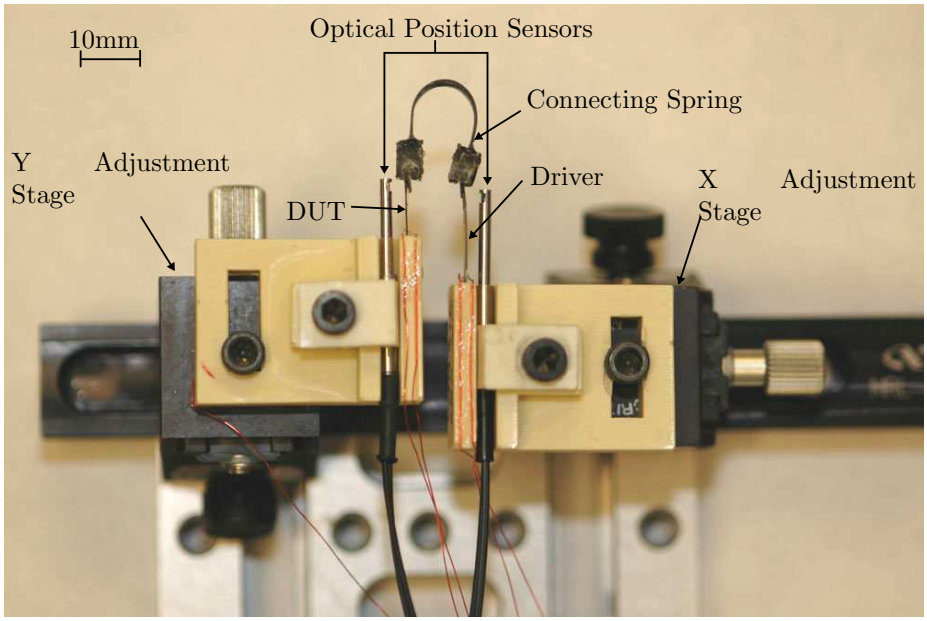

Figure 3.9: Picture of dynamometer test setup.

3.3 Testing Methods

The scheme shown in Fig 3.10 was used to drive the DUT. The scheme is denoted a "simultaneous" driver as the relative field on both PZT plates is controlled by V_d while V_b is constant, as discussed in [73]. For all tests, the minimum bias (V_b) used was 310 V. The drive voltage V_d had a DC offset of 155V for tests where the amplitude of the drive voltage was 125V or under. For example, for a drive amplitude of 125V, the drive voltage V_d would swing between 30V and 280V. This keeps a minimum of 30V bias on each PZT plate shown in Fig 3.10 to keep the polarization in the correct direction. In past experiments, it was noticed that mechanical depolarization can reduce the performance of bimorph bending actuators; this minimum electrical polarization field is meant to alleviate the issue. For drive amplitudes more than 125V, the bias voltage V_b and the DC offset

on the drive signal V_d are increased to always have a minimum of 30V on each PZT plate in the correct polarization direction.

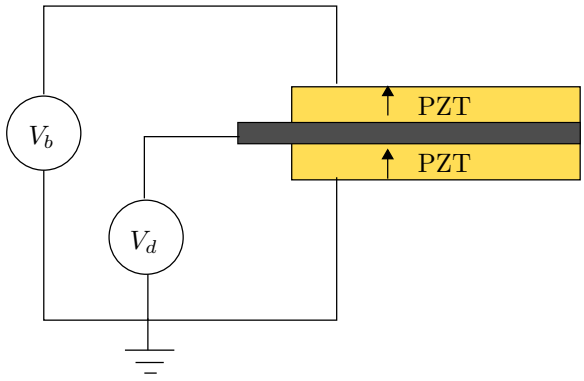

Figure 3.10: Voltage drive scheme for test actuators. The arrows indicate the polarization direction of the PZT-5H. The bias voltage is denoted V_b and the drive voltage V_d.

To control the DUT and Driver actuator voltages and to monitor the sensor outputs, Matlab XPC Target running on a standalone acquisition computer was utilized along with a Quanser Computing Q8 A/D D/A real time control board. The real time computer was sampling at 15kHz, well above test frequencies. As mentioned earlier, the positions of the two actuators were monitored by analog signals from custom optical reflective position sensors [57], which have bandwidths over 3kHz.

3.3.1 Iterative Resonance Technique

For a given sinusoidal drive on the DUT, a range of sinusoids at the same frequency on the Driver makes the DUT resonate at different amplitudes. DUT resonance is defined as the drive voltage of the DUT being 90 degrees out of phase with the position of the DUT. If estimates of the Driver stiffness, damping, mass and the DUT stiffness, damping, and mass along with the connecting spring stiffness could be made, an analytical prediction for the Driver signal for resonance could be made. The beauty of the iterative method described here is that no knowledge of any these variables except the Driver stiffness at a constant voltage is necessary to extract power output.

In the iterative technique for resonance, first the DUT drive sinusoid amplitude is fixed (and called 0 phase). An amplitude of the Driver is then chosen that results in approximately the motion amplitude of the DUT that is desired. The phase of the Driver is then tuned until the DUT position and voltage input are 90 degrees out of phase. When the resonance condition is achieved, the amplitude of the DUT can change considerably, so the drive amplitude of the Driver is tuned and the phase is iterated further until resonance at the desired amplitude is achieved. The energy output at this condition is now calculated with (3.18) using the positions of the two actuators and the spring constant of the connecting spring.

3.4 Dynamometer Verification

Once the dynamometer was constructed, some simple test cases were used to verify that it was behaving as desired.

3.4.1 Bandwidth Verification

The bandwidth of the entire system was tested when the DUT and Driver were simultaneously connected through k_{sp}. As can be seen from Fig. 3.11, the resonant frequency of the system was approximately 320Hz, which satisfies the requirement of being over 100 Hz (note that the positions x1 and x2 are 180 degrees out of phase at DC due to the positive directions of the two displacements shown in Fig 3.2 being in opposite directions). The system had a very high mechanical Q; this means that it was very easy to excite the main resonant mode when driving at lower frequencies. Thus to avoid resonances from 2nd and 3rd harmonics of the drive, drive signals $<$ 100Hz were used. In practice, even driving the structure at 100 Hz excited some minor resonances. Second and 3rd harmonic compensation were injected, however, into the Driver actuator so that the overall output had negligible frequency content outside of the main drive frequency. It was a time consuming manual process to tune the higher harmonics out of the motion, so most of the tests were

run at 30Hz where excitation of higher harmonics in the system was minimal. Higher frequency drives are explored in a later section using manual harmonic tuning.

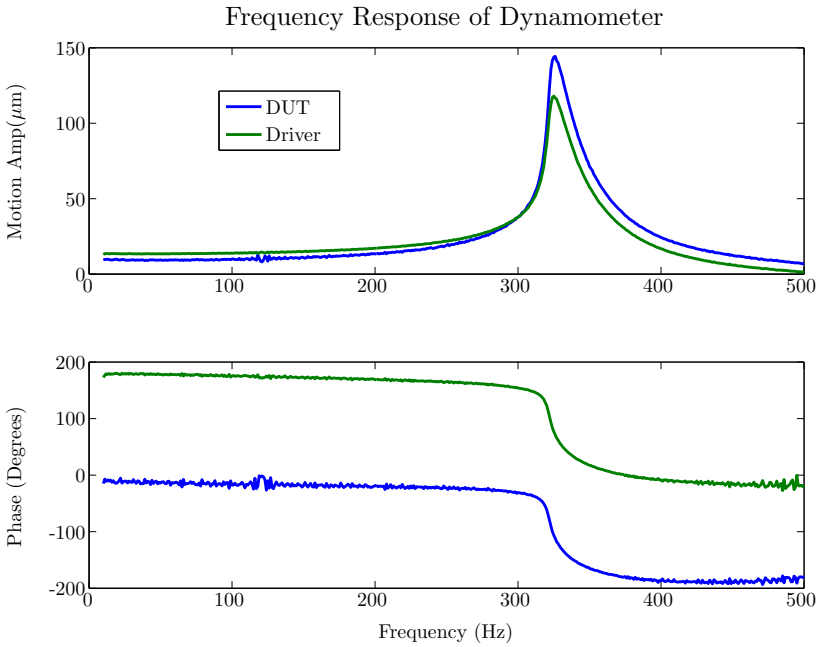

Figure 3.11: Bode plot driving the Driver actuator of the dynamometer. DUT plot is for position x_1 of Fig 3.2 and Driver plot is for position x_2 of Fig 3.2.

3.4.2 Verification of Maximum Power at Resonance

At resonance, the total spring and mass of a dynamic system not only produce and absorb no net energy per cycle (which is true of any periodic steady state system) but also have no reactive power. At the resonant frequency, the actuator needs to provide no force at any point during the cycle to keep a mass/spring system resonating. Under this condition, the actuator only performs work on its internal damping and the load damping. Therefore, if the energy output per cycle of the DUT is calculated from (3.15) (again only $W_{k,n}$ from (3.15) is included), a peak when the phase difference between the input voltage and the DUT position is 90 degrees should be observed. As seen in Fig. 3.12, indeed the power output of the DUT is maximum at a 90 degree phase difference within an allowable phase error (about 1 degree). To simulate resonance here and throughout these tests,

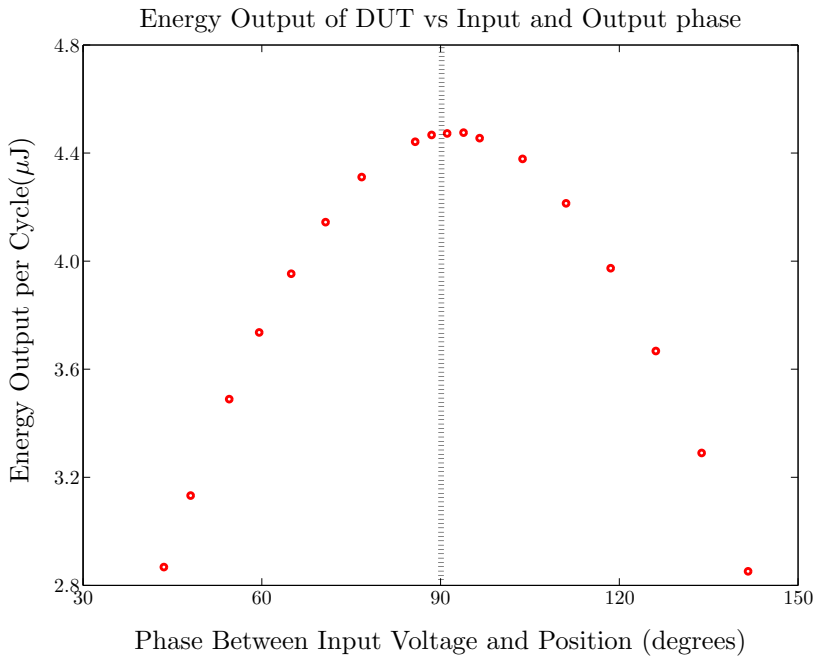

Figure 3.12: Verification of maximum power at resonance (90 degrees), 1 V/μm.

the driver actuator is adding virtual mass to the system to reduce its natural resonant frequency.

3.4.3 Sample Work Loop

A work loop was plotted in Fig. 3.13 to further verify the system's behavior. As one can see, the standard work loop curve is observed (see [11], [1] or [42] for more on actuator or muscle work loops). The useful work which is reported later in this paper (for this trial 5.9 μJ per cycle) is the area inside the work loop of Fig. 3.13. The shape of the work loop is not perfectly symmetric due to expected hysteresis.

3.5 Power Output Measurements

From the frequency response tests of [73], 10 mm, 10 mg actuators are expected to fracture at an average motion amplitude of 190 μm when resonating. Their fracture is governed by the externally applied load, applied field, and initial crack size along the edge of the piezoelectric plate.

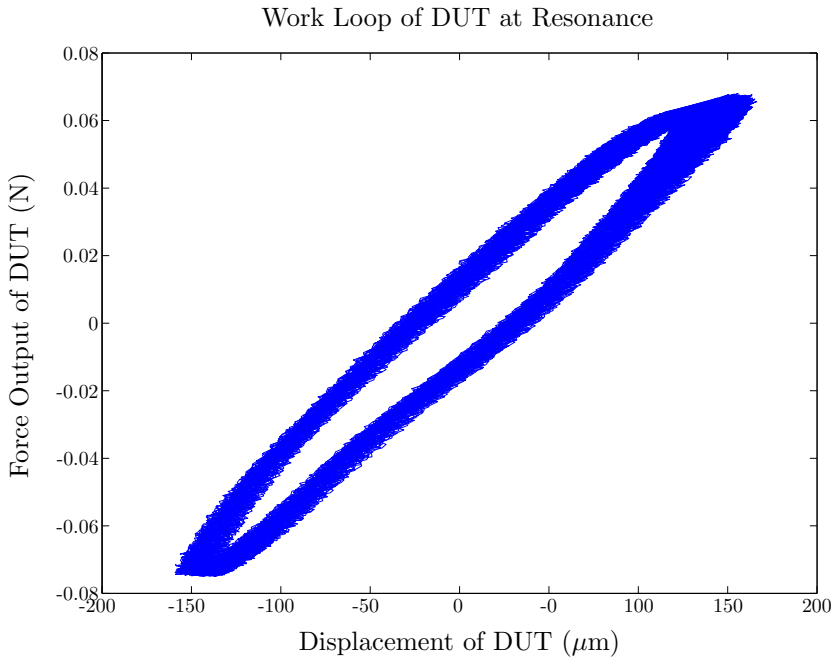

Figure 3.13: Work loop of DUT at 125V drive, 150 μm amplitude of displacement (30Hz). 5 seconds of unfiltered data is shown.

Since these variables are not always well known (especially initial crack size), the experimental motion amplitude for fracture of 190 μm is used rather than a fracture prediction. To make sure each actuator survives all the tests, a factor of safety is included here to only run the DUTs up to 150 μm of amplitude. The measured power output at simulated resonance (90^o phase shift) for each point at 30Hz for a typical 10mm actuator is shown in Fig. 3.14. At a fixed voltage, the simulated damping is sequentially reduced so that power can be measured at increasing DUT amplitudes.

Several interesting observations can be made from Fig. 3.14. First, one can see that the power output is saturating at very high (>125V) voltage amplitudes. Even though the power output is still modestly increasing, significantly more power output was not observed if the drive voltage is increased above 200V (1.6 V/μm); it was not increased above this value.

Using a simple linear system analysis, the data in Fig. 3.14 was fit to a linear model. At resonance, the internal force source of the actuator only does work on its own internal damping and the simulated damping introduced by the driver shown in Fig 3.15. At frequencies below the

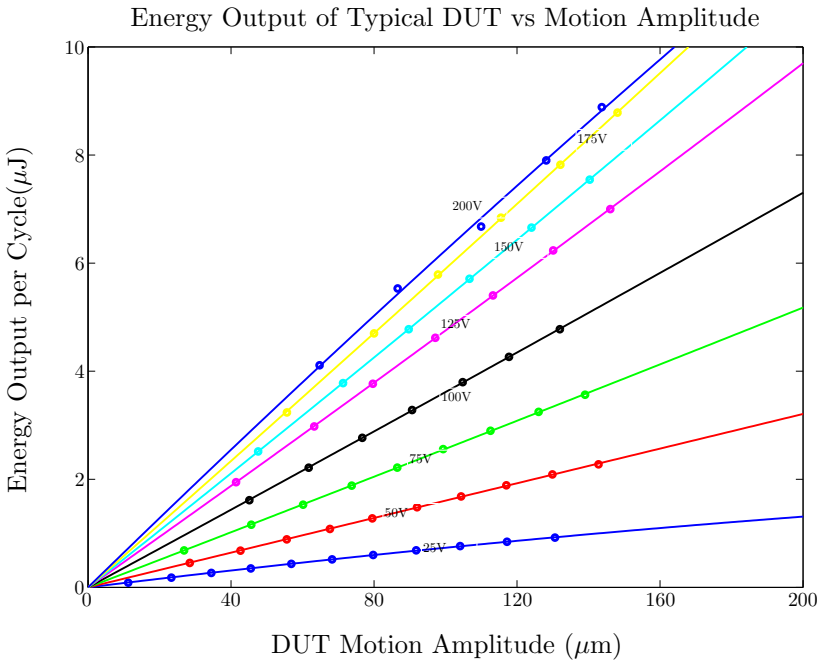

Figure 3.14: Typical power output curves for 10mg bimorph.

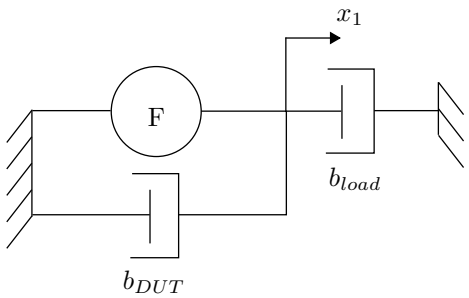

Figure 3.15: Block diagram of the system of Fig 3.5 when resonating.

resonant frequency of the device, the connecting spring mass and damping can be neglected. Below its bandwidth (approximately 1kHz), the driver actuator can be thought as just providing simulated mass to resonate the structure and a desired load damping, so its internal spring, mass, and damping can be neglected. This effectively reduces the 6th order system of Fig. 3.5 to a second order resonance and a simple second order analysis can be used.

With an internal actuator damping *bact* and a simulated load damping b_{load} the useful work output of the DUT is given by

$$W = b_{load} A_1^2 \omega^2 \int_0^T \cos^2(\omega t + \phi_1) dt = b_{load} A_1^2 \omega \pi \tag{3.22}$$

where A_1 is the oscillation amplitude of the DUT. At resonance,

$$F = (b_{DUT} + b_{load}) v_1 \tag{3.23}$$

If the internal force source of the actuator is linear, the work output of the actuator can be derived in terms of the internal damping of the actuator. For the work loop data of Fig. 3.13, the force amplitude of the DUT at the voltage drive frequency is approximately 11 times larger than the amplitude of the next highest harmonic (the second harmonic). The force source of the actuator was therefore assumed to linearly vary with the voltage input to the actuator, or

$$F = F(V) \cos(\omega t + \phi_1) \tag{3.24}$$

Combining with (3.23) and (3.22), the work output of the actuator for a given voltage drive is

$$W = [\pi F(V)] A - [\pi b_{DUT}] A^2 \omega \tag{3.25}$$

Fitting this model via least squares to the data yields the curves in Fig. 3.14. These curves are work output parabolas, and reach their maximum when the load damping matches the internal actuator damping. However, the peak of these parabolas would only be observed if the actuator could withstand much more than 150 μm of motion; only the very front edge of each parabola is observable. The parabola would reach its maximum value for much larger values of motion amplitude than can be realized due to actuator fracture. Therefore, b_{DUT} cannot accurately be extracted because the data is ill-conditioned to fit the amplitude squared term of (3.25) .

Energy output for 5 actuators was measured and plotted in Fig. 3.16. Deviation is observed

due to both measurement error and variations in hand assembly. To address variations in hand assembly, the slopes of the best fit lines (the linear part of (3.25)) are shown in Table 3.2. The slope mean is 0.0632 $\mu J/\mu m$ with a standard deviation of 0.0054 $\mu J/\mu m$ (or 8.54% of the mean slope). Deviation in actuator performance due to variation in assembly is therefore concluded to not be a significant performance issue.

Table 3.2: Variation in fit slopes for 5 actuators at 200V amplitude drive.

Actuator	Slope ($\mu J/\mu m$)
1	0.0591
2	0.0619
3	0.0641
4	0.0721
5	0.0590

Fitting just one slope line to all the data for the 5 actuators can address hand assembly variation and measurement error together. The linear part of (3.25) was fit to all the actuator data via least squares. The absolute value of the error from each data point to the least squares fit mean was calculated and divided by the least squares fit value at that specific amplitude to find a percentage error vector. The standard deviation of this percentage error vector is given in Table 3.3.

Table 3.3: Error characteristics for least squares fit to data in Fig. 3.16, n=5 actuators at 4 different voltage drive amplitudes.

Drive Amplitude Fit	Std. Dev. of % Error	Max Energy/Volt at 150μm Amp. (μJ/V)
50V	7.2	0.048
100V	8.3	0.052
150V	6.2	0.053
200V	7.7	0.047

3.5.1 Extrapolation to Higher Frequencies

All results presented thus far were run at 30 Hz to avoid bandwidth/harmonic limitations discussed in Section 3.4. To find the behavior of the actuator at higher frequencies, and to again verify that the spring mass and damper energy terms ((3.17) and (3.16)) are not needed, the DUT was driven at a constant voltage amplitude and kept at a constant displacement (in this case,

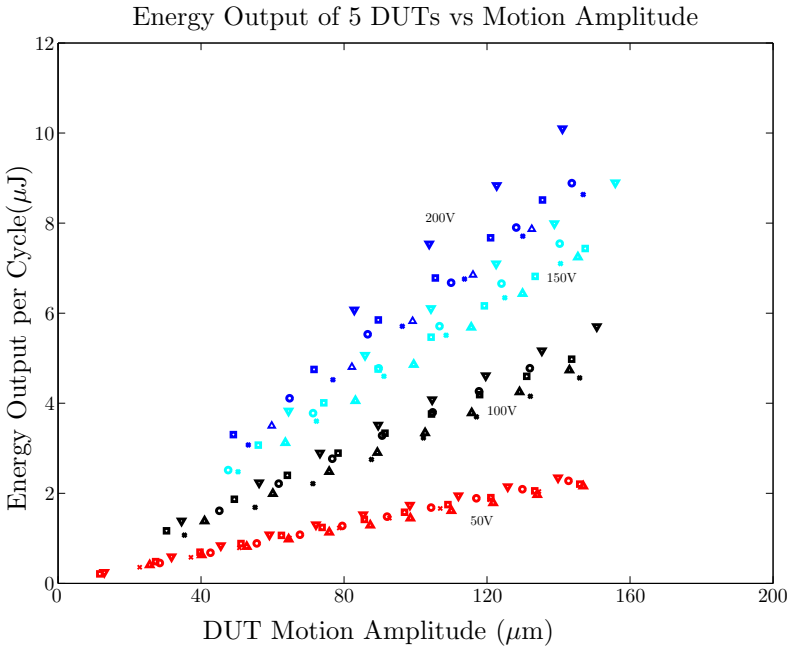

Figure 3.16: Power output for 5 different 10mm bimorphs.

125V amplitude drive, 100 μm amplitude displacement) with the Driver. The frequency was varied between 20 and 100Hz, and energy output of the DUT was taken at resonance (90° phase) for each frequency as seen in Fig. 3.17.

Fig 3.17 is the work done per cycle on the load damping, given by (3.22), not the work done by the DUT on its own internal damping. However, since the displacement and voltage drive are kept constant, for all frequencies the work output per cycle should be a constant and would equal the total work done by the internal force source of the DUT, or

$$W_{Total} = W_{b_{load}} + W_{b_{DUT}} = C \tag{3.26}$$

The internal damping in the DUT actuator, b_{DUT}, can then be extracted through a least squares fit of the slope of the data in Fig. 3.17, which is also plotted. When the two slopes are averaged, at 125V drive, $b_{DUT} = 0.0066 Ns/m$. This value corresponds only to a 3% loss in energy output from 20Hz compared with 100Hz for the 100 μm amplitude, 125V trial. It is important to

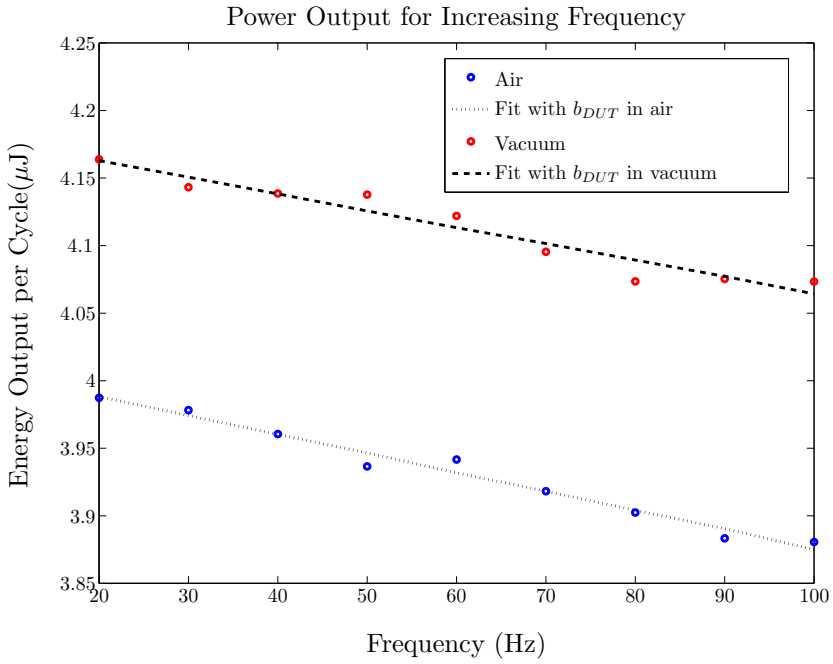

Figure 3.17: Behavior of dynamometer with increasing frequency.

note that again the mass and damping of the spring were neglected, so strictly speaking this value of b_{DUT} is an upper bound, but the mass of the spring is very small and its damping is negligible simply through its construction as discussed earlier.

3.6 Improvements to Actuator Performance

In recent findings [66], it was shown that a special cutting technique could reduce the size of edge cracks along the bimorph actuators which govern their fracture. The technique involved scoring the PZT-5H using laser micromachining, then cleaving the edge on the score line. When the actuators were assembled, the cleaved edge (most likely containing fewer or smaller microcracks) faced outward on the actuator, where the maximum strain takes place. In principle, this could increase the amplitude at which the actuators fracture and therefore increase their power density by allowing them to be run at higher displacement.

As seen from Fig. 3.18, the performance of the actuators made with this process improved

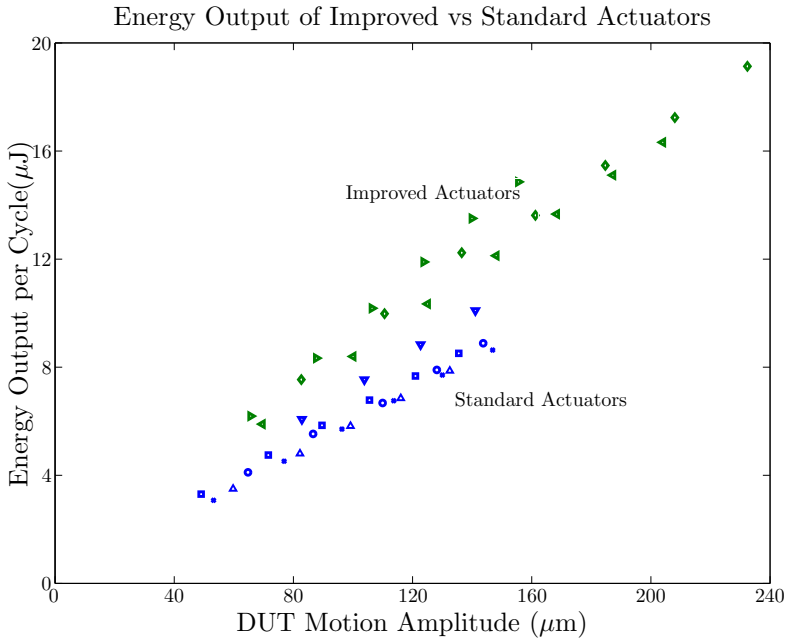

Figure 3.18: Comparison of improved actuator and standard actuator performance. Both were driven at 200V amplitude, 30Hz.

significantly, and not just by increasing the available displacement before fracture. In fact, the power output of the actuator was significantly better at all amplitudes. It is hypothesized that since the actuators are very small (1.5mm wide at the base), edge crack effects are probably very significant, thus performance can be improved tremendously by reducing these edge cracks through the mentioned cleaving process. Fig. 3.18 includes results from three of the improved actuators, but even a larger driver actuator than used in previous tests could not test these actuators to fracture. Therefore, the maximum energy output per cycle shown in Fig. 3.18 of 19.1 μJ/cycle is only a lower bound until the actuators can be tested to fracture. The standard actuators were easily fractured if tested beyond 150 μm.

3.7 Concluding Remarks

The results of the dynamometer power output measurements for miniature (10mg) piezoelectric bending actuators measured at AC are summed up in Table 3.4. Shown are average power output for several actuators of each type, with predicted results coming from [73]. As one can see, the predicted results extrapolated from DC measurements are indeed overestimates, especially when compared with the "standard" actuators. The improved actuators were not tested all the way to failure due to limitations in the Driver actuator; therefore the power output measurements are lower bounds for these actuators. The improved actuators are much closer to the predicted power output measurements than the standard actuators, but are still not as high performance as is predicted from DC.

One can also see that the internal damping of the actuator is not a significant source of loss. The actuator can in fact not be run in the matched condition at resonance in which the load damping and the actuator damping are equivalent, corresponding to maximal power transfer to the load damping. This condition would require very large deflections in the bimorph actuator which would far exceed the maximum strain the PZT can withstand and would result in cracking and failure.

Table 3.4: Energy output characteristics for 10mg piezoelectric bimorph actuators.

Parameter	Predicted in [73]	Standard	Improved
Mass (mg)	11.72	10.1	10.1
Energy Output (μJ/cycle)	27.5	9.5	>19.1
Energy Density (J/kg)	2.35	0.94	>1.89
b_{DUT} @ 1V/μm (Ns/m)	0.0052 [68]	0.0066	–

The power density of the actuators can now be addressed. A reasonable assumption for the power density of a whole hovering animal is 75 W/kg (laid out in Chapter 2). Using an insect as a model, 35% of an insect's total mass being flight muscle [14] implies a 100mg robot with approximately the same mass profile would need an actuator with a minimum power density of 200W/kg. With a flapping frequency of 275Hz, the "improved" actuators in Table 3.4 have a useful

work output at 200V drive of 4.7mW (including a 0.53mW or 11% loss from the internal damping of the actuator, assumed to stay the same from 125V drive up to 200V drive). This yields a power density of 467W/kg, easily satisyfing the design requirement of 200W/kg.

With PZT-5H being confirmed as a viable actuation source for mobile millirobots, several design rules can be offered for using piezoelectric bending actuators as the main power source for these robots. They are as follows:

- **Drive Structure at Resonance:** Considering that the PZT bending actuators have an elastic layer (only the elastic material in a unimorph but a combination of elastic material and the opposite PZT in a bimorph) that corresponds to a large internal spring that the PZT is working against, if the structure is not run at resonance much of the energy output of the PZT is transferred to the internal spring and is not useful work. Therefore, the robot should be run at resonance so that all the energy output of the PZT is used to drive the load in the form of damping.

- **Maximize Drive Frequency:** Since the internal actuator damping is very low, damping losses in the actuator are very low even at high frequency. Since the power output of the actuator is proportional to the drive frequency of the actuator minus these small losses, the drive frequency should be as high as possible to get maximal power output from the actuator.

- **Maximize Drive Amplitude:** The power output of the actuator is also proportional to the motion amplitude of the actuator; therefore this motion amplitude should be maximized as much as possible without fracturing the actuator. Even though the damping matched condition cannot occur due to premature fracture of the actuator, a transmission mechanism should be chosen so that the amplitude of motion is maximized for maximal power output.

Chapter 4

Redesign of the MFI

The MFI has been an active research project since 1998. The project has seen numerous design changes, from original corrugated wings and stainless steel flexures to the 2003 design incorporating carbon fiber composite through the invention of the SCM process. However, throughout these designs the MFI was iterated on a basic premise: a piezoelectric bending actuator driving a fourbar mechanism with a slider crank. This is basically the "power plant" of the MFI.

Although the MFI thorax has generated large amounts of thrust on a test base [55] in 2006, it has yet to generate a thrust to weight ratio greater than one on a scaled, mobile platform. The main difficulty with the design has been a lack of flapping amplitude, which as explained in the Introduction and Chapter 2 can be understood in terms of power delivered to the wing.

4.1 Past Designs in a Power Density Context

From Chapter 3, the power density of the 10mg piezoelectric actuators running at 275Hz and a drive amplitude of 200V is 467 W/kg. However, previous designs did not have access to either the actual power density delivered by the actuators or the newest, high power density bimorphs created through a small process change discussed in Section 3.6. Now that the power density of

both the newest actuators and the older bimorph actuators are known, previous designs can be examined in terms of power density.

The best lift value of the two degree of freedom wing flapping mechanism design discussed in Chapter 1 was achieved in 2006 from a structure denoted 06-β [2] [55]. This structure had a flapping stroke of approximately 80 degrees peak to peak (40 degrees amplitude) at a frequency of 275 Hz and produced 1400 μN of lift from a single wing, capable of lifting a mass of approximately 140mg (with two wings, 280 mg). However, the design utilized very heavy and large piezoelectric actuators, not the scaled 10mg actuators on the standalone MFI because it was just to be used for structure characterization, not liftoff. However, the power delivered to the wing can be calculated from data on this structure.

For an actuator driving a wing at resonance (i.e. only delivering power to the damping of the structure which here is only wing damping) through a transmission ratio T (in rad/m) connected between the linear actuator and the wing, power output can be estimated from results in [74]. In that work, it is shown that a bound on equivalent damping that the actuator sees is

$$B = \frac{2m_{MFI}gl_{wing}T^2}{\theta\omega} \tag{4.1}$$

where T is the transmission ratio relating actuator linear displacement and wing flap angle, l_{wing} is the length of the wing, m_{MFI} is the mass of the MFI, g is gravity, θ is the flapping amplitude, and ω is the flapping frequency in rad/s. The expression in (4.1) assumes that the maximum damping force on each wing is equal to twice the weight of the MFI and occurs at the distal end of the wing. This assumption has been shown to be reasonable through previous experiments, see [74].

Using the 06-β structural data in Table 4.1 and the fact that power delivered to a pure damper is equal to

$$P = \frac{1}{2}Bv_{max}^2 \tag{4.2}$$

Parameter	Value
Flap Frequency	275 Hz
Flap Amplitude	40^o
Transmission Ratio T	3200rad/m
MFI mass	100mg

Table 4.1: Structure 06-β flapping characteristics.

(where v_{max} is the maximum actuator tip velocity) yields an estimated power delivered to the air by the wing of 10mW. If an actuator were driving the wing through an ideal transmission, this is also equal to the total power delivered to the system by the actuator(s).

To find the actual power delivered by each actuator, it was assumed that the energy density of the large unimorph actuators used to drive the structure is similar to the energy density of the measured 10mg miniature bimorph actuators at an equal voltage drive level. The unimorph actuators weigh 125mg each, which means at a 275Hz operation frequency and energy density of 0.5J/kg at 100V drive amplitude (extracted from Fig. 3.14), they can each deliver 17.2mW. Considering there are 2 actuators driving a single wing, this means that there is approximately 34.4 mW of power delivered by the actuators into the structure. One obviously notes a discrepancy here between the approximately 10mW delivered to the wing and the 34.4mW delivered by the two actuators; in fact, this means that the mechanical drive structure connecting the wing to the actuators is only 29% efficient. This could possibly be attributed to losses in the transmission mechanism (mostly flexural damping losses), but the efficiency of the SCM created structure has been previously estimated at 90% in [56] through vacuum testing.

The large power loss is actually related to the dynamics of the system containing a differential and is further explained in [2]. With a nonzero stiffness connecting the two actuators (through the differential), most of the energy delivered to the structure is used to "fight" the dynamics that would resonate the structure at an undesirable, delayed or backwards wing rotation mode resulting in very little lift. This result is the main motivation for using a passive rotation system for the wing drive in upcoming sections.

If the best scaled 10mg actuators were used at 275Hz and a drive voltage amplitude of 200V (much higher than most experiments), each actuator would deliver 4.8mW to the structure for a total of 9.6mW. For an efficiency of 29% (again, the low efficiency is due to poor dynamic coupling, not limitations to the SCM process, see [2]), only 2.78mW would be delivered to the wing. Compared to the power of 10mW into the wing of structure 06-β, this is not enough power to flap the wing at 80 degrees. As has been seen in many failed structures leading to 06-β, very low flapping amplitudes (20 degrees) are observed when using the 10mg bimorphs due to a lack of power going into the flapping mode of the wing.

4.2 Recent Success of Single Actuator Flapping Mechanism

A 60mg flapping mechanism design by Prof. Robert Wood at Harvard [66] [67] implements several design improvements, including eliminating the "fighting" dynamics introduced by the differential, to produce a design capable of 120 degrees of flapping at 110 Hz. This device was measured to have a thrust to weight ratio of 2:1 and successfully lifted off, tethered, with guide posts. Prof. Wood's flapping mechanism is the first sub-100 milligram device to produce thrust greater than its weight on a platform with integrated actuators, transmission, and airframe and is pictured in Fig. 4.1.

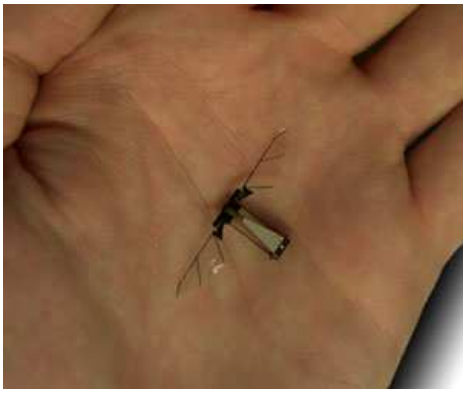

Figure 4.1: Prof. Robert Wood (Harvard) 60mg flapping mechanism from [30].

The Wood design utilizes a single cantilevered bending actuator in a bimorph configuration, as shown in Fig. 4.2. This actuator drives both wings through an amplifying dual fourbar system with very high transmission ratio from linear input to rotational flapping output. Passive rotation hinges (simple flexures with integrated joint stops at +/- 45^o) are used instead of a differential to allow the aerodynamic input to the wings to rotate them. The whole design is connected with an airframe ground element also composed of carbon fiber.

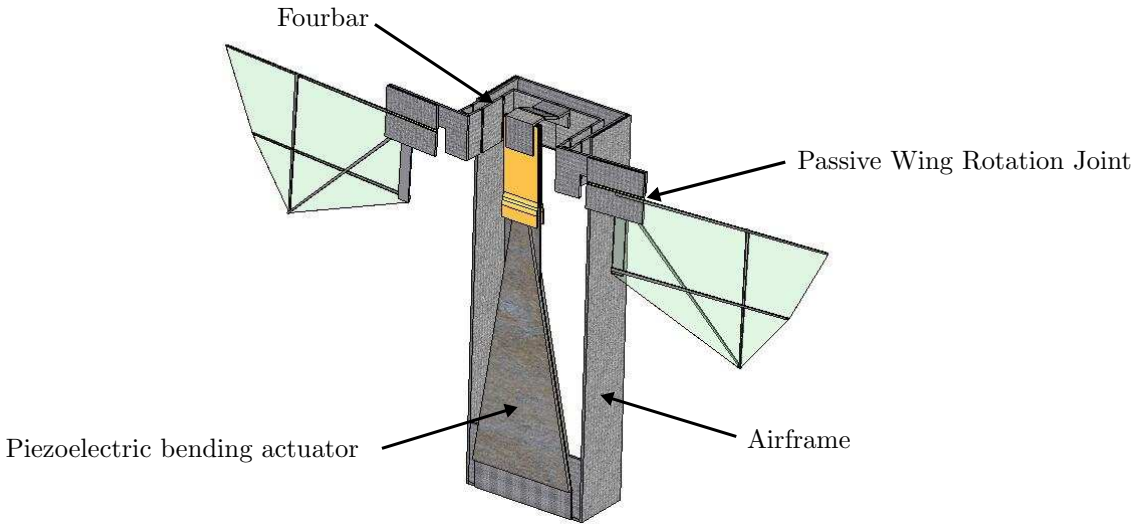

Figure 4.2: CAD model of Wood design (courtesy of Stanley Baek).

4.2.1 Problems in Wood Design

Though Wood's design has been a tremendous success in both proving the viability of micro-flapping UAVs and the SCM process through which it was manufactured, it is still a research project and several problems with the design are recognized. First, the flapping frequency is low at 110 Hz - this is mostly due to the low stiffness of its large cantilever actuator driving the structure. It is known that the power output per cycle for a piezoelectric bending actuator does not suffer significantly at high frequency (detailed in Chapter 3). Lift force is expected to increase as flapping frequency squared or even faster as wake capture becomes a larger source of lift at high frequency.

Therefore, to introduce more power into the air (consequently creating more thrust), the flapping frequency should be increased by either stiffening the actuator, lowering the (dominant) wing inertia, or even more drastically changing to a non-cantilever actuation mechanism.

Another possible problem with the design is its dependence on a large grounded airframe. At high speeds and high flapping amplitudes, it is quite difficult to create a ground that is actually stationary. In fact, ground elements have vibrated significantly in previous grounded designs; an ungrounded or "differentially" actuated scheme might be best here to not waste power in undesirable vibrating modes that either do not contribute to useful work output or in fact reduce the useful work output of the structure.

Finally, discussed in Section 4.4 in more detail, the strain profile of the PZT inherent in a bending actuator is not energetically advantageous; however, improving this would require a significant actuator change.

4.3 MFI Redesign Goals

Experience from years of MFI project work has taught a vast amount about engineering a small flapping mechanism. However, the previous MFI design has followed the paradigm of individual actuated flapping and rotation degrees of freedom, using a total of four actuators since 1998. In this and the following chapter, the "power plant" of the MFI is completely redesigned to take advantages of many of the past technological advances and discoveries. These discoveries (and experiences from the success of the Wood design) are summed up here in the goals for this new MFI.

- **Axial Straining Piezoelectric Element** Most importantly, the proposed design attempts to take advantage of the large power output gain in using an axially straining actuator rather than the bending actuator of Chapter 3. However, this is not a trivial change; it is quite difficult to amplify the small 0.1% strain that a material such as PZT-5H produces, especially considering the high forces that a large transmission ratio implies on the lightweight transmission elements

on the MFI.

- **Coupled Wing Input** Rather than having the two wings be driven by independent actuators as in the previous MFI iteration, it has been concluded that a single wing input is desirable for the system. This change eliminates the need to match two separate resonant systems for two wings (which has proven very difficult).

- **Passive Wing Rotation** As opposed to an actively controlled wing rotation design as for the last MFI iteration (utilizing a differential), passive wing rotation will be employed in the future MFI. Even though wing rotational timing is critical in producing adequate aerodynamic lift forces (especially when considering wake capture), the Wood design demonstrates that passive wing rotation can achieve very similar lift forces when compared to forced rotation. Passive wing rotation also greatly simplifies the design, not to mention eliminating the undesirable dynamic modes coming from the stiffness of the differential.

- **No Ground Element Design** Having a true ground present for a high Q, high frequency lightweight resonant system such as the MFI has proven not only difficult but counterproductive. Frame elements are required to be so light that they are not nearly strong enough to completely decouple vibrating sections of the structure; the entire structure vibrates in undesirable ways instead. The proposed design attempts to have no intentionally designed ground element that is required not to move; rather the entire structure should vibrate similar to the resonant thorax of an insect.

- **High Frequency Operation** The tremendous lift advantage (without significant penalty in actuator losses) due to high frequency flapping has already been demonstrated in structure 06-Beta. Flapping at a frequency greater than 200Hz is therefore a goal of the redesigned MFI.

4.4 Strain Energy Comparison of Bending vs Axial Mode PZT Actuators

If it is assumed that the energy output of a piezoelectric actuator is equal to the strain energy stored in the material itself, then several advantages can be deduced from different actuator morphologies. For instance, for a standard beam obeying Hooke's law $\sigma = E\epsilon$ (where σ is stress in the material, E is the Young's modulus of the material, and ϵ is the strain in the material), the strain energy stored in the material is equal to the work done on the beam during deformation and the beam can then do equal work in returning to its zero strain condition. Likewise, if the strain source is actually an internal mechanism like in a piezoelectric element, the work that the element is capable of performing is equal to the strain energy introduced into the system by the piezoelectric element.

For a standard axially strained material, the strain energy per unit volume for an axially strained beam of material is given by

$$D_U = \frac{1}{2}E\epsilon^2 \tag{4.3}$$

For a rectangular slab of PZT-5H actuated via an electric field to its maximum strain ϵ_{max}, the total strain energy (not the strain energy per unit volume) would be

$$U = \frac{1}{2}E_{pzt,11}\epsilon_{max}^2 wlt_{pzt} \tag{4.4}$$

where w is the width of the slab, l the length, t_{pzt} is the thickness of the piezoelectric, and $E_{pzt,11}$ is the Young's modulus of the ceramic in the 11 direction. A bending mode actuator, on the other hand, does not have a uniform strain profile as can be seen in Fig. 4.3. The maximum strain ϵ_{max} occurs only at the outer edge of the PZT surface. To quantify the strain energy difference between the axial and bending scenario, consider a PZT bimorph actuator with rectangular piezoelectric

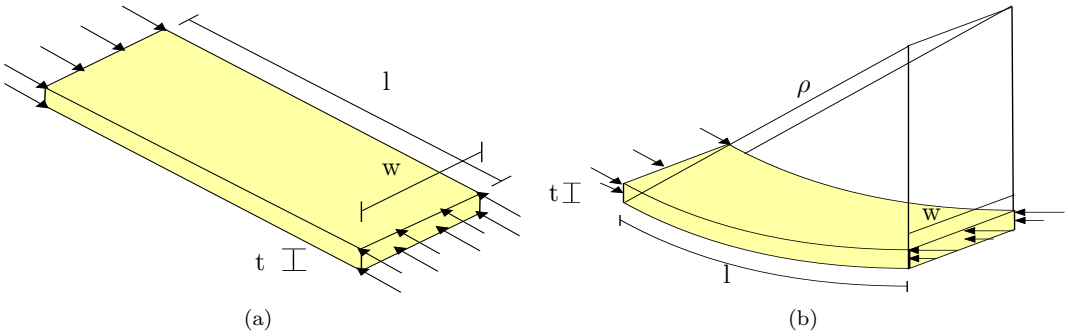

Figure 4.3: Strain profiles on piezoelectric layer for (a) uniform axial loading and (b) a bending load.

plates of length l, width $w/2$, and thickness t_{pzt}.

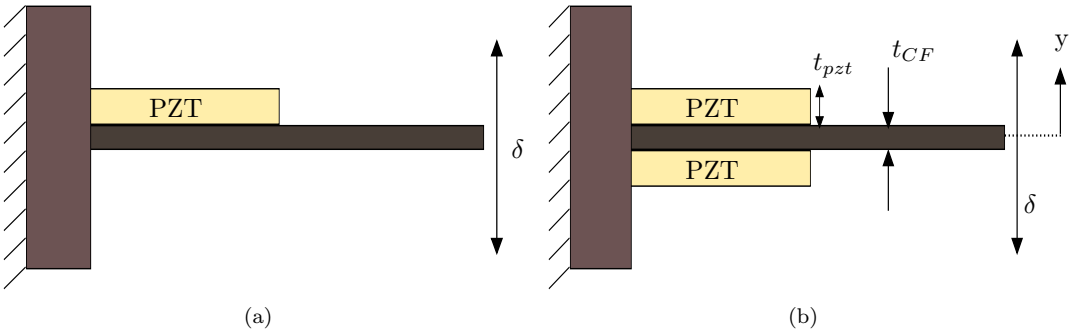

Figure 4.4: Unimorph (a) and bimorph (b) bending actuator configurations.

An important assumption that the bending actuator has a uniform radius of curvature was made for simplicity. This is only the case if the actuator is subject to a pure bending moment; one can also think of this assumption as having an infinitely long, infinitely rigid extension attached to a piezoelectric bender with a force applied at its distal end. This condition serves to make the strain uniform on the outer edge of the piezoelectric material; otherwise, for a rectangular plate in a bending configuration, there is a strain concentration at the base of the actuator. Other methods are available to assure this strain condition, such as varying the thickness of the PZT plate or varying the width such as in [73].

If the bending actuator has a uniform radius of curvature, then the strain in the PZT plate and the middle elastic layer can be expressed by

$$\epsilon = \frac{y}{\rho} \tag{4.5}$$

where y is shown in Fig. 4.4. The strain energy can then be integrated over the thickness of half the actuator as

$$U = \int_0^{t_{CF}/2} \frac{1}{2} E_{CF} \epsilon^2 w l dy + \int_{t_{CF}/2}^{t_{CF}/2+t_{pzt}} \frac{1}{2} E_{pzt,11} \epsilon^2 w l dy \tag{4.6}$$

Substituting the expression for strain in terms of y and ρ and performing the integration yields

$$U = \frac{1}{2} E_{CF} \frac{w l t_{CF}^3}{48\rho^2} + \frac{1}{2} E_{pzt,11} \frac{wl}{2\rho^2} [\frac{(t_{CF} + 2t_{pzt})^3}{24} - \frac{t_{CF}^3}{24}] \tag{4.7}$$

The first term (strain energy in the elastic layer) can be discounted noting that piezoelectric actuators need to be run in a resonant mode of the structure they are driving to be used effectively [56]. At resonance, the strain energy in the elastic layer is perfectly recovered because it cancels with inertial energy per cycle; only at DC must it be accounted for. Also knowing the boundary condition at the surface of the piezoelectric layer

$$\epsilon_{max} = \frac{t_{pzt} + t_{CF}/2}{\rho} \tag{4.8}$$

yields an expression for the total strain energy in one half of the bimorph actuator; it must be multiplied by 2 to account for both layers, yielding the final expression

$$U = \frac{1}{12} E_{pzt,11} w l \epsilon_{max}^2 [t_{CF} + 2t_{pzt} - \frac{t_{CF}^3}{(t_{CF} + 2t_{pzt})^2}] \tag{4.9}$$

The ratio of the performance of the axial mode actuator to the bending mode actuator is simply

$$\frac{U_{axial}}{U_{bending}} = \frac{6t_{pzt}}{t_{CF} + 2t_{pzt} - \frac{t_{CF}^3}{(t_{CF}+2t_{pzt})^2}} \tag{4.10}$$

It is interesting to note that the limit of (4.10) as the thickness of the elastic layer becomes large is 1; this is expected since if the two bending plates are infinitely spaced, their strain profiles would be rectangular. For a quantitative example of a typical value, consider an actuator with a single carbon fiber layer ($t_{CF} = 40\mu m$) and PZT thickness of $125\mu m$. For this case, the ratio of Eq. 4.10 is equal to approximately 2.6, meaning that the axial mode actuator can output 2.6 times more energy per cycle than the bending actuator.

It must be remembered that the assumption of a uniform bending radius for the actuator has made this factor of 2.6 a lower bound. In reality, there is a stress (and strain) concentration at the base of the actuator because the load is not purely a bending moment. This reduces the total strain energy in the bending configuration because the maximum strain is limited by the strain at the base rather than having a uniform maximum strain along the length of the piezoelectric material.

4.5 Proposed Design

The factor of 2.6 in energy or power output of the actuator could lead to a much improved flapping platform if it can be harnessed. Assuming the PZT can be properly clamped so that 0.1% strain can be realized, several amplification mechanisms must be employed to utilize the increased power density and flap the wing through a desired angle of 90 degrees. Previously, the total transmission system was a combination of a bending mode in the piezoelectric connected by a slider crank to a linear to rotational converting fourbar mechanism. However, as has been previously discussed, the first bending stage is a source of significant energy output loss and reduction in resonant frequency. Several alternative amplifying modes were considered; eventually a flextensional amplifying mode was chosen for the first actuator stage.

4.5.1 PZT Amplifying Mechanisms

There are many existing methods for amplifying small PZT deflection into larger output motions. A full review of available technologies is beyond the scope of this thesis but can be found in [43] and more recently in [44]. These methods can be broken down into several classes, including bending mode actuators (unimorph and bimorph benders as well as RAINBOW [25] actuators), flextensional actuators (such as moonie [59] and cymbal [13] actuators), and frequency-leveraged actuators such as the Inchworm actuator [38].

As shown in Section 4.4, bending mode actuators have an associated energy output cost that probably cannot be tolerated for miniature flying robots. Frequency-leveraged actuators are not only bulky and difficult to control but also do not have the bandwidth needed for a flapping device. Some flextensional geometries, on the other hand, are high frequency, compact devices that are appropriate for integration into the MFI.

Moonie actuators are cylindrically shaped actuators in which a piezoelectric stack is sandwiched between two end caps with a shallow cavity in between. As the stack displaces, the end caps flex, producing an amplified motion. A diagram of a moonie actuator from [45] is shown in Fig. 4.5. However, a cylindrical shape combined with the difficulty of attaching to a three dimensional flexing element makes the moonie actuator not easily integrated into MFI technology.

However, the related cymbal actuator is a very appropriate geometry. In a cymbal actuator, a cylindrical stack actuator is sandwiched between two conical metal endcaps as shown in Fig. 4.6. Several different metals were used for the endcap amplifying mechanism as discussed in [13]. Though the cymbal actuators discussed there are much heavier and larger than can be used in the MFI, the cymbal actuator geometry is modified in following sections so that it can be successfully integrated into the context of SCM for the MFI.

The basic cymbal actuator uses “side beams” near their singularity sandwiching a linear actuator. As the linear actuator contracts, the side beams get pushed outward, amplifying the input motion due to their proximity to a singularity. A commercial implementation of a cymbal actuator

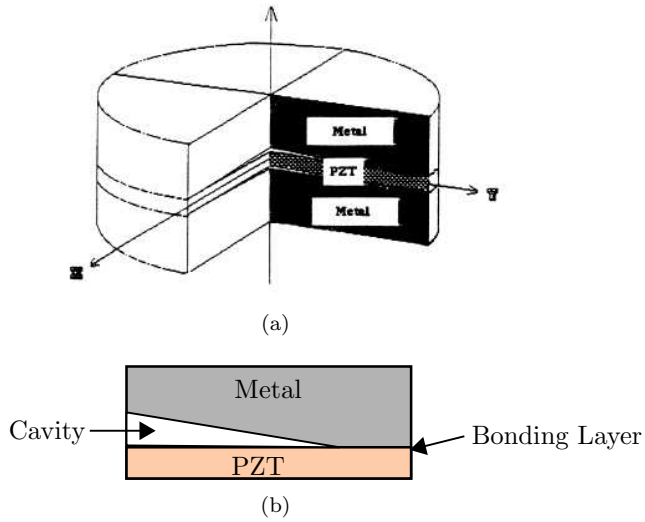

Figure 4.5: Diagram of a cylindrical moonie actuator from [45].

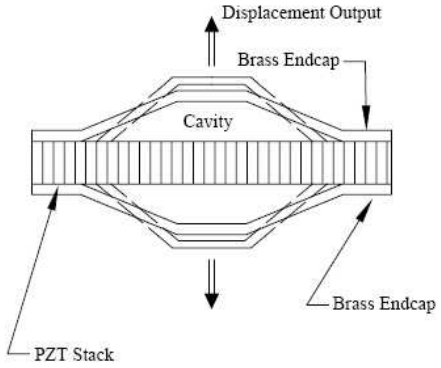

Figure 4.6: Diagram of a cymbal actuator

is shown in Fig. 4.7, made by Cedrat Inc.

This is the basic idea extracted from the cymbal actuator here; unlike the cymbal actuators, stack actuators were not used due to their heavy weight. Rather, two thin piezoelectric plates operated in their d_{31} mode were used in place of the stack actuator and carbon fiber composite was used in place of the metal side beams of the standard cymbal actuator.

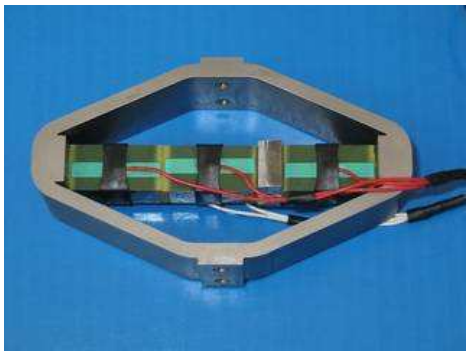

Figure 4.7: Cedrat APA120ML 130μm, 1400N actuator (from [32])

4.5.2 Transmission Ratio Analysis for Flextensional Geometries

The flextensional geometry of the main MFI core allows for several design choices, the most notable of which is the geometry of the amplifying side beams. Although the number of side beam shapes is limitless, there are two main classes one can consider: distributed compliance and concentrated compliance beams. In a distributed compliance beam, the entire length of the beam is allowed to deform and treated as an elastic member. Fig. 4.8 shows three different reasonable shapes to be considered for side beam geometries. The ends of all these beams are clamped. The input to the structure is Δy and the output is Δx.

Fig. 4.9 shows two concentrated compliance side beams. In other words, these structures are comprised of stiff beams connected by pin joints (or for this case, flexure elements). Bending only takes place in the flexural elements; the connecting members are considered to be infinitely stiff. The input and output are again Δy and Δx, respectively.

It is not difficult to examine all the cases above for transmission ratio. Obviously, a large transmission ratio is favorable considering that only microns of motion need to be amplified to a large flapping angle. The shape of each beam is modeled analytically with trigonometric functions as follows:

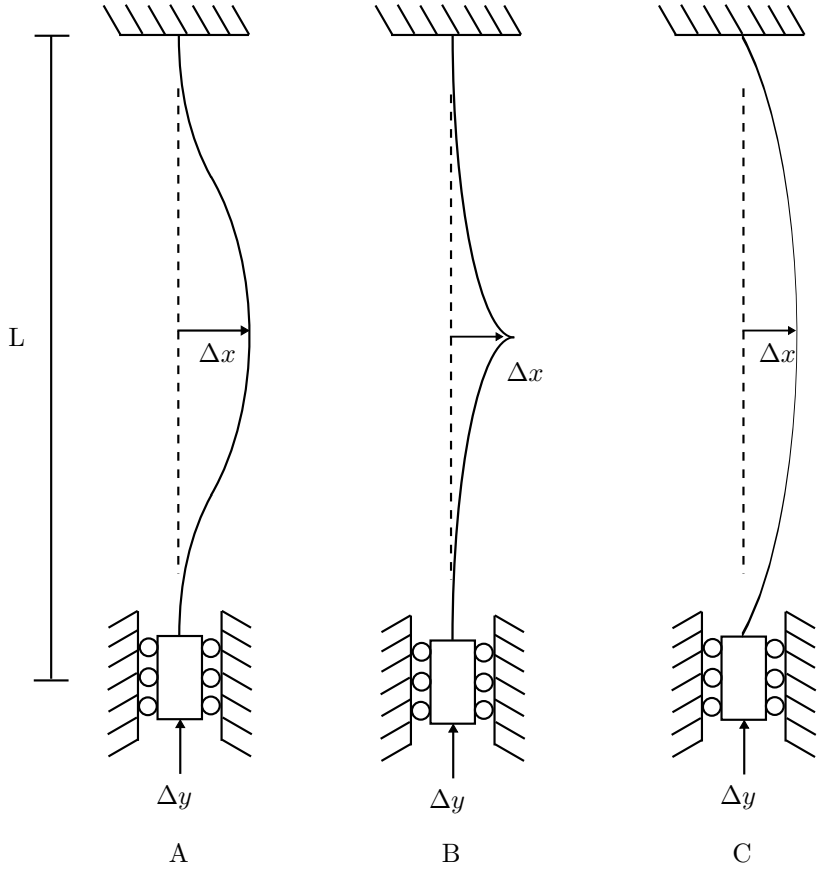

Figure 4.8: Three different distributed compliance beam shapes.

$$x_A = \frac{\Delta x}{2}(1 - \cos[\frac{2\pi y}{(L - \Delta y)}]) \tag{4.11}$$

$$x_B = \Delta x(1 - \cos[\frac{\pi y}{(L - \Delta y)}]) \tag{4.12}$$

$$x_C = \Delta x \sin[\frac{\pi y}{(L - \Delta y)}] \tag{4.13}$$

where the x direction specifying the shapes (x_A, x_B, and x_C) is the Δx axis. Note that

$$ds^2 = dx^2 + dy^2 \tag{4.14}$$

or

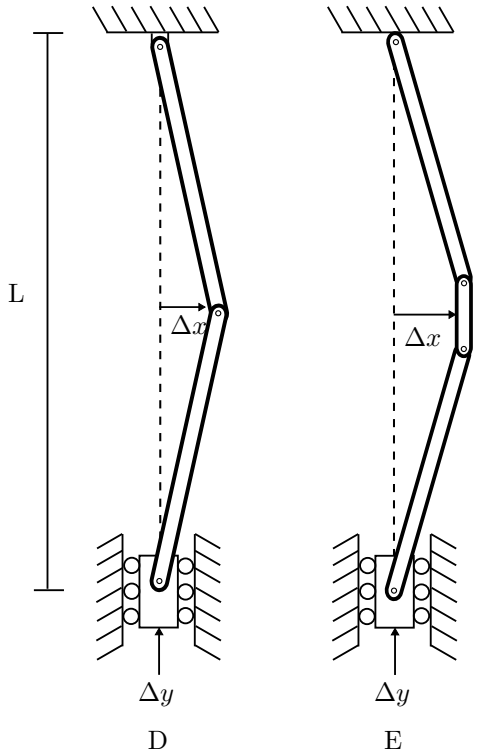

Figure 4.9: Two concentrated compliance diagrams, approximated by pin joints and rigid links.

$$ds = \sqrt{dx^2 + dy^2} = dy\sqrt{1 + (\frac{dx}{dy})^2} \tag{4.15}$$

Using the analytical expressions for x(y) above and noting that the length of the beam is invariant yields

$$\int_0^{L_{beam}} ds = L_{beam} = \int_0^{L-\Delta y} \sqrt{1 - \frac{dx}{dy}^2}\, dy \tag{4.16}$$

Considering the case where the beam is always near its singularity, a 2nd order series expansion of the square root function about 0 was used to find

$$L_{beam} = \int_0^{L-\Delta y} 1 - \frac{1}{2}\frac{dx}{dy}^2\, dy \tag{4.17}$$

Now the analytical expressions for x(y) can be substituted to find that surprisingly, for all the cases in Fig. 4.8,

$$L_{beam} = L + \frac{\pi^2 x_0^2}{4L} \tag{4.18}$$

where x_0 is the initial prebend distance of the beam. This finally yields the expression

$$\Delta x = \frac{1}{\pi}\sqrt{L - \Delta y}\sqrt{\frac{\pi^2 x_0^2}{L} + 4\Delta y} \tag{4.19}$$

Again, this expression is true for all cases of x(y) in Fig. 4.8. For the concentrated compliance cases of Fig. 4.9, the same analysis is used with the expressions

$$x_D = \frac{2\Delta x}{L - \Delta y} y \tag{4.20}$$

$$x_E = \frac{2\Delta x}{L - b - \Delta y} y \tag{4.21}$$

for the displacement relations (up to length L/2). The same analysis as above can be used without the square root approximation (it is an exact solution for these cases) to find

$$\Delta x = \sqrt{L - \Delta y}\sqrt{\frac{x_0^2}{L} + \frac{\Delta y}{2}} \tag{4.22}$$

for case D and

$$\Delta x = \sqrt{L - b - \Delta y}\sqrt{\frac{x_0^2}{L - b} + \frac{\Delta y}{2}} \tag{4.23}$$

for case E. Fig. 4.10 compares the distributed compliance case to the concentrated compliance cases in D and E using L = 20mm, b = 2mm, and maximum Δy = 0.1%(L) = 20μm. As one can see in the figure, the concentrated compliance cases have a larger transmission ratio than the distributed

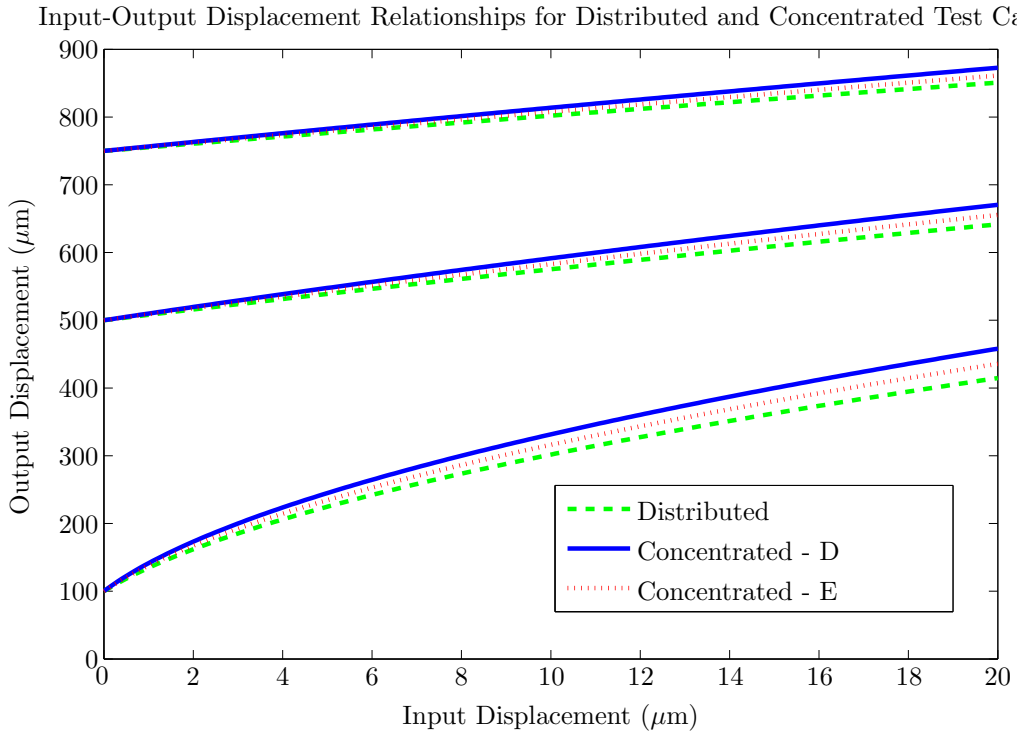

Figure 4.10: Input-output displacement relations for distributed and concentrated compliance test cases.

compliance cases. For the "prebend" distances in Fig. 4.10 (100, 500, and 750 μm), the triangular concentrated compliance case of Fig. 4.9 has higher transmission ratios than the case in E. The difficulty with case D is attaching to the output link since it is both displacing and rotating; this is discussed further in Chapter 5.

Besides a larger transmission ratio, another advantage of using a concentrated compliance rather than distributed compliance is in serial stiffness of the device. If the input to the structure (Δy) is blocked and a load is applied to the output of the amplifying side beam along Δx, serial stiffness can be defined as force applied over the back driving displacement Δx. Ideally, no displacement would be observed, or serial stiffness is infinite. However, especially for the beams in Fig. 4.8A and B, the serial stiffness is most likely not infinite in the real case because the bases of the beams are subject to large shear forces at the ground connection, which most likely deforms the

base and allow the output to deflect. However, in Fig. 4.9, the beams are not held normal to the load at the base, and a portion of the load is deflected along the beam rather than normal to it. In addition, since the distributed compliance beams are meant to bend throughout their length, their stiffness cannot be too high (to be actuated by the PZT to 90% of the unloaded PZT displacement, $k_{side} < 86000N/m$); this amplifies the effect of bending at the base since the beam cannot be rigid. The concentrated compliance beams can be made very stiff through most of their length; they need only be thin at the flexures.

4.6 Design Synthesis

A two stage transmission mechanism is proposed here to create a $> 80^o$ flapping amplitude. The first stage is the concentrated compliance flextensional mode discussed earlier. The second stage is a slider crank mechanism, taking the differential output from the flextensional stage to create a large wing flapping angle. The square geometry of the PZT actuator core provides the linear constraint of the moving bracket in the top of the Figure.

4.6.1 Actuator Core Design

Rather than using a heavy piezoelectric stack actuator, two PZT plates were used in their d_{31} actuation mode. One plate cannot be used alone because it would not have good stiffness properties in standard cantilever bending. A box structure shown in Fig. 4.11 was utilized to separate the two plates, making it stiff in all bending directions. Carbon fiber separating planks were used to keep the plates from bending in a 2nd order (rainbow-shaped) mode rather than actuating in an axial direction. PSI-5H4E from Piezo-Systems (properties in 4.2) was used for the piezoelectric actuation material. Dimensions of the piezoelectric plates are in Table 4.3.

The axial force output of a single plate of piezoelectric material in its d_{31} mode is given (from [62]) by

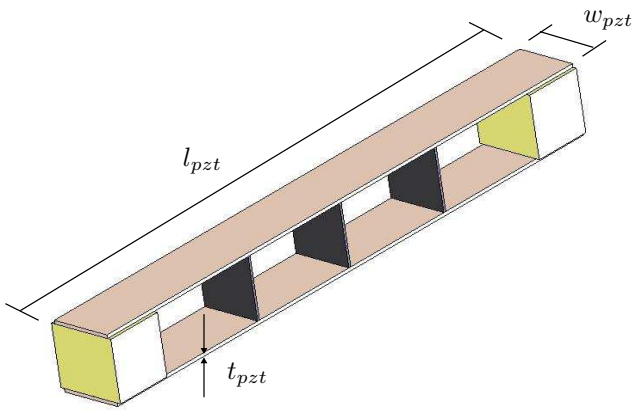

Figure 4.11: Solidworks model for the initial axial-mode actuator core.

Parameter	Value
Strain Coefficient d_{31}	$-320 * 10^{-12}\ m/V$
Force Coefficient g_{31}	$-9.5 * 10^{-3}\ Vm/N$
Elastic Modulus E_{11}	$6.2 * 10^{10}\ N/m^2$

Table 4.2: PSI-5H4E properties, from Piezo Systems [37].

Parameter	Value
t_{pzt}	125 μm
w_{pzt}	1 mm
l_{pzt}	20mm

Table 4.3: Actuator core dimensions.

$$F = d_{31} E_{11} w V \tag{4.24}$$

where d_{31} is the piezoelectric strain coefficient, E_{11} is the modulus of the piezoelectric material in the 11 direction, w is the plate's width, and V is the drive voltage on the plate. The stiffness of the same plate is

$$k = \frac{E_{11} t_{pzt} w_{pzt}}{l_{pzt}} \tag{4.25}$$

where E_{11} is the modulus of the material, t_{pzt} is its thickness, w_{pzt} is the width of the plate, and l_{pzt} is the length of the plate.

A single plate of piezoelectric material can be simply modeled by a voltage controlled force source in parallel with the internal spring coming from the modulus of the material, shown in Fig. 4.12. For the dimensions in Table 4.3, each plate can produce a blocked force of at 11.9N at 300V, and each plate has a stiffness of 775,000N/m. Therefore the entire core has a stiffness of $1.55 * 10^6$N/m with a blocked force of 23.8N. This would lead to an unloaded core displacement of 15.4 μm. It is important to note here, however, that experimentally a free plate of the PZT-5H displaces approximately 0.1% or 20 μm for a 20mm plate. This is due to softening of the material (or a reduction in the Young's Modulus) and an increase in d_{31} at high field [60][63]. Though only a linear model is offered here, it is important to note that a full 0.1% strain is observed from the piezoelectric material, so any analysis using the linear model is a lower bound on displacement.

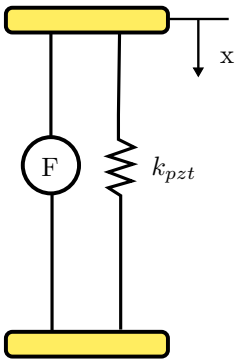

Figure 4.12: Simple model of piezoelectric material as a force source in parallel with a spring dependent on the modulus and dimensions of the material.

4.6.2 Transmission Analysis

A diagram of the entire transmission system to be used in the new MFI design is shown in Fig. 4.13. Two slider crank mechanisms are attached to the flextensional actuator output and are appropriately biased.

To find the input (x) to output ($\Delta\theta_3$) relationship for the transmission, the trigonometric relationships derived from Fig. 4.13

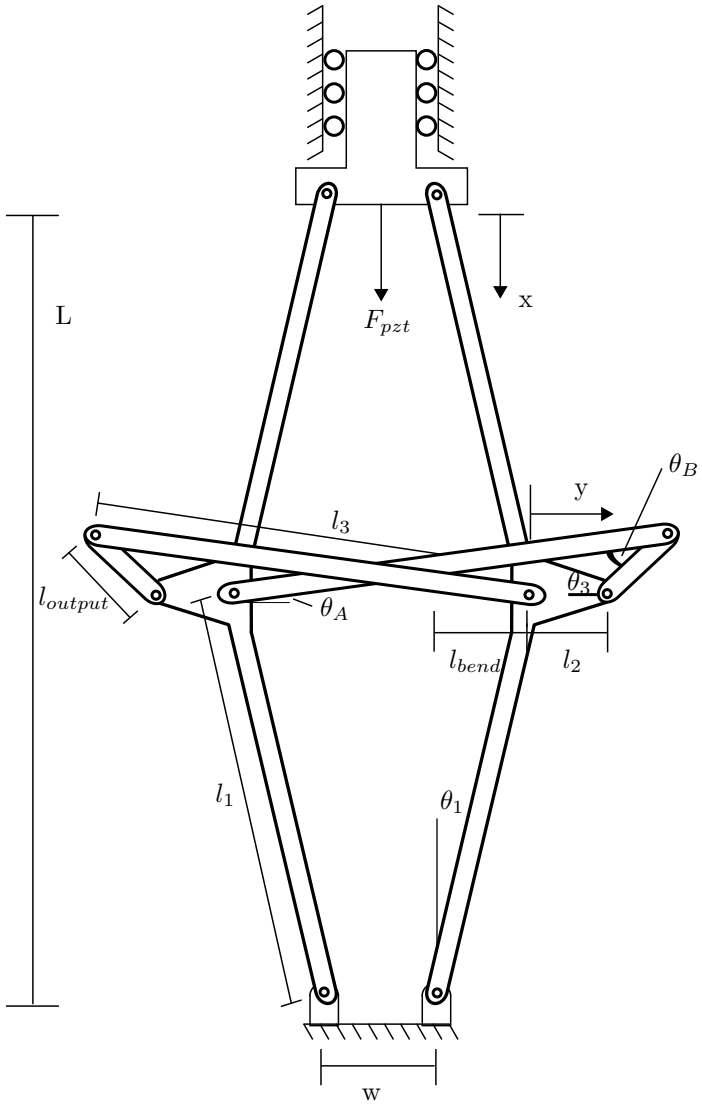

Figure 4.13: Initial design linkage diagram.

$$y = l_1 \sin(\theta_1 + \Delta\theta_1) - l_{bend} \tag{4.26}$$

$$l_3^2 = (2l_2 + 2l_{bend} + w_{pzt} + 2y)^2 + l_{output}^2 \tag{4.27}$$
$$-2(2l_2 + 2l_{bend} + w_{pzt} + 2y) l_{output} \cos(\theta_{3,0} - \Delta\theta_3)$$

were used. The total angle θ_3 in Fig. 4.13 is here broken down into its initial attachment angle

Parameter	Value
L	20mm
l_1	10.004mm
l_2	1mm
l_3	4.76mm
l_{output}	300μm
l_{bend}	300μm
θ_1	1.72^o
θ_3	120^o
w	2mm

Table 4.4: Transmission dimensions from Fig. 4.13.

$\theta_{3,0}$ and the change in angle $\Delta\theta_3$ such that $\theta_3 = \theta_{3,0} - \Delta\theta_3$. For the dimensions of Table 4.4, the relationship of x vs $\Delta\theta_3$ is plotted in Fig. 4.14 (the actual expression is quite long and is not presented here). As one can see, the relation between x and the output flapping angle $\Delta\theta_3$ is nearly linear. 15.4 μm of input displacement leads to 82^o of total flapping angle.

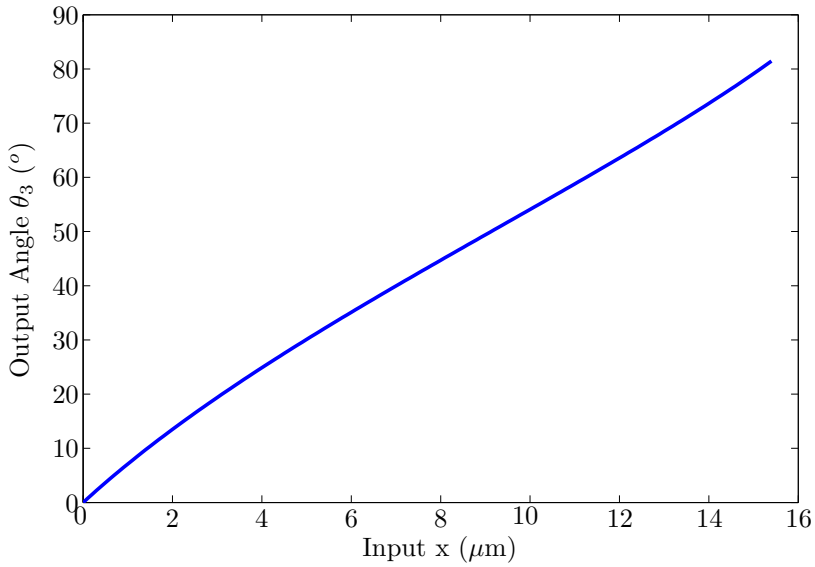

Figure 4.14: Transmission relationship x to $\Delta\theta_3$.

4.6.3 Entire System Stiffness

Considering the force of 23.8N available from the actuator core, it must be verified that this force can drive the proposed transmission structure shown in Fig. 4.13. It has already been

shown that 15.4 μm of input displacement leads to a large (82^o) flapping angle, but if the structure is overly stiff, the piezoelectric ceramic displacement saturates rather than move near its unloaded displacement of 15.4 μm.

The dimensions of Table 4.3 were again used and the relations

$$l_{output}^2 = l_3^2 + l_w^2 - 2 * l_3 l_w \cos(\theta_A) \tag{4.28}$$

$$\pi = \theta_A + \theta_B + (\theta_{3,0} - \Delta\theta_3) \tag{4.29}$$

$$\tag{4.30}$$

along with an expression for the total energy in the system U

$$U = x^2 k_{pzt} + 6k_{CF}\Delta\theta_1^2 + k_{rot}(\pi + \Delta\theta_3 - \theta_{3,0})^2 + k_{rot}\theta_A^2 + k_{rot}(\pi - \theta_B)^2 \tag{4.31}$$

to find the energy U in terms of x and the rotational stiffnesses of the flexures, which again are being used as part of the SCM process in place of the pin joints in Fig. 4.13. Here, it was assumed that the flextensional side beam flexures are made from 40 μm carbon fiber and the slider crank contains 7 μm kapton flexures. The stiffness of a rotational flexure is given from [28] by

$$k_{flex} = \frac{EI}{l_{flex}} \tag{4.32}$$

The rotational stiffnesses of the carbon fiber and kapton flexures were found with the dimensions in Table 4.5.

Using

$$\frac{\partial U}{\partial X} = F \tag{4.33}$$

Parameter	Value
E_{CF}	100GPa
E_{kapton}	3GPa
t_{CF}	40μm
t_{kapton}	7μm
$w_{CF,flex}$	2mm
$w_{kapton,flex}$	2mm
$l_{CF,flex}$	60μm
$l_{kapton,flex}$	100 μm

Table 4.5: Flexure dimensions for flexures approximating the pin joints of Fig. 4.13.

the input actuation force of the piezoelectric material could be found as a function of output angle. Plotting this up to the force expected from the PZT-5H of 23.8N results in the plot of Fig. 4.15.

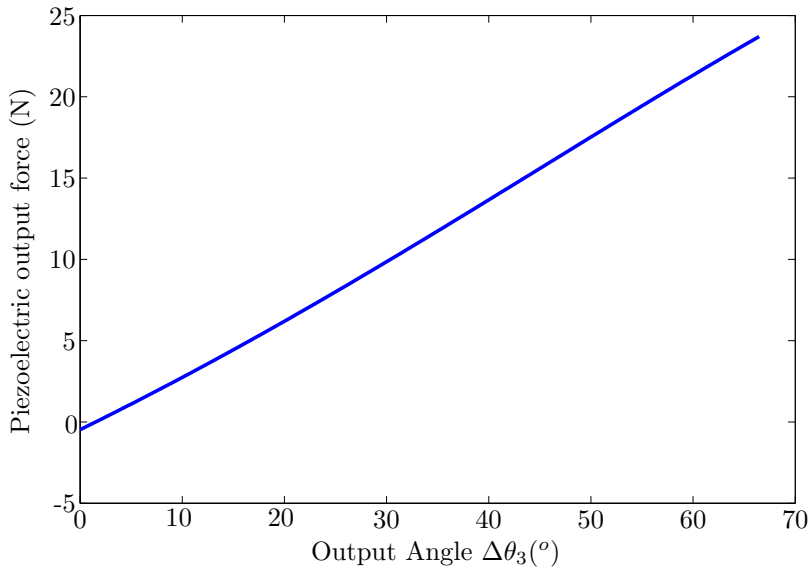

Figure 4.15: Input actuation force vs output flap angle.

Note that in Fig. 4.15 only 67^o of wing flapping is observed from the transmission. However, the reader is encouraged to note that this is strictly a lower bound on the flapping angle knowing that d_{31} goes up and the stiffness of the material goes down as the field is increased, leading to more deflection (again, 0.1% or 20μm instead of 15.4 μm, unloaded at DC). Also, when the structure is run at AC, wing flapping goes up at the resonant frequency (this is the Q factor). From previous designs with a resonant frequency of 250Hz, the Q is approximately 1.2; it is expected that since

the same inertially dominating wing is used and the resonant frequency is comparable, the stiffness and hence the Q factor will be comparable. These effects combine for an expected flapping angle of greater than 90 ^{o}.

It is also interesting to note that there is a net tension on the piezoelectric actuating plates when the design is at equilibrium. This is due to the slider crank mechanisms being attached with a bias in their flexures; however, this force is only 0.475N (corresponding to a stress of 1.9MPa or a strain of 31×10^{-6}), which means it does not have a significant effect on initial flapping angle of the wing or the overall stroke (it deflects the 20mm piezoelectric plate only 0.6 μm).

A CAD model of the entire design is shown in Fig. 4.16. Wings are not shown attached here, nor are passive rotation joints. The reader can relate the CAD model to the linkage diagram of Fig. 4.13 through the corresponding labels.

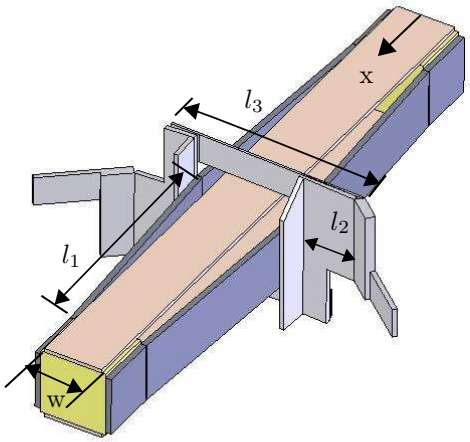

Figure 4.16: Solidworks model for the initial structure design.

Chapter 5

Construction and Testing of Axial Mode MFI

The design proposed in Chapter 4 is constructed and tested here. It is referred to as "Revision 1"; design improvements are suggested and implemented in what is called "Revision 2" also in this chapter. Construction and testing of Revision 1 was performed in a step by step basis by building onto a base component and testing each stage, the first component being the actuator core with a maximum motion of approximately 20μm. This was followed by addition of flextensional side beams, which have roughly a transmission ratio of 24:1 (even though the transmission is not strictly linear). Finally, dual slider cranks provide a transmission ratio of 3864 rad/m; the wing is attached to the slider cranks' output links.

5.1 Actuator Core

The actuator core (Solidworks model in Fig. 4.11) was constructed by molding two polyurethane rectangular end caps 2.25mm wide. These end caps were aligned on a flat surface and two piezoelectric plates (PSI-5H4E from Piezo Systems) were attached flat onto them with

cyanoacrylate glue. Carbon fiber plates were precisely laser cut to the exact spacing between the two plates and were glued vertically to prevent rainbow-shaped deflection of the plates. A completed actuator core appears in Fig. 5.1.

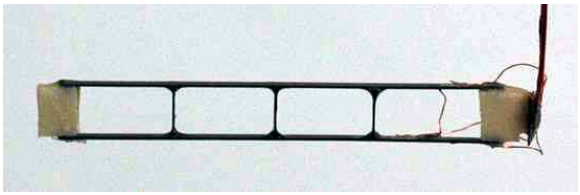

Figure 5.1: Constructed actuator core.

Deflection results for 8 actuator cores appear in Table 5.1. More than the predicted 15.4μm of motion (from chapter 4) is observed from the core alone. This is due to lowering of the Young's modulus of the material and an increase in d_{31} for the piezoelectric material when driven with high fields [60].

Parameter	Value
Cores tested	8
Peak drive voltage	250V
Peak drive field	2V/μm
Mean Deflection	18.47 μm
Standard Deviation of Deflection	0.62 μm

Table 5.1: Deflection data for 8 tested actuator cores.

5.2 First Amplifying Stage

The amplifying flextensional side beams were fabricated using an alignment and molding technique that allows a precise bias to be constructed into the beams so that the transmission ratio does not vary due to hand alignment and bending. As mentioned in Chapter 4, the amplifying side beams utilize carbon fiber flexures. The stiff link elements of the side beams were made by precisely stacking a total of seven layers of carbon fiber around one central layer that acts as the flexure where the stacks are not present. A diagram of a side beam before it is biased into its proper position is shown in Fig. 5.2.

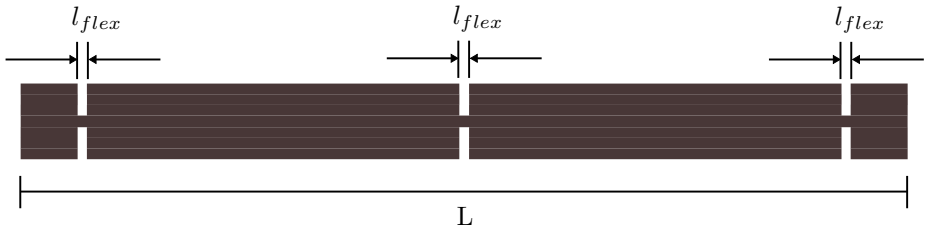

Figure 5.2: Diagram of side beam layup.

To align and stack the side beams, the pattern shown in Fig. 5.3(a) was laser micromachined into a piece of flat, 40 μm carbon fiber. After machining, the entire sample was slightly heated to soften the resin in the carbon fiber so that the beams adhere to one another. One continuous beam on the right (there are three extra shown in the Figure) was removed and placed on the cut beam section (shown in Fig. 5.3(b)). The beam was pressed down with teflon so that it adheres to the underlying layers. These two beams were then folded along the cut line to on top of the adjacent machined beam section and pressed with teflon (Fig. 5.3(c)). This process was repeated until there were three cut beam sections on both the top and bottom of the continuous beam.

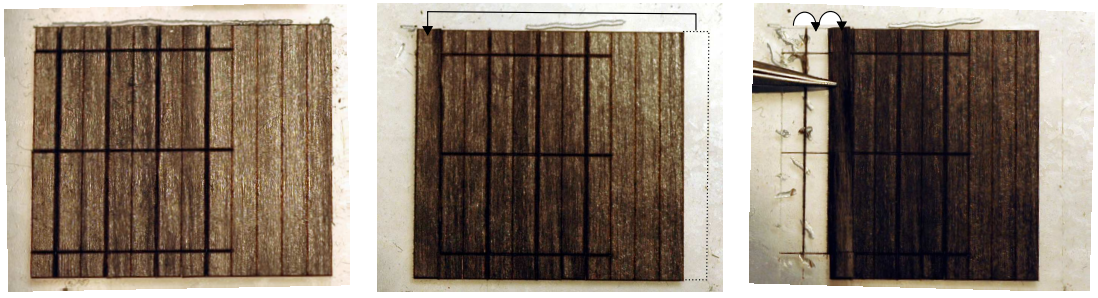

(a) (b) (c)

Figure 5.3: Side beam cut and folding process

Once assembled, the side beam layup was placed on a rubber mold that was created with a 3d Systems Thermojet printer and Dow Corning 3120 RTV high temperature rubber, shown from the top and side view in Fig. 5.4 (note the shape profile that is seen from the side view of the mold). The side beam layup was aligned on this mold; small amounts of polyimide were used to hold the side beam to the contour of the mold before it was placed in the oven. The molded assembly was vacuum bagged (details in Appendix A) to keep pressure on the entire assembly while it is cured.

When the beams were removed after the curing process, their relaxed position was now precisely the shape of the mold as shown in Fig. 5.5, where a) is a cartoon diagram of the shape of the beam and b) is the beam itself after curing and shaping, held in tweezers.

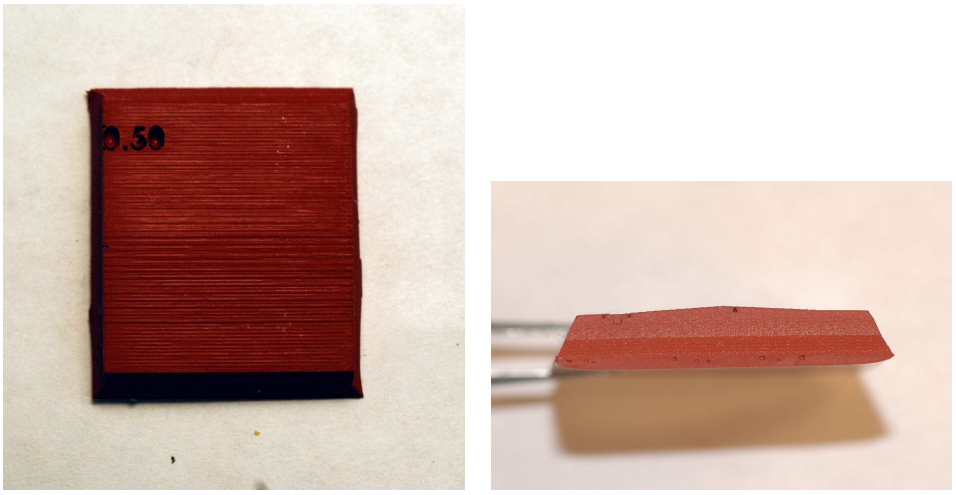

(a) (b)

Figure 5.4: Side beam mold top and side views.

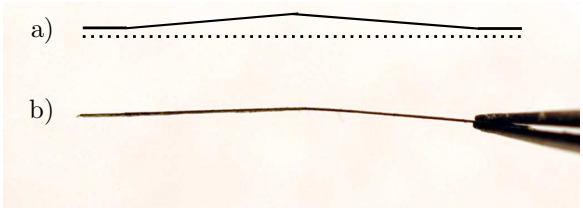

Figure 5.5: Side view of a) diagram representation of a cured side beam and b) actual cured side beam.

5.2.1 First Amplifying Stage Testing

Side beams designed in Chapter 4 with a bias of 300μm (equal to the distance l_{bend} in Fig. 4.13) were molded to be used as the flextensional side beam amplifiers. Two of these side beams were attached with cyanoacrylate glue to the plastic end caps of the actuator core, shown in Fig. 5.6. Two different 300 μm side beam cores were constructed and tested unloaded; displacement results are in Table 5.2. Considering the average displacement introduced by the experimental PZT

core of $\Delta = 18.47$ μm and the transmission expression for the flextensional stage

$$y = \sqrt{(L/2)^2 + l_{bend}^2 - (L/2 - \Delta/2)^2} - l_{bend} \tag{5.1}$$

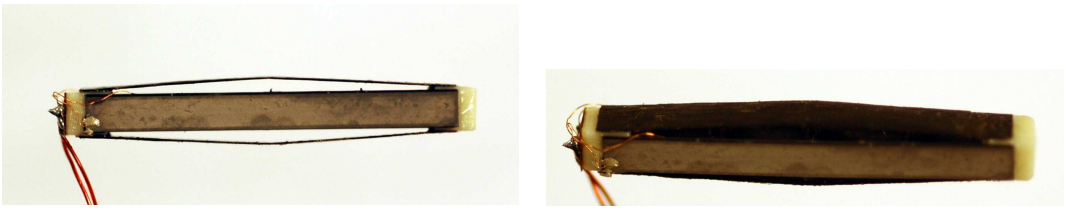

(a) (b)

Figure 5.6: Flextensional core with side beams.

a displacement of 224 μm for each side beam is predicted, for a total of 448 μm of motion. This is slightly more than the actual displacement in Table 5.2. However, the transmission model uses ideal pin joints to model the carbon fiber flexures in the side beam; therefore, some motion is expected to be lost in compression and rotation of the flexures. Also, the 18.47 μm observed from the core was unloaded; slightly less would observed when the core is loaded, also explaining less side beam deflection.

Core	Left Beam Displacement	Right Beam Displacement	Total Displacement
1	237	204	441
2	175	212	387

Table 5.2: Displacement results for 300 μm bent side beam cores.

After constructing the 300 μm bent side beam flextensional core it was noted that since the beam was so close to its singularity, flexibility in the flexures, glue used to attach the side beams to the plastic, and even hand misalignment when attaching the side beams allowed them to easily snap through their singularity. The snapped-through beam moved inward rather than outward, meaning if the wing slider crank was attached no wing motion would be observed. Considering the length of the side beam (20mm) and "prebend" distance of 300 μm, it was noted that after constructing the beams, even the mold used to shape the beams could not resolve this prebend distance accurately.

Through experimentation, it was found that a 0.5mm (or 500 μm) prebend distance was large enough that the 3D printer and molding process could accurately introduce this bias. Therefore, rather than 300 μm prebent side beams, 500 μm side beams were used. Using Eq. 5.1, 158 μm of output deflection from each beam is predicted for a total of 316 μm. Table 5.3 shows displacement data for 5 flextensional cores; the average total motion is 270 μm.

Core	Left Beam Displacement	Right Beam Displacement	Total Displacement
1	124	161	285
2	139	131	270
3	121	121	242
4	102	168	270
5	157	124	281

Table 5.3: Displacement results for 500 μm bent side beam cores.

The final design utilized 500 μm bent side beams along with a slider crank with an output link of 240 μm to compensate for the lost displacement in the flextensional stage. The DC wing displacement for each wing with these design changes is predicted at 69^o. The AC displacement would increase at resonance in the system.

5.2.2 Passive Wing Hinge

As discussed in Chapter 4, passive wing rotation was used rather than the active wing rotation of the previous design that utilized a differential. Passive wing hinge design was first discussed and analyzed by Wood [66]; that design utilized a standard SCM flexure hinge and a passive plate to attach the wing. As is stressed in the design of the hinge in that work, the rotational resonance of the system must be higher than the flapping frequency; if this is not the case, a phase lag from the aerodynamic input to the actual rotation angle would be noticed and lift forces would be drastically reduced due to poor rotational timing [12]. For the low flapping frequency of the Wood design (110 Hz), achieving high enough rotational resonance is not overly difficult.

However, the design discussed here has a target flapping frequency of up to 300 Hz. The diagram of Fig. 5.7 shows the topology of the wing rotation flexure system. The wing was attached

to the bottom carbon fiber plate; a joint stop was incorporated into the design by making the flexure short enough that the top corner of the bottom plate jammed into the bottom corner of the top plate, as shown in the diagram. The joint stop angle ϕ was set with the relation

$$\phi = \frac{\pi}{2} - \frac{L_{flex}}{t_{CF}} \tag{5.2}$$

where L_{flex} is the length of the flexure. The relation is from [66] and assumes that the thickness t_{CF} is significantly greater than t_{flex}. For an angle of attack during midstroke (while the wing is jammed) of 45^o with $t_{CF} = 40\mu m$, $L_{flex} = 31$ μm.

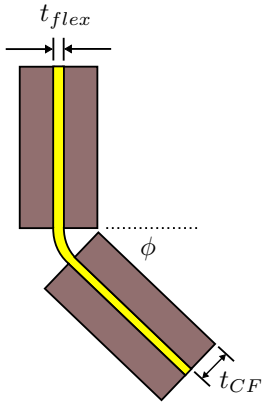

Figure 5.7: Passive rotation wing bracket diagram with characteristic dimensions.

To find the resonant frequency of the wing passive rotation system, the moment of inertia of the bottom rotational plate plus the wing about the axis of rotation was found. Using the Solidworks model shown in Fig. 5.8, the rotational inertia was found to be

$$I_{xx} = 2.16mg - mm^2 \tag{5.3}$$

With the stiffness of the rotational flexure joint given by

$$k_{rot} = \frac{EI}{L_{flex}} \tag{5.4}$$

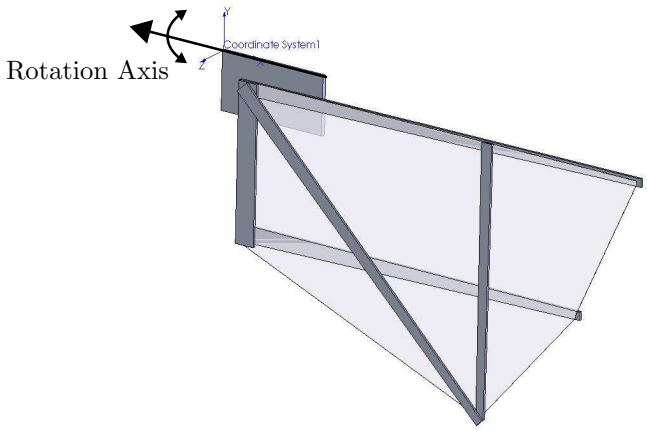

Figure 5.8: Analysis of wing bracket and wing rotational inertia.

The rotational resonance of the passive rotation system is

$$\omega_{rot} = \sqrt{\frac{k_{rot}}{I_{xx}}} \tag{5.5}$$

or

$$f_{rot} = \frac{1}{2\pi}\sqrt{\frac{Ewt^3}{12L_{flex}I_{xx}}} \tag{5.6}$$

Since I_{xx} and L_{flex} are set (the inertia by the morphology of the wing and L_{flex} by the joint stop angle) and E is set by the material choice (Kapton), the design variables here are the width of the wing bracket and its flexure thickness. Increasing the wing bracket width (thereby increasing the stiffness of the joint) also increases the rotational inertia of the system. Even though the wing bracket is near the flapping axis, since the bracket is much heavier than the wing it has a large effect on rotational inertia; the width of the wing bracket was therefore fixed at a convenient-to-construct 2mm. Rather, the thickness of the flexure is the main design variable. Normally, 7 μm Kapton flexure material is used, but as seen in Table 5.4, 12 μm Kapton must be used instead to keep the rotational resonance above the target flapping frequency.

The constructed wing bracket is shown in Fig. 5.9. The rotational flexure is difficult to see

Flexure thickness (μm)	Resonant Frequency (Hz)
7	210
12	472

Table 5.4: Wing rotational resonant frequencies for different flexure thicknesses.

because it is very small (only 31 μm long), but it is labeled for the reader to note.

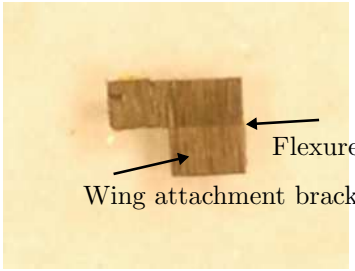

Figure 5.9: Passive rotation wing bracket.

Shown in Fig. 5.10 are snapshots of wing rotation at 275Hz. Shown in order are the wing rotated fully in one direction (5.10(a)), reaching the end of the stroke (5.10(b)), beginning to rotate in the opposite direction (5.10(c)), fully rotated in the opposite direction (5.10(d)), beginning to rotate back to the original angle of attack (5.10(e)), and finally fully rotated in the original direction in 5.10(f). The wing rotation is visually in phase with the aerodynamic input when it was flapped at 275 Hz, indicating the resonant frequency of the rotational system is sufficiently high.

5.2.3 Slider Crank Construction

The slider cranks that straddle the flextensional structure were cut out using the standard SCM process detailed in [70]. However, the laser micromachining step in this process has difficulty creating link lengths any smaller than 0.5mm (500 μm) with the standard cutting process; the resin in the composite is damaged near cuts, evaporating the resin completely in sufficiently small link sections. Therefore, to machine a 240 μm link, a new construction process for small links was needed.

Rather than machining the links directly, the composite was folded and stacked in its thickness direction to achieve small link lengths. As seen in Fig. 5.11, the slider crank was machined

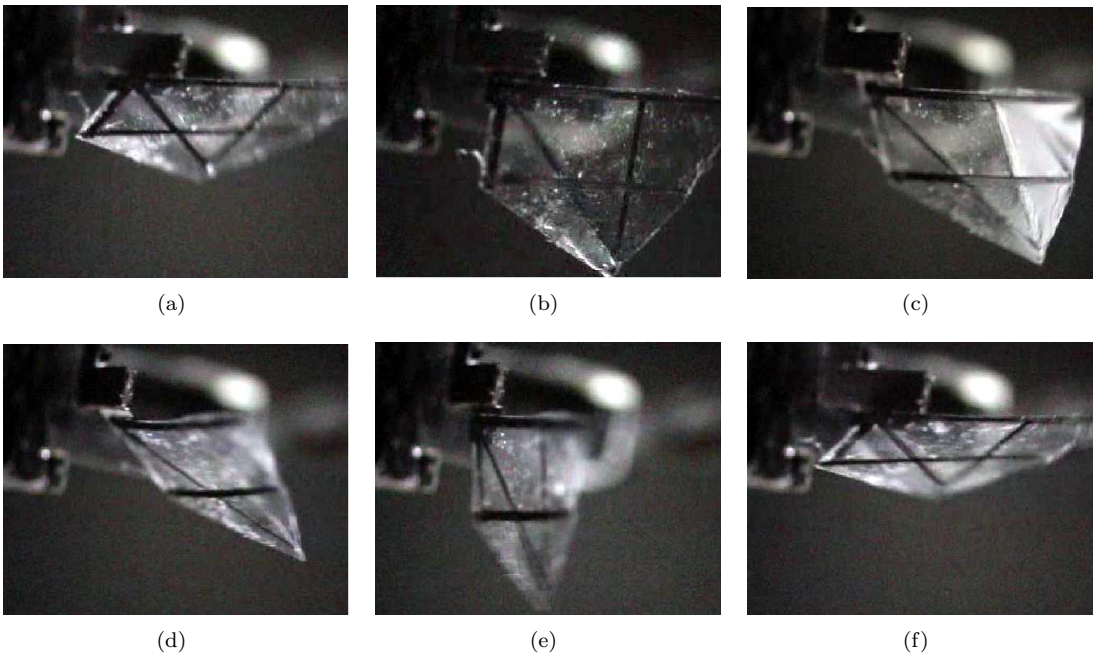

(a) (b) (c)

(d) (e) (f)

Figure 5.10: Snapshots of passive wing rotation at 275 Hz showing in phase response to wing flapping.

with the standard SCM laser process, shown flat in Fig. 5.11(a). Shown here is construction of a slider crank with a 240 μm output link, equal to 6 total thicknesses of carbon fiber (the polymer is only 7μm thick, significantly thinner than the carbon fiber). To begin stacking the output link, first shown in Fig. 5.11(b) is folding down one carbon fiber thickness onto what will become the output link. It was then attached with cyanoacrylate glue. As seen in Fig. 5.11(c) and Fig. 5.11(d), the output link was next folded on top of and then back on itself and attached.

More supporting links were folded in Fig. 5.11(e) to make the unidirectional carbon fiber give support in all loading directions. A passive rotation wing bracket was attached in Fig. 5.11(f) and more supporting planks were folded onto it for strength in Fig. 5.11(g). The completed slider crank mechanism is shown without (Fig. 5.11(h)) and with (Fig. 5.11(i)) a wing .

After assembly is complete, an accurate miniature link has been formed through the thickness of composite as is shown in Fig. 5.12(a). In the Figure, the slider crank is held in tweezers (lower left) by the side beam attachment bracket and the wing would be pointing vertically from the spar at the top of the Figure, as shown in the diagram of Fig. 5.12(b).

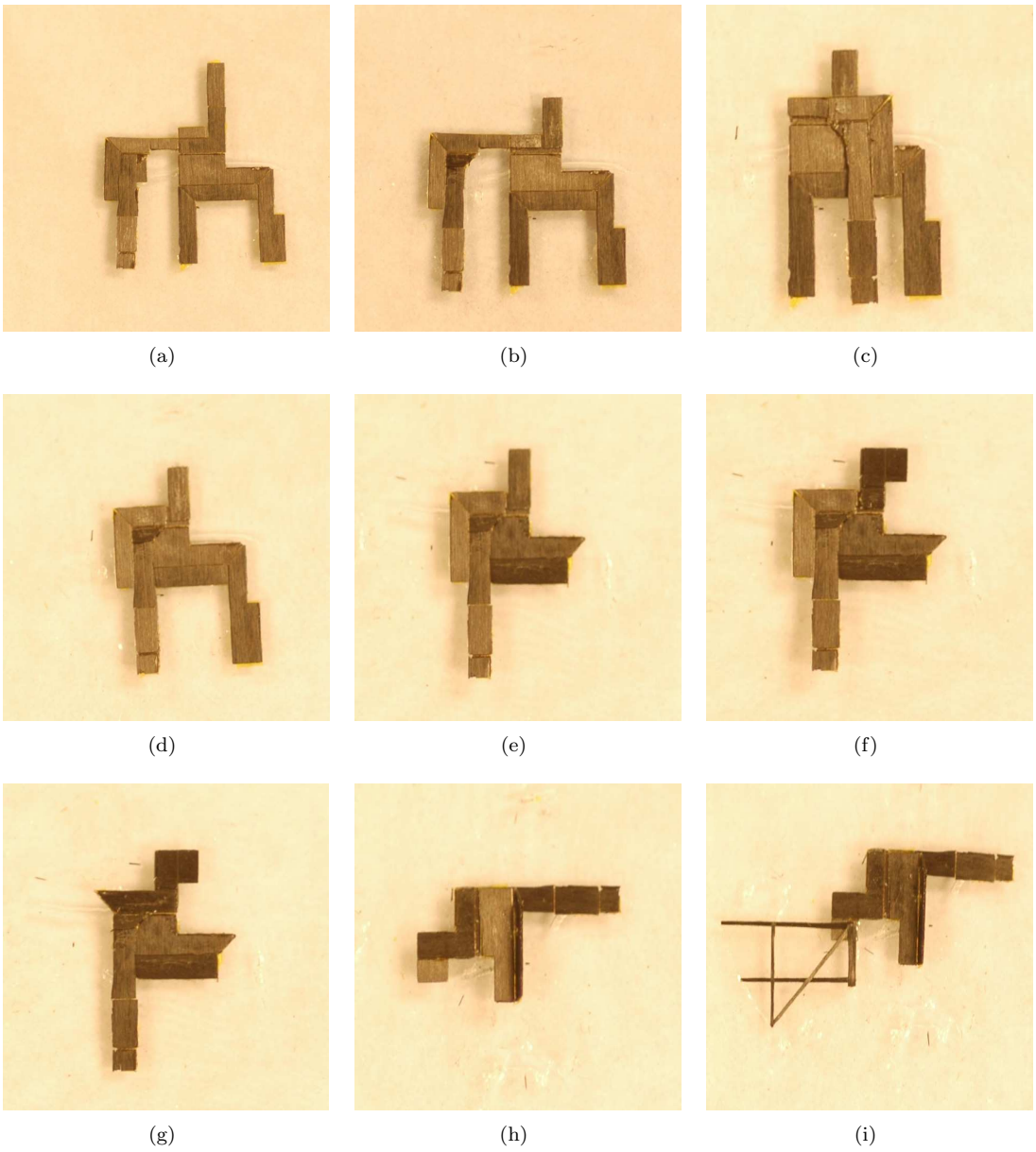

(a) (b) (c)

(d) (e) (f)

(g) (h) (i)

Figure 5.11: Construction process for slider crank mechanism.

Although this new construction procedure allows for links of smaller sizes than were previously achievable, one disadvantage is that the output link is now much heavier than simply a single laser cut link due to its multiple thicknesses and weight of the cyanoacrylate glue attaching the plates, which might reduce the resonant frequency of the structure.

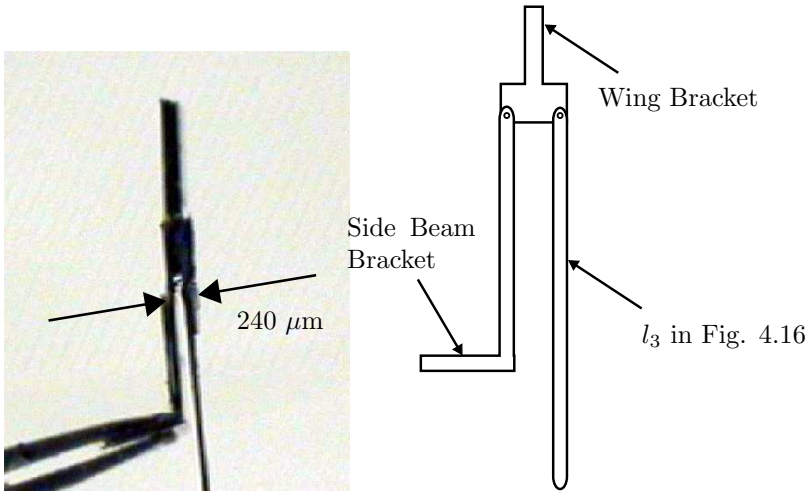

Figure 5.12: Side view of folded output link of slider crank.

5.2.4 Integrated System Testing

The integrated system was built with 500 μm bent flextensional side beams, 240 μm output link slider cranks, and wings with passive rotation joints as shown in Fig. 5.13.

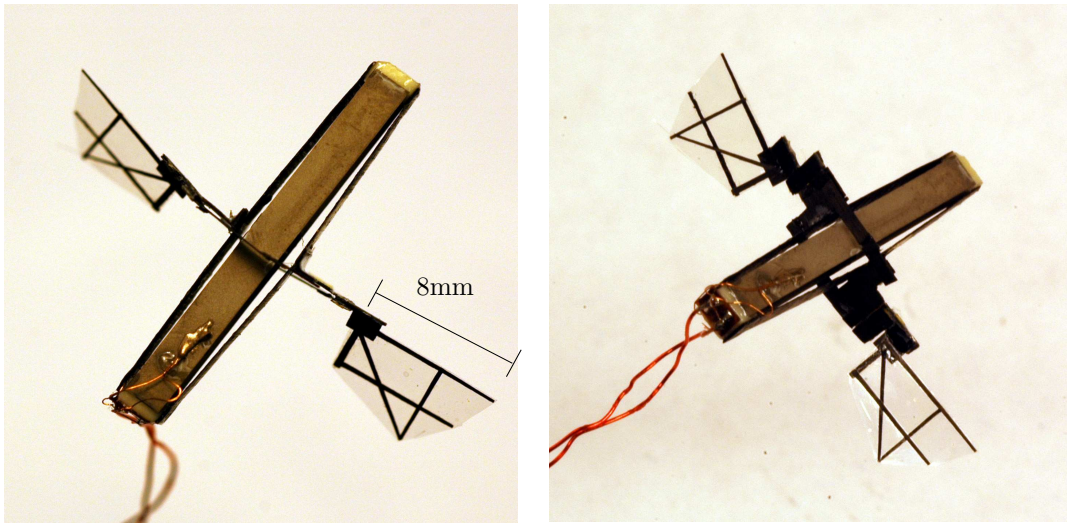

Figure 5.13: MFI Revision 1 top and back view.

The first structure of the Revision 1 variant was tested on a step by step basis as it was assembled. The loaded (no slider cranks or wings) and unloaded (with slider cranks and wings)

Element	Unloaded Deflection	Integrated System Deflection	Deflection Lost
Left Side Beam	127 μm	73 μm	43%
Right Side Beam	127 μm	84 μm	34%
PZT plates	18 μm	18 μm	0%
Left Wing Flap Angle	-	29^o	-
Right Wing Flap Angle	-	36^o	-

Table 5.5: Loaded and unloaded deflections for integrated MFI system.

displacements under static conditions are shown in Table 5.5.

One notices in Table 5.5 that the PZT plates were measurably deflecting the same amount when loaded with side beams only vs loaded with side beams and slider cranks. However, motion was lost in the side beam output when the slider cranks were attached; the total deflection has fallen 38%. This leads to the unacceptably low flapping angles (at DC) also seen in Table 5.5.

A change was made to the design to attempt to increase the flapping amplitude without significant design iteration. This structure's side beams were not 7 layers thick in the rigid sections as was outlined in Chapter 4; due to laser machining and yield problems that were later fixed, the side beams were only 3 layers thick which presumably were not stiff enough relative to the flexure stiffness. This might be one explanation for the loss in deflection from the side beams without loss in the PZT deflection.

The next structure of the Revision 1 variant was constructed with the full 7 layers of carbon fiber in the stiff elements of the side beams. Results are in Table 5.6.

Element	Unloaded Deflection	Integrated System Deflection	Deflection Lost
Left Side Beam	99 μm	66 μm	33%
Right Side Beam	161 μm	124 μm	23%
PZT plates	18 μm	18 μm	0%
Left Wing Flap Angle	-	40^o	-
Right Wing Flap Angle	-	54^o	-

Table 5.6: Loaded and unloaded deflections for integrated MFI system.

A similar observation can be made here; the PZT plates are deflecting the same amount as when unloaded but the side beams are not. However, in this case only 27 % of the motion was lost rather than 38 % in the previous structure. The DC wing deflection rose to an average of 47^o

from the previous 33.5^o.

AC test results for this structure are shown in Table 5.7. One notices here that the resonant frequency is a bit below the design goal of 200-300 Hz; however, the flapping inertia can be lowered or stiffness raised to put it in the proper range rather easily.

Parameter	Value
Unloaded Resonant Frequency	550 Hz
Wing/Slider Crank Loaded Resonant Frequency	190 Hz
Average AC Peak-Peak Flapping Motion	54^o

Table 5.7: AC test results for integrated structure, loaded and unloaded.

5.3 MFI Revision 1 Results Analysis

Considering that lift forces from a flapping wing are expected to scale with the flapping amplitude squared, the very low DC flapping angles (and hence AC flapping angles) seen here in Revision 1 of the MFI are not acceptable. However, it is suspicious that the piezoelectric plates are deflecting as predicted; low flapping amplitude is therefore not explained by failure of the PZT to produce the predicted force nor is it explained by unpredictably high stiffness in the structure. It was soon discovered that serial compliance in the structure's transmission is the culprit.

5.3.1 Serial Stiffness Measurement of Side Beams

An expression for the stiffness of the transmission mechanism attached to the axially actuating PZT plates was addressed in Section 4.6.3. This is denoted "parallel" stiffness of the transmission. Unfortunately, there is also a "serial" compliance in the structure causing low flapping amplitude. A serial stiffness or compliance is denoted so because it is in series with the motion, meaning this compliance absorbs some useful motion in the system. Diagrams explaining this terminology appear in Fig. 5.14 for a transmission element alone (5.14(a)), then a transmission with a parallel stiffness only (5.14(b)) and finally a transmission with a parallel and serial stiffness (5.14(c)).

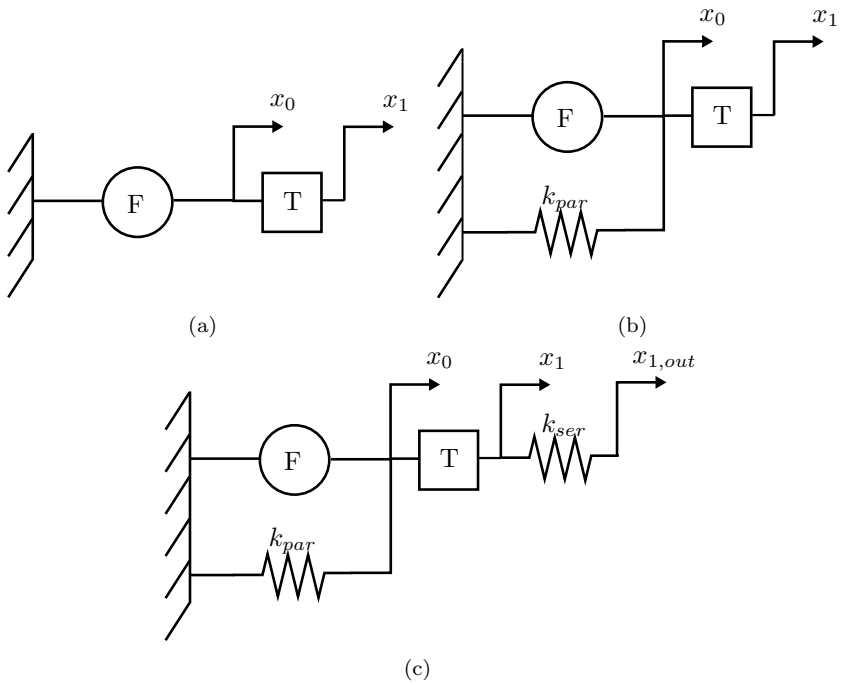

Figure 5.14: Parallel and serial transmission stiffness diagrams. a) represents a standard transmission, b) a transmission with an associated parallel stiffness, and c) a transmission with a parallel and a serial stiffness

In an ideal transmission, the serial stiffness would be infinite, or there would be zero serial compliance. If the transmission proposed here was made from ideal pin joints with infinitely stiff links, it would indeed have infinite serial stiffness. However, due to the use of flexures, lightweight materials and small dimensions, serial stiffness was not infinite and was in fact absorbing a significant amount of actuator deflection.

To quantify the serial stiffness of the lightweight side beam configuration, side beams were isolated and their input given by x_0 in Fig. 5.14 was blocked. If the input x_0 is in fact blocked, then x_1 is also blocked, leaving $x_{1,out}$ of Fig. 5.14(c) as the only moving degree of freedom. By applying known forces to the output of the side beam as in the experimental setup in Fig. 5.15, the serial stiffness can be quantified.

Four different beam "prebends" were tested with the setup. The force vs displacement relationship for these prebend distances is shown in Fig. 5.16. Though it is seen from the data that

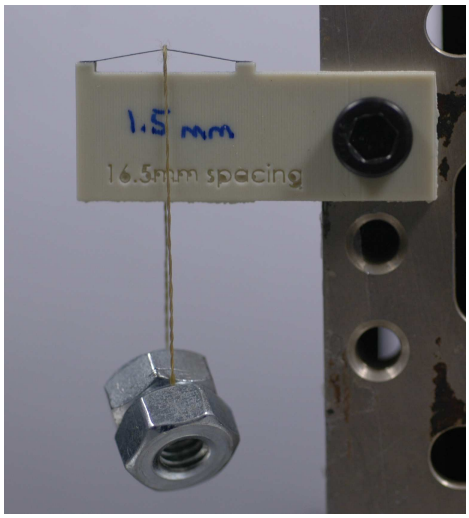

Figure 5.15: Experimental apparatus for serial stiffness measurement.

the relationship is not strictly linear, a linear approximation to the stiffness was made for ease of analysis, and the linear stiffness approximation for each beam is in Table 5.8. The nonlinearity most likely arises from buckling of both flexures and stiff links at different forces and is most noticeable with the stiffest (largest prebend distance) side beams.

Prebend Distance	Fit Serial Stiffness
0.5	2570 N/m
0.75	3977 N/m
1	8266 N/m
1.5	15191 N/m

Table 5.8: Linear fit of serial stiffness for different prebend distances.

5.3.2 Loss in Deflection due to Serial Stiffness

The model in Chapter 4 provided a complete input to output relationship including all stiffnesses and transmission ratios built into the equations. However, the model does not include any serial compliance. To represent serial compliance in the system, a simple linear model shown in Fig. 5.17 was used. This is strictly a DC model; there would be mass elements preceding $T1$ and $T2$ and following $T2$ in an AC model, which would result in several resonant modes. Here, $T1$ represents the flextensional amplifier and $T2$ represents the slider crank mechanism. The parallel

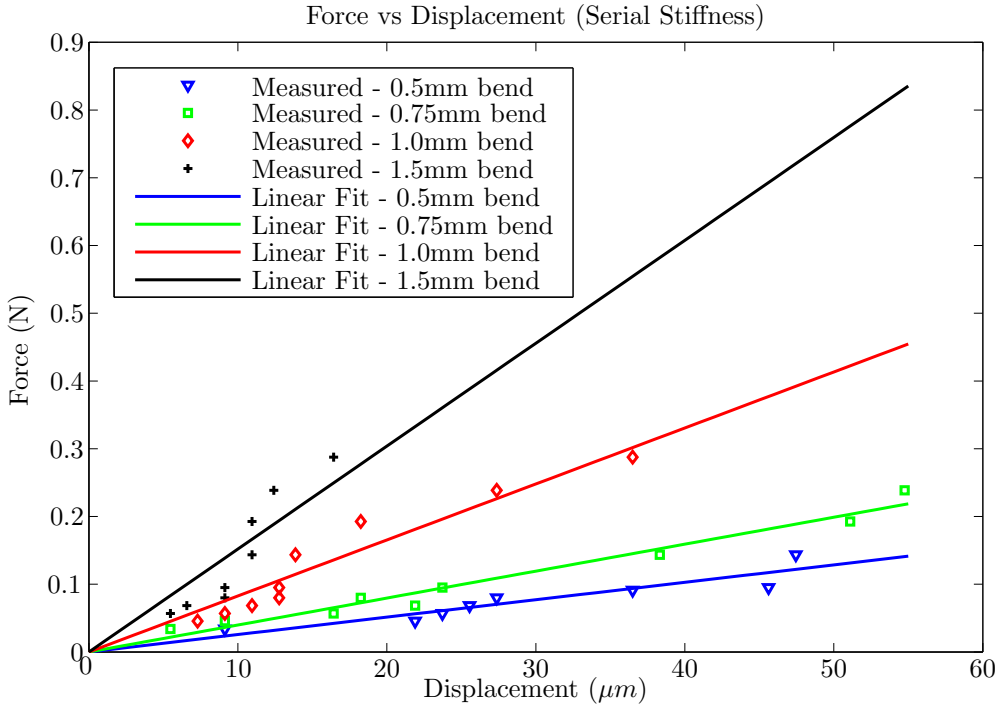

Figure 5.16: Measured serial stiffness for first transmission stage, various prebend distances

stiffnesses of these transmissions are k_{T1} and k_{T2}, respectively. Ideally, the spring k_{ser} would be infinite representing no serial compliance.

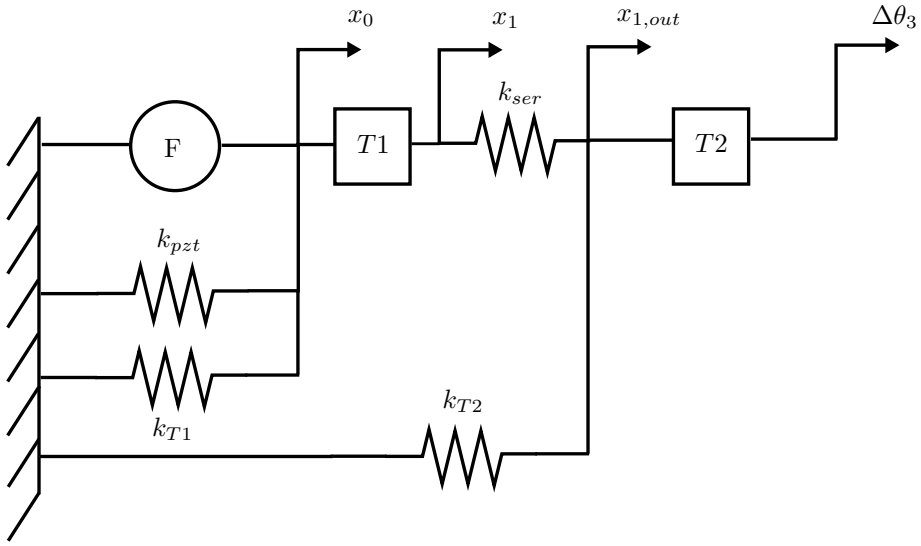

Figure 5.17: MFI Rev 1 model showing serial stiffness.

From the MFI Revision 1 structures tested here, it is known that the internal force source of the PZT plates are not force saturating; therefore the displacement x_1 in the model was simplified as a displacement source for the analysis here. If the spring k_{ser} is infinite in stiffness, then

$$T1x_0 = x_1 = x_{1,out} \tag{5.7}$$

However, the serial spring compresses if its stiffness is not infinite. Using the analysis in Chapter 4, the mean spring constant of the two slider crank mechanisms in parallel (represented by k_{T2} in the model) is equal to 928 N/m with the dimensions of Table 4.4. Knowing that the serial stiffness of a 0.5mm bent side beam is 2570N/m (Table 5.8), the relationship

$$x_{1,out} = \frac{k_{ser}}{k_{T2} + k_{ser}} x_1 \tag{5.8}$$

shows that there is a 42% loss in deflection due to the serial compliance. This is a large and unacceptable loss in the transmission that was not previously predicted in the models.

5.3.3 Modeling of Serial Stiffness and Improvement in Structure

If the serial stiffnesses of Table 5.8 are plotted against the theoretical transmission ratio (a linear approximation to the actual nonlinear transmission ratio $x_{1,out}/x_0$), the relationship between them appears to follow an inverse square law, shown in Fig. 5.18. The serial stiffness of the side beam would theoretically depend on the buckling strength of the beams and flexures (dependent on length, thickness, and width) and the initial shape of the beam. The initial shape of the beam should be very similar to the mold it is cured on; however, the beam relaxes after being released from the mold and the dimensions (like thickness) sometimes change due to stress concentrations. With these variables in doubt, an experimental stiffness relationship was used instead of a theoretical relationship.

An experimental fit of an inverse square relationship via least squares to the data in Fig.

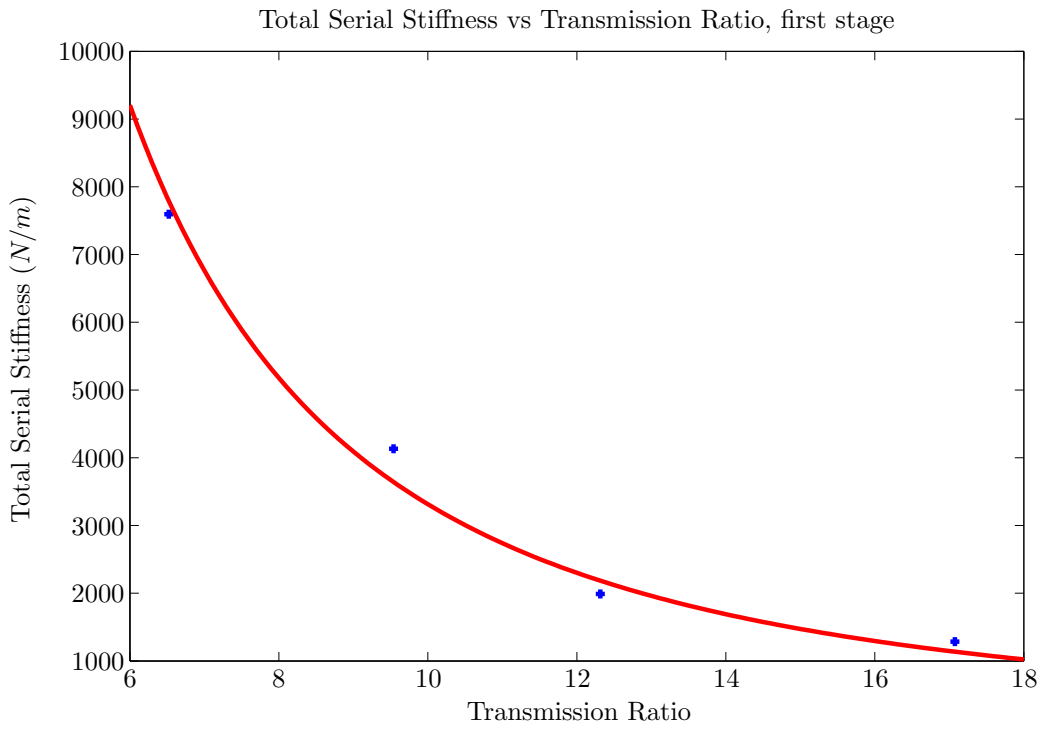

Figure 5.18: Serial stiffness to transmission ratio relationship for transmission stage 1.

5.18 yields the relationship

$$k_{ser} = 3.31 \times 10^5 T^{-2} \tag{5.9}$$

The relationship in (5.9) suggests a significant design change. If the side beam bend distance is increased, for instance making the transmission ratio of each beam drop by a factor of 2, the serial stiffness of each beam increases by a factor of 4. This means that if two of these flextensional stages were stacked in series (this is similar to the work in [61]), the total serial stiffness would be higher by a factor of 2 for the same output displacement. The mass of the structure would be comparable if the width of the PZT plates in each stage are reduced by a factor of 2. This is the main idea behind Revision 2 of the MFI design change utilizing an axial displacing piezoelectric plate.

5.4 MFI Revision 2 Design

To take advantage of serial stiffness scaling with the transmission ratio of the flextensional stage, two flextensional stages was connected in serial as shown in the model of Fig. 5.19. Each side beam is prebent at 1mm, larger than the previous 0.5mm prebend distances that suffered from serial compliance issues. One millimeter wide PZT plates are used for both cores. Considering the difficulty in attaching the point contacts of the output of the flextensional stage, a flat beam section was incorporated into the midsection of the side beams. This creates an underconstrained device; the flat section of the side beams could rotate rather than moving directly outward.

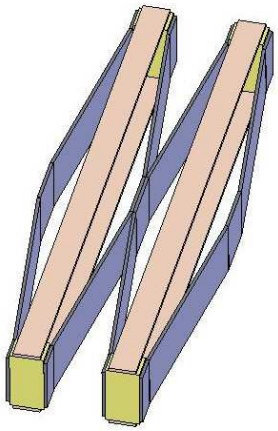

Figure 5.19: Solidworks representation of MFI Rev 2 actuator core.

A second transmission stage was added as shown in Fig. 5.20 to accomplish several goals. First, this second stage constrains the underconstrained rotational motion of the side beams. Secondly, since lack of motion amplitude has been an issue in the previous design, it provides further amplification to increase flapping amplitude. Finally, this increase in transmission ratio allows the final slider crank stage to employ a 320 μm output link rather than the previous 240 μm output link. The 240 μm output link was difficult to construct and align due to the small size of the output link; this increase in size makes construction easier.

The design now contains three amplifying stages. The first is the side beams in the double

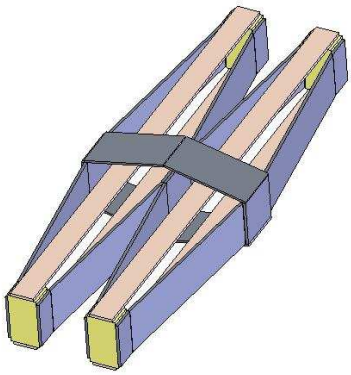

Figure 5.20: Proposed MFI Revision 2 with 2nd amplification stage.

core design (shown in Fig. 5.21(a)), once again using 40μm thick carbon fiber flexures. The second stage attaches the two outward facing links of the core and contracts toward the middle of the core, shown in Fig. 5.21(b). The flexures of the second stage are made from 13μm Kapton. Finally, a similar slider crank to the previous Revision 1 was used to turn the output of the 2nd transmission stage to a wing rotation. These two slider crank mechanisms actually pass through the middle of the actuator core, connecting the two second amplifying contracting stage. Flexures for this stage are made from 7μm Kapton. Important dimensions and predicted motions for each stage in the design are listed in Table 5.9 and Table 5.10.

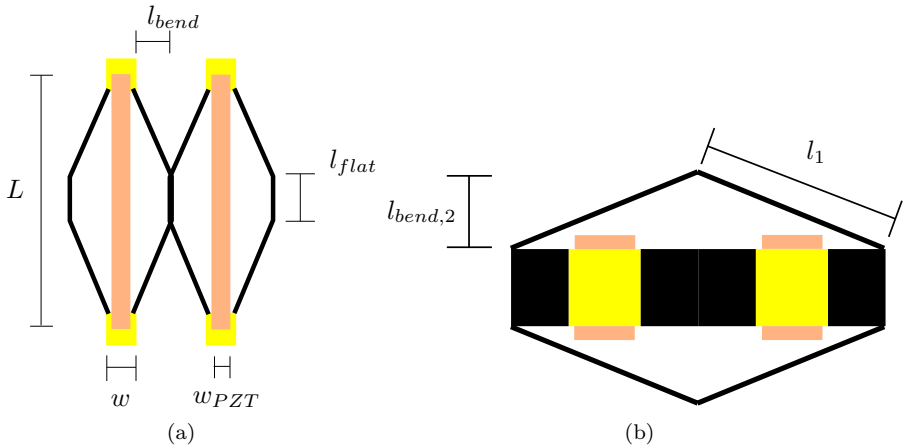

Figure 5.21: Diagrams showing dimensions of MFI revision 2.

Element	Parameter	Dimension
First Transmission Stage	l_{bend}	1mm
	w	1.25mm
	L	20mm
	w_{PZT}	1mm
Second Transmission Stage	$l_{bend,2}$	1.6mm
	l_1	4.3mm
	l_{flat}	2mm
Slider Crank	l_{output}	320μm

Table 5.9: Important design dimensions for MFI revision 2.

Element	Output Deflection
First Transmission Stage	268μm
Second Transmission Stage	834μm
Total Flapping Angle	$>120^o$

Table 5.10: Predicted output deflections for MFI revision 2.

The transmission ratio was intentionally designed to output much more motion than is necessary; 90^o of motion is the flapping angle goal. However, the predictions in Table 5.10 do not include serial compliance in any stages and therefore are overestimates. If only the serial compliance observed and measured in Revision 1 were present, then the flapping angle would meet this 90^o of flapping goal.

5.5 MFI Revision 2 Construction and Testing

The construction process for Revision 2 proceeded as follows. The side beams were folded much in the same way as Revision 1, but a flat section 2mm wide is incorporated at the output of the side beams for ease of attachment. The two cores were assembled separately and attached along their flat output beams with cyanoacrylate glue. The second transmission stage was then attached by hand and aligned with the output link of the first stage. Finally, the slider cranks were folded up as in Revision 1 (although the output link contains more layers) and were passed through the middle of the structure. Passive wing rotation joints were incorporated as in Revision 1. The assembled

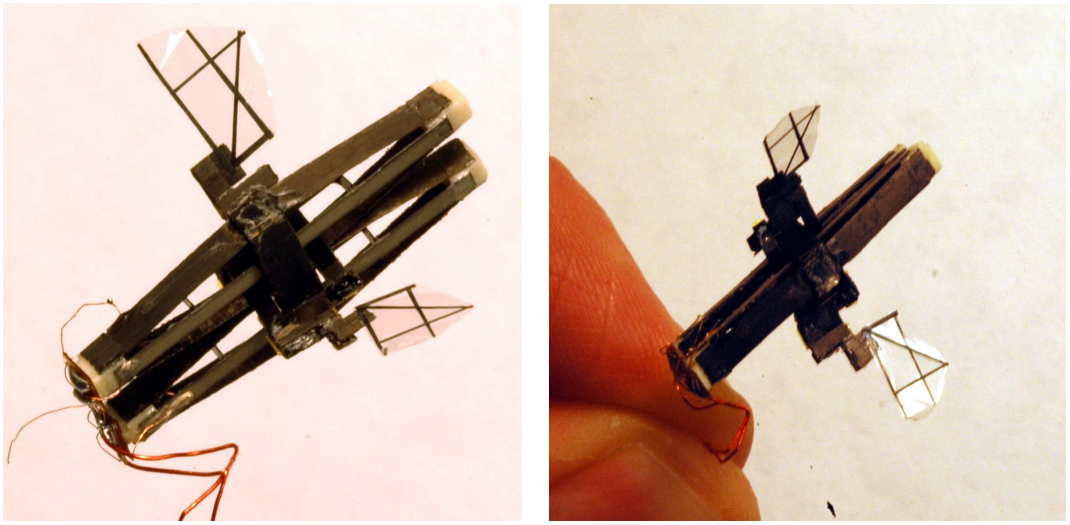

(a) (b)

Figure 5.22: MFI revision 2.

MFI Revision 2 is shown in Fig. 5.22.

DC deflection data for the design was observed at various stages of assembly and is presented in Table 5.11. Contained there is data for the double core stage alone, then the core loaded with the 2nd contraction stage, and finally with all the transmission stages. The final wing deflections are 30^o and 28^o for the left and right wing.

Element	Unloaded Deflection	Loaded with 2nd Stage	Loaded with Slider Crank
First Transmission	237μm	234μm	120μm
Second Transmission	-	854 μm	201μm

Table 5.11: DC deflections for the loaded and unloaded MFI Revision 2.

The resonant frequency of the assembled structure with wings was 225Hz. Average wing motion at this frequency and 250V peak voltage drive was 42^o total flap angle. This motion is shown in Fig. 5.23 under a strobe light. Some wing rotation can be observed in the Figure but the wing does not properly rotate fully due to the low flap angle.

Even with low flapping amplitude and minimal wing rotation, a simple lift test was performed by holding the structure above a precision balance (Adam Equipment AAA-250L, see Fig. 5.24). The downwash from the wings presses down on the scale to make a lower bound on the lift

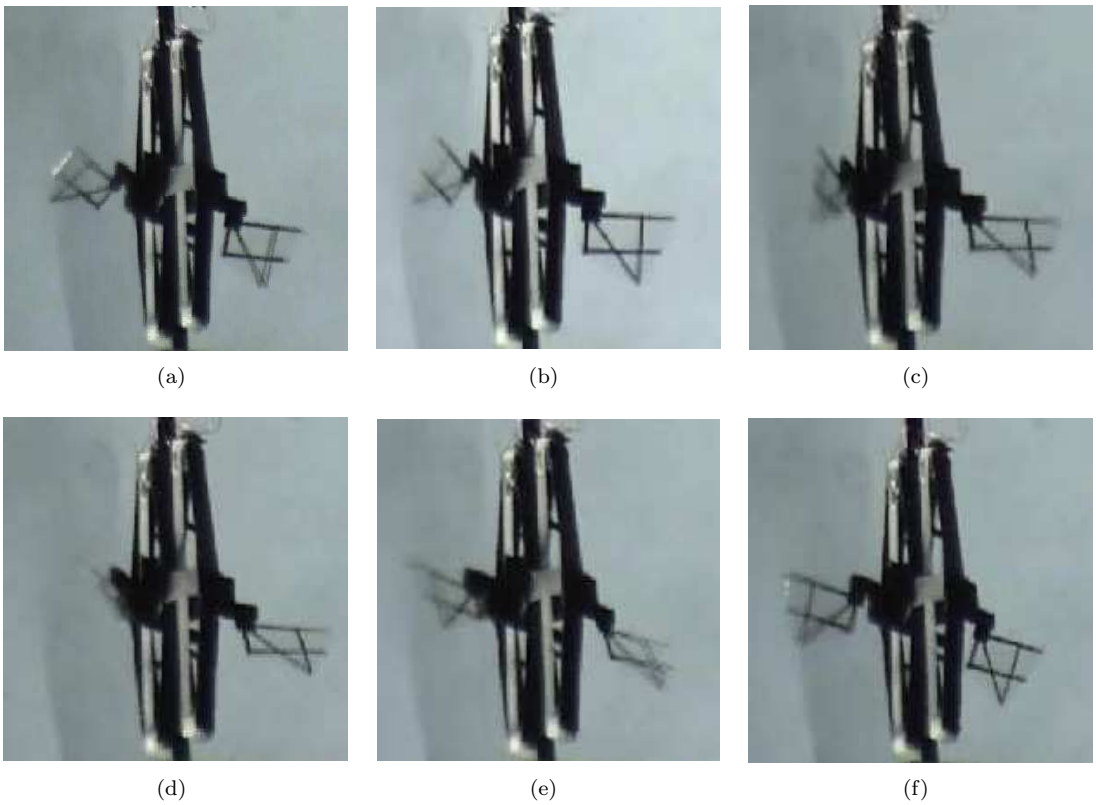

Figure 5.23: Strobed wing stroke of MFI rev 2 at 275 Hz.

produced. The total lift produced is technically larger than the measured value on the scale; some of the downwash was being damped out by surrounding air or directed more outward, thereby missing the scale plate. The largest lift measurement from the structure was 37.5mg, short of the structure's total weight of 150mg.

5.6 MFI Revision 2 Results and Analysis

MFI Revision 2 suffers from serial compliance issues similar to those in MFI Revision 1. However, the serial compliance here was not only from the side beams; in this case, there are two other major twisting degrees of freedom that must be addressed. Both twisting compliances are associated with the attachment point between the two independent actuator cores and the associated side beams' abilities to resist bending moments.

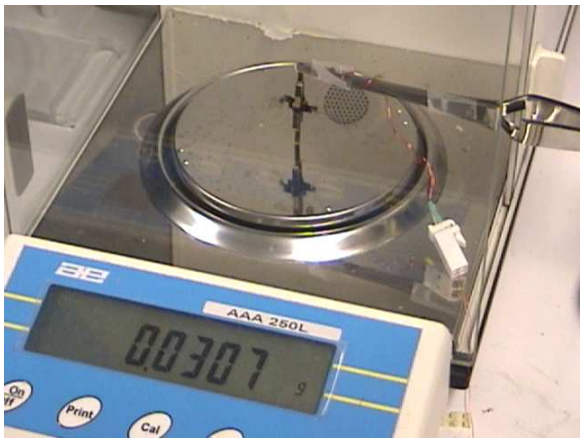

Figure 5.24: Lift test setup of MFI revision 2.

Fig. 5.25(a) shows a compliance associated with the plastic end caps of the cores on one side coming closer together while the end caps on the other side become farther apart. This, in combination with the compliance shown in Fig. 5.25(b) associated with moments at the end caps, are two internal modes of motion that result in severely reduced wing motion.

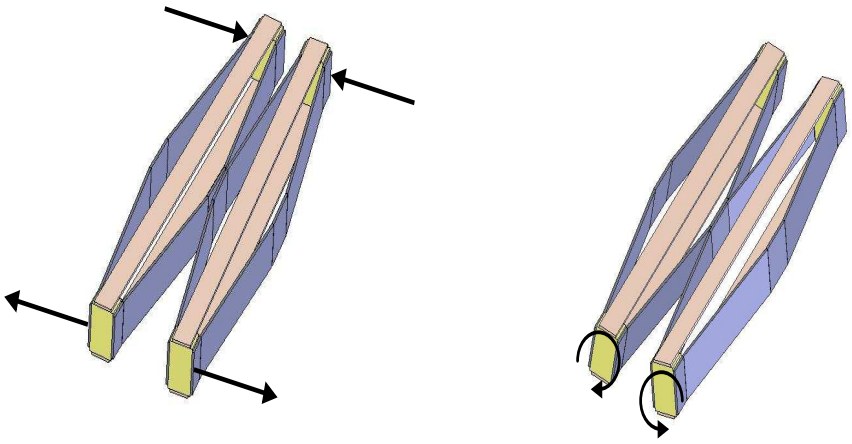

(a) (b)

Figure 5.25: Two noticeable undesirable compliances in MFI Revision 2

Even with the compliances that result in a very low wing flapping angle of 42^o at 225 Hz, 37.5mg of lift was measured from the structure, equal to 25% of the structure's total weight. Though

lift is expected to increase as amplitude squared, it in fact increases faster than this as the low flap amplitude here most likely does not properly allow the delayed stall vortex on the wing to properly establish. Also, wing rotation was minimal, so if the flap amplitude is increased the aerodynamic input for rotation would be larger, resulting in a more optimal angle of attack (45^o).

Chapter 6

Conclusion

In this work, a power density framework has been developed for the design of mobile millirobots, with target power density coming from animals in nature. The power output of the piezoelectric actuators used on the MFI was then directly measured for the first time. Using this data and an observation regarding the strain profile on the PZT layers of a bending actuator, the MFI platform was completely redesigned using an axially straining PZT plate. An axial method of actuation for a piezoelectric plate is predicted to have a power density >1000W/kg at 275Hz compared to a measured power density 467 W/kg at 275Hz for a bending actuator due to its uniform strain profile through the thickness of the piezoelectric material. Two revisions of the axial MFI design were built and tested. Although takeoff or lift force equal to the weight of the structure has not been achieved, the design offers the promise of increasing the power input to the wing. Rather than suffering from actuators not capable of proper power output, the design suffers from an inefficient transmission mechanism which can continue to be engineered.

6.1 Suggested Future Work

The main advantage of using an axial mode piezoelectric plate is the increase in power output to the wing; however, using this mode requires a transmission mechanism that tends to have high serial compliance which then absorbs the increased power to various degrees. Here two different future routes are suggested for the MFI platform, both based on the work in this thesis. The first option suggests improvements to the design presented in this thesis. The second option is an improvement to the Wood design that has already taken off to improve its flapping frequency and power output to the wing to achieve even greater thrust to weight ratio.

6.1.1 Changes to Axial Mode MFI

Although serial compliance can be predicted in the side beams of the MFI design, when two cores were connected in series in Revision 2 of the redesigned MFI, other compliances began reducing flapping amplitude. Using Sarrus linkages across the plastic end caps of the core will reduce twisting (described in Section 5.6) and improve flapping amplitude. This addition will also make the resonant frequency of the system higher for increased lift.

The design can also benefit from improved attachment between the two middle side beams; currently they are glued along a 2mm x 2mm plank. Considering the structure's overall length of 20mm, this small attachment plank could benefit from either being larger or should be incorporated into the curing process for a firmer attachment. Other improvements can also be made to the side beams themselves, including the adoption of smaller flexures (to increase buckling strength), straight rather than curved flexures (when relaxed), or thicker link sections.

6.1.2 Suggested Changes to Wood Design

Rather than adopting the straight axial design proposed here, another route could be to adopt several changes to the already successful Wood design that are suggested by the research in

this thesis for a future flapping vehicle.

To address the loss in energy output due to the strain profile of a bending actuator, the thickness of the elastic layer can be increased. Using the relation in Eq. (4.10), the energy output ratio between the bending actuator and an axially straining PZT plate is plotted in Fig. 6.1. As has been previously discussed, with only a 40 μm thick elastic layer (one layer of carbon fiber) the axial PZT plate can output 2.6x more energy than a bending actuator; however, if the elastic layer is infinitely thick, the strain profile in the PZT layer would be uniform and this ratio would be 1. The Figure shows that increasing the thickness of the elastic layer by only a few layers of carbon fiber can quickly make the bending actuator more competitive in terms of energy output of the active PZT layer. Increasing the thickness of the elastic layer up to several hundred microns is not realistic in that the energy density of the actuator due to the weight of the elastic layer would quickly fall.

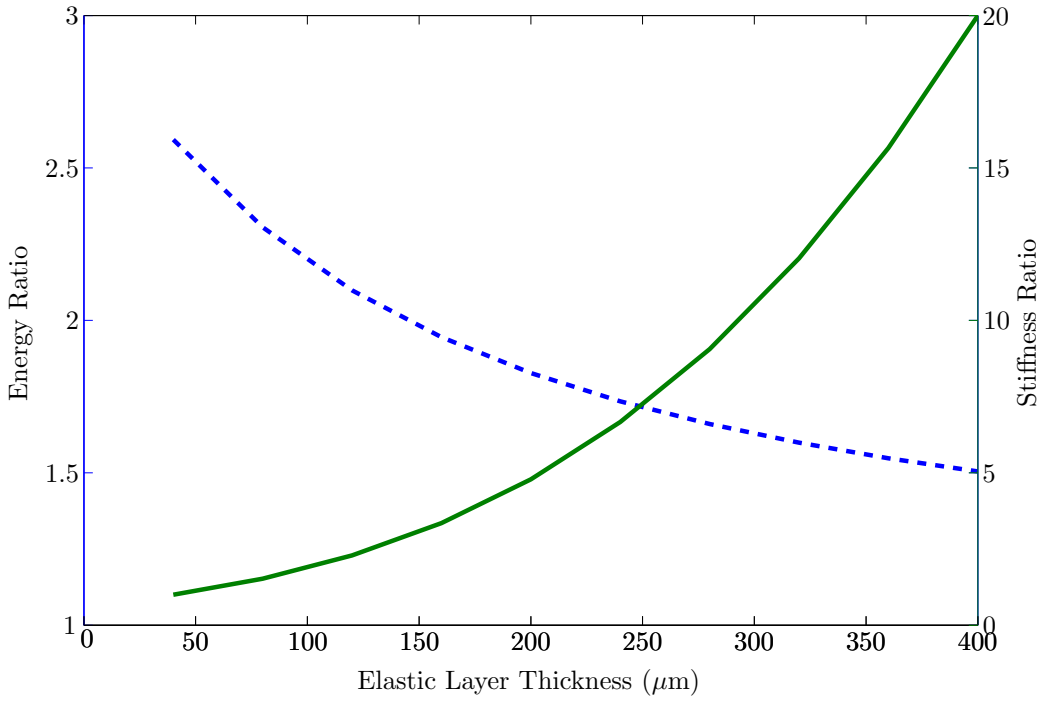

Figure 6.1: Actuator performance (stiffness and energy output ratio) as the carbon fiber elastic layer thickness varies.

Increasing the elastic layer thickness also increases the stiffness of the actuator. Fig. 6.1

also shows the predicted increase in stiffness (divided by the stiffness of the 1 layer carbon fiber actuator, so plotted is a stiffness ratio) as a function of the elastic layer thickness. As elastic layer thickness increases, the DC motion of the actuator goes down, but the resonant frequency goes up. At the resonant frequency, the overall AC motion of the actuator will not suffer except for the increase in damping of the wing due to the increased drive frequency.

Designing a flapping mechanism using a large bending actuator like Robert Wood's design at Harvard with a stiffer cantilever actuator is therefore viable but would need to be carefully tuned. In fact, redesigning Wood's 60mg flapping mechanism using a stiffer actuator would yield a vehicle that does not suffer from the serial compliance issues of the straight axial design proposed here while still benefiting from a more uniform strain profile on the PZT. It would also have a beneficially higher resonant flapping frequency while only having a nominal loss in flapping amplitude, which itself reduces plastic strain in the output flexures giving the structure a longer lifetime.

6.2 Final Remarks

Considering the many years of research in producing the MFI design of 2006 utilizing bending actuators, fourbars, and a differential, the 1.5 years of development for the axially straining MFI can be seen as just the groundwork in developing the next design. It will hopefully lead to vehicle thrust to weight ratios from 2 to 5 that custom power and control electronics and a battery can be integrated with to yield an autonomous flapping flying vehicle.

Appendix A

Improvements in Manufacturing Technology

As described in the Introduction, high performance compliant mechanisms were chosen for transmissive elements of the MFI. In fact, the "origami" process of machining flat parts and folding them into three dimensional stiff or flexible elements can be used for not only transmissive elements but also for various other structural purposes.

Lightweight compliant mechanism construction for the MFI project has evolved over several years. Early construction processes involved scoring and folding lightweight stainless steel, using folded triangular steel as rigid links and scored flat steel as a flexural material [74]. Eventually, high performance composite materials (such as unidirectional carbon fiber or fiberglass) became utilized along with polyester flexures as has been described in detail in [70] and [69] to yield compliant mechanisms that are much lighter, easier to assemble, and which have longer cycle life. Along with detailed analysis and design guidelines in [3], the process has yielded a versatile and successful fabrication solution for microrobots.

The compliant mechanism construction and design process has been named Smart Com-

posite Manufacturing (SCM) [70]). The process itself has been tuned for several years; its current form is described briefly here to provide context for recent improvements.

A.1 Previous Manufacturing Process

The current composite linkage assembly process proceeds as follows - the reader is stepped through the creation of a simple 3 link, two flexure mechanism.

Each half of a component (in the thickness direction) is manufactured separately. To create one side of the component, the composite material (for the MFI, UHM M60J unidirectional carbon fiber from YLA Inc.) is attached to Gelpak 8 (a sticky material that holds the sample down during machining) and micromachined under a frequency doubled Nd:YAG laser (wavelength 532nm) using a square spot size of 125 microns (by means of a 20x focusing lens). The part after laser micromachining appears in Fig. A.1(a). The surrounding carbon fiber waste is removed manually with tweezers under a microscope (Fig. A.1(b)), and a laser micromachined layer of polyester film (12 micron Mylar) is aligned manually to the composite (Fig. A.1(c)). This assembly is then baked in a vacuum oven, pinching it between two glass slides by either applying weights or using a spring hand clamp to apply pressure (Fig. A.1(d)). Once removed, the carbon fiber/polyester part is peeled from the underlying Gelpak and placed upon another micromachined composite side (Fig. A.1(e)), again manually aligned. This assembly is again clamped and baked in a vacuum oven the same as in Fig. A.1(d); once peeled from the Gelpak, the part is finished as shown in Fig. A.1(f).

Several problems still exist with the process even though it is vastly superior to previous steel processes. First, part yield is an issue. The manual alignment in step A.1(c) is quite critical; many parts are lost due to small misalignments in this step. In addition, clamping the pieces between 2 glass slides and applying pressure via weights or a hand clamp does not produce uniform pressure; some parts have very little pressure and do not achieve adequate bonding between the polymer layer and the carbon fiber, while others are under a pressure concentration. This results in peeling of the

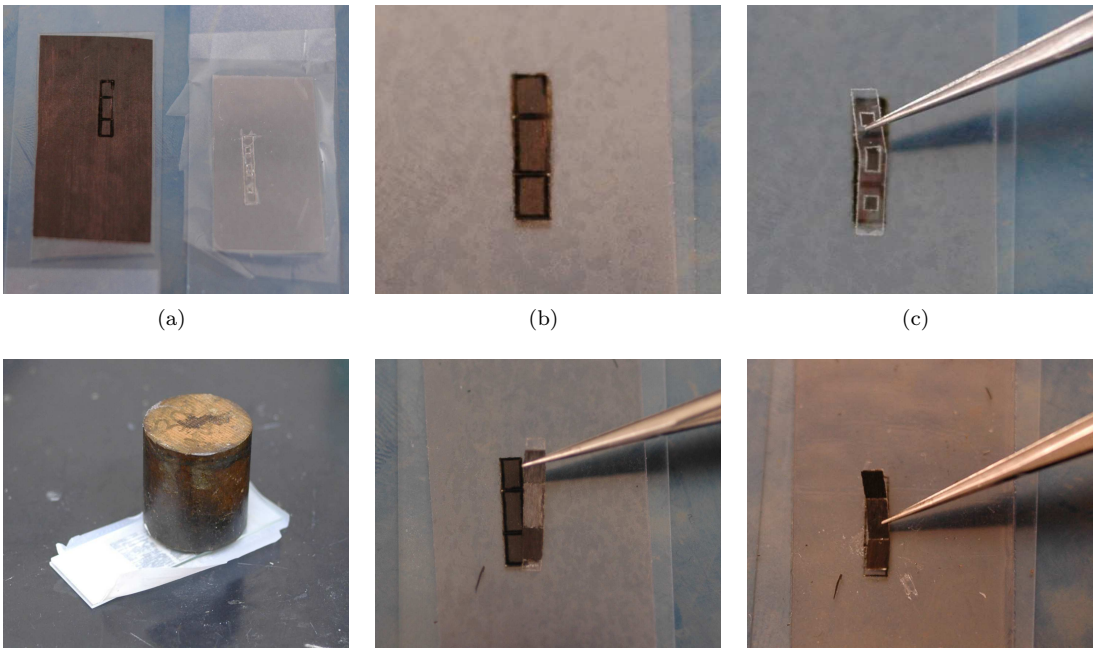

(a) (b) (c)

(d) (e) (f)

Figure A.1: Previous composite manufacturing process.

flexural joints; however, since polyester bonds very well to carbon fiber, not many parts are lost due to peeling.

Utilizing polyester as a flexure material, however, does result in another undesirable characteristic of the current process. The recommended peak cure temperature of the UHM M60J with RS3C Resin is 350^oF (or 176^oC); however, when the Mylar film is exposed to air at this temperature, it becomes "cloudy" (presumably oxidizing) and most importantly more brittle. This effect was qualitatively observed to become worse with rising bake temperature. One solution would be to cool the part down to room temperature in the vacuum oven; however, this is not practical because the oven takes many hours to cool. Rather, a compromise was reached during curing; the whole part was cured at 140^oC, meaning that the carbon fiber is not cured ideally but the flexures have not become too brittle. This could possibly result in higher damping of the structure from the uncured resin in the carbon fiber and reduced lifetime from the somewhat brittle polyester.

These observations give rise to several process improvements that improve both component

quality and yield. First, if a polymer with better temperature stability than polyester is utilized, the carbon fiber can be cured without damage to the film. Polyimide film (Kapton 30HN by DuPont) was chosen as the new polymer flexure layer, and in fact the high lift MFI structure in [55] was produced using Kapton flexures. However, part yield utilizing Kapton with the current process is well below 50% due to the inertness of the polyimide; clamping and curing in the vacuum oven is not adequate to prevent flexure peeling except where the clamping mechanism has produced pressure concentrations. In fact, flexure peeling is even more an issue because of the damage the laser introduces to the resin in the carbon fiber near flexures; since much resin is evaporated, bonding in these areas is not ideal considering that clamping does not apply enough pressure to encourage the resin to reflow into the damaged areas.

Several process improvements are required to improve part yield and to take full advantage of polyimide as a flexure material. The improvements to the past process offered herein are three fold:

1. Improvement in damage to CF when laser cut to maintain significant resin concentration near flexures.
2. An automated folding process for higher part yield and less manual alignment.
3. Vacuum bagging for higher and more uniform pressure and therefore improved bonding of Kapton to CF.

A.2 Improved laser cutting process

As mentioned earlier, using a 20x lens, the current process cuts with a wavelength of 532nm with a 125 micron spot size. However, the damage to the carbon fiber remaining on the sample is significant; a “shadow” exists where resin has been evaporated from the carbon fiber matrix as shown in Fig. A.2(a). This is one reason that peeling from the flexures is observed; there is very little resin after the cutting process near the flexures. Some flow of the resin occurs during baking.

However, RS-3C is a low-flow resin, which is good for preventing resin from flowing into the flexure, but means that good flow of the resin into the evaporated region was not being achieved.

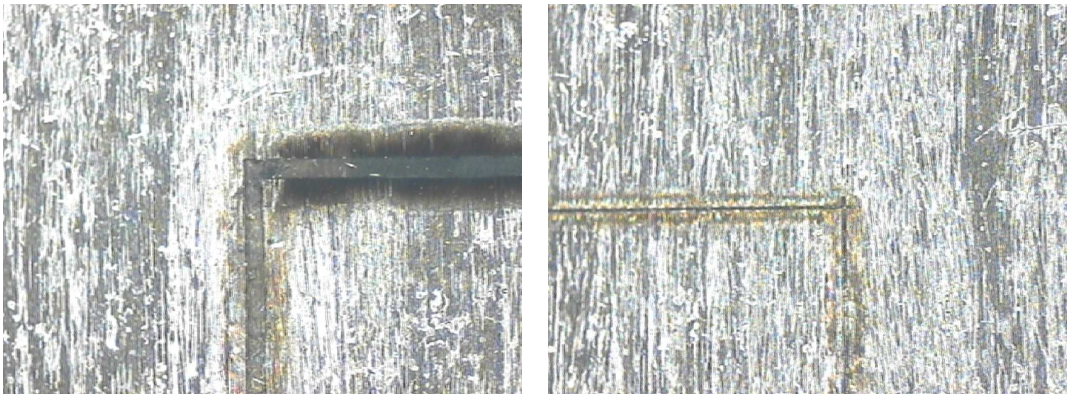

(a) (b)

Figure A.2: Laser damage to carbon fiber resin for (a) a 125 μm cutting window and (b) a 17μm cutting window.

To prevent resin curing and evaporation, the laser spot size can simply be reduce with a window available in the laser hardware. This reduces the overall power into the sample, but does not reduce the power density. For reference, the relationship between the "markersize" variable within the Microlaze software (M) was measured while measuring carefully the actual cut width (W) in the carbon fiber under a microscope (Fig. A.3). The relationship of Eq. A.1 produced by a linear fit of the data of Fig. A.3 relates the markersize value and the cut width W in μm.

$$M = \frac{W + 7.86}{1.25} \tag{A.1}$$

Various cut widths were used to find a point at which the carbon fiber was properly vaporized while damage to the surrounding resin was minimal. As can be seen in Fig. A.2(b), it was found that a 17μm by 125μm spot size for vertical cuts and 125μm by 17μm spot size for horizontal cuts significantly reduces damage to the surrounding matrix while still cutting through the material. The smaller dimension in each of these correspond to a markersize value M of 20. It is also interesting to note that the cut step size, that is the distance the laser advances for each stage step, must be

shorter for cross-fiber cuts because the laser heat is only transmitted appreciably along the fiber direction and not appreciably against the fiber direction.

	Markersize X	Markersize Y	Cut Step Size (mm)
Vertical Outline Cut	20	100	0.12
Horizontal Outline cut	100	20	0.06
Vertical Flexure Cut	Variable	100	0.06
Horizontal Flexure cut	100	Variable	0.04

Table A.1: Recommended laser profile settings for carbon fiber cutting.

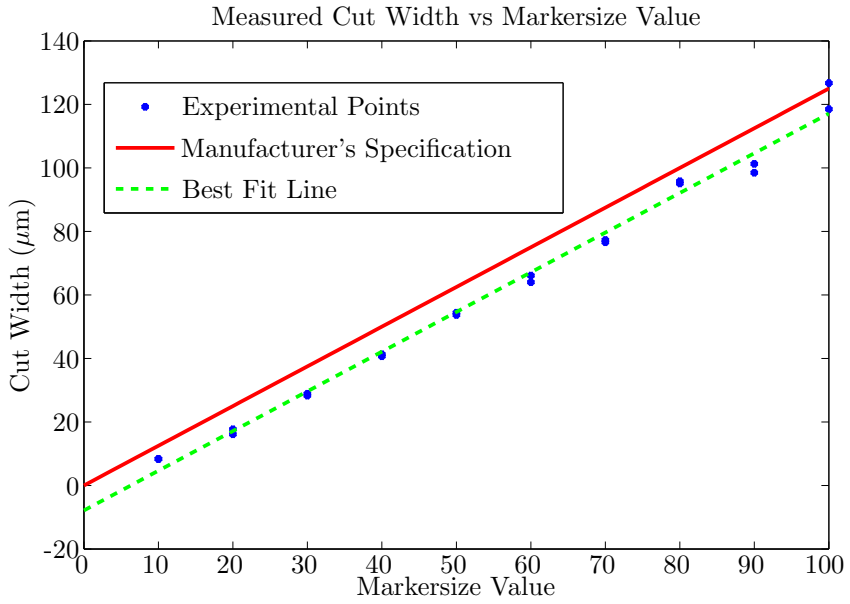

Figure A.3: Experimental, fit, and theoretical relationship between laser markersize variable and actual cut width on carbon fiber (20x lens)

When a wider flexure cut is needed, rather than cutting with a full open window, 2 parallel smaller window size cuts are used. Qualitatively, a window size of 65 μm or smaller keeps damage to the surrounding matrix acceptably small for bonding/peeling purposes. When just an outline cut is needed, the window size is kept rectangular with the smaller direction of 17μm against the cut direction. The laser power has been increased to maximum power for all cuts mentioned. An additional benefit of this method is that the damage to the Gelpak 8 under the composite is minimal, which helps to keep ash from bonding with the flexure layer during curing as shown in Fig. A.4.

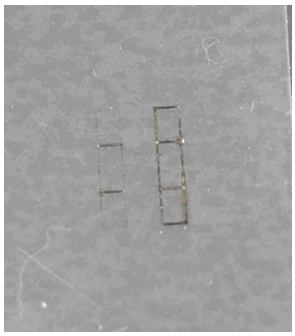

Figure A.4: Damage from laser cutting with large window size (right) compared with small window size (left, difficult to even see)

A.3 Automated Folding of parts

Even though many successful structures have been built by the process outlined in Section A.1, errors due to misalignment in step (d) can force part yield below 50 % even for skilled builders. A highly accurate and repeatable alignment process is needed. Undergraduate researcher Quan Gan developed such a process and published it only internally to the lab. The process was fine tuned by myself and is now regular practice in the manufacturing procedure. Today, virtually no parts are lost due to misalignment.

The process begins in Fig. A.5(a) where, rather than simply cutting one layer of carbon fiber alone, two separate layers of carbon fiber are laid out separated by steel shim with a precisely cut score line running vertically down it. This score line later serves as a fold line for alignment. Both sides of the carbon fiber are placed on Gelpak X8 on the two sides of the steel, which itself is stuck to the Gelpak. One side, however, is Gelpak with adhesive backing while the other is non adhesive backing; this is important so that one of the glass slides is easily separable from the rest of the assembly. The non adhesive backed Gelpak X8 is taped with standard scotch tape to the glass slide; this is removed later.

The entire assembly is placed under the micromachining laser with the angle between the stainless steel score line and the laser stage frame of reference noted. Both the left and right side of the carbon fiber are cut parallel to the fold line, with software compensating for misalignment

between the score line and the laser stage. The polymer layer is cut and aligned identically to the old method since aligning the polymer layer is not critical or difficult. The two halves of the carbon fiber cut and the polymer layer (in this case Kapton film 30HN) aligned on one side are shown in Fig. A.5(b).

The two halves of the carbon fiber on glass are now folded together along the precision scored line in the steel shown in Fig. A.5(c) - they automatically align since they were cut aligned to the fold line originally. The glass slide that was taped to the non adhesive Gelpak x8 is next removed (Fig. A.5(d)) and holes are poked through the top layer of Gelpak to allow the epoxy resin in the carbon fiber to outgas. The single remaining glass slide with the part and two layers of Gelpak is then baked; a cross section of the layup is shown in Fig. A.6.

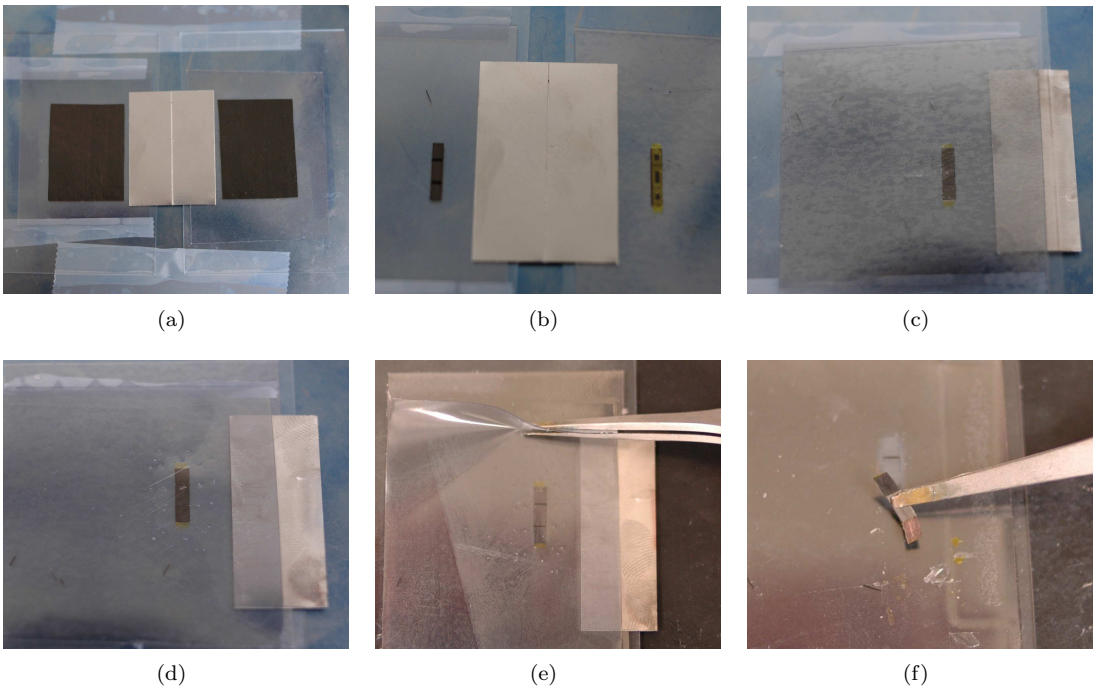

Figure A.5: Improved composite manufacturing process.

Once baked, the top layer of Gelpak is peeled away using a sharp peel angle (Fig. A.5(e)) and the part is removed as before from the bottom layer of Gelpak (Fig. A.5(f)). The idea of automatic folding is key to increasing part yield in the SCM process in that virtually no parts are

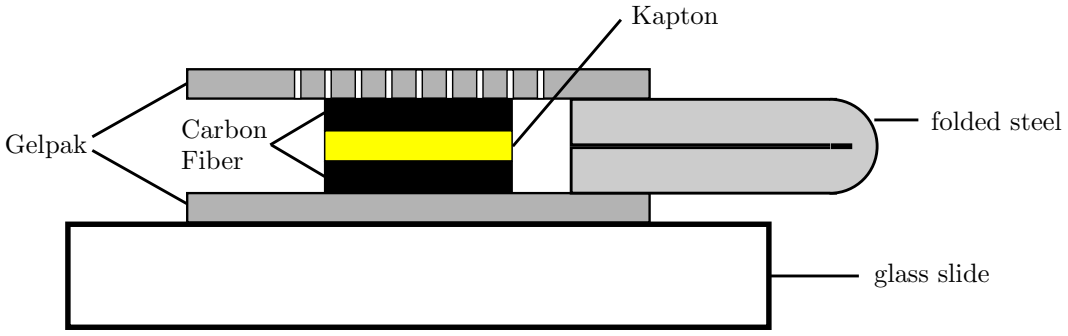

Figure A.6: Cross section of carbon fiber/Gelpak layup produced from the automated folding process. The top Gelpak layer is shown with holes for the composite to vent.

lost due to layer misalignment.

A.4 Vacuum Bagging for Improved Bonding

Finally, and possibly most importantly, is to address the method of applying pressure to the part during curing. When polyester flexures are to be used, this is not critical; polyester bonds very well to the carbon fiber resin and no peeling is observed. However, as was detailed earlier, it is difficult to cure the carbon fiber properly considering the high temperature embrittlement of the polyester. Therefore, Kapton (polyimide) film was chosen for the flexure layer of the parts. However, Kapton is quite inert and does not bond well to the carbon fiber using previous baking methods. Parts cured simply with a sandwich of glass slides and weights on top did not achieve adequate bonding of the carbon fiber to the Kapton; the carbon fiber was easily peeled away from the Kapton, as is illustrated by Fig. A.7.

A more uniform pressuring method is necessary, not to mention the need to follow the manufacturer's recommended temperature cure profile for the carbon fiber to achieve adequate bonding. The solution is to employ vacuum bagging rather than simply applying weight to the sample. A custom vacuum bagging aluminum plate was constructed (shown throughout Fig. A.8).

The aluminum plate is very simple; it has a central hole which connects to the outside edge of the plate where it is threaded and attached to a vacuum ball valve (McMaster-Carr, item

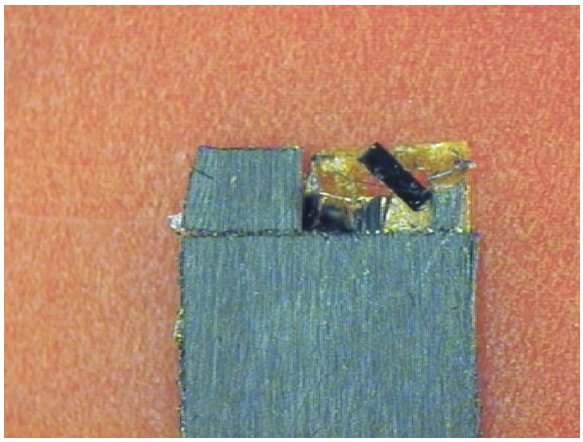

Figure A.7: Carbon fiber peeling away from Kapton near a flexure when vacuum bagging is not employed.

4847K43). After going through the laser micromachining and folding stages (Sections A.2 and A.3), the glass base plate of the part is placed on the aluminum plate in Fig. A.8(a) (also shown is molding of a three dimensional shape of carbon fiber over a high temperature rubber mold). High temperature sealant tape (AT-200Y from fiberglasssupply.com) is placed on the aluminum plate around the slide and around the central hole in the plate in Fig. A.8(b). If the sample is not a "sandwich" type layup with Gelpak on top and bottom, a piece of perforated teflon film is used as a release layer directly on top of the sample. A breather cloth (paper towel is sufficient) is laid on top of the layup within the borders of the sealant tape to allow air to flow laterally along the plate when vacuum is applied (Fig. A.8(c). Stretchlon 800 film (fiberglasssupply.com) is then laid on top of the sealant tape and pressed down in Fig. A.8(d). Vacuum is applied to the sample and the tape is pressed down further to guarantee a good seal; the valve is then closed, shown in Fig. A.8(e). A cross section diagram of the vacuum bagged layup is shown in Fig. A.9, using a folded carbon fiber part as an example.

The entire aluminum plate is then placed in a programmable oven and baked. The oven is programmed according to the resin system manufacturer's directions; in this case, the RS-3C resin from YLA, Inc is used in the carbon fiber. The recommended cure profile is shown in Fig. A.10.

The vacuum and flexibility of the Stretchlon film creates a very uniform pressure on the

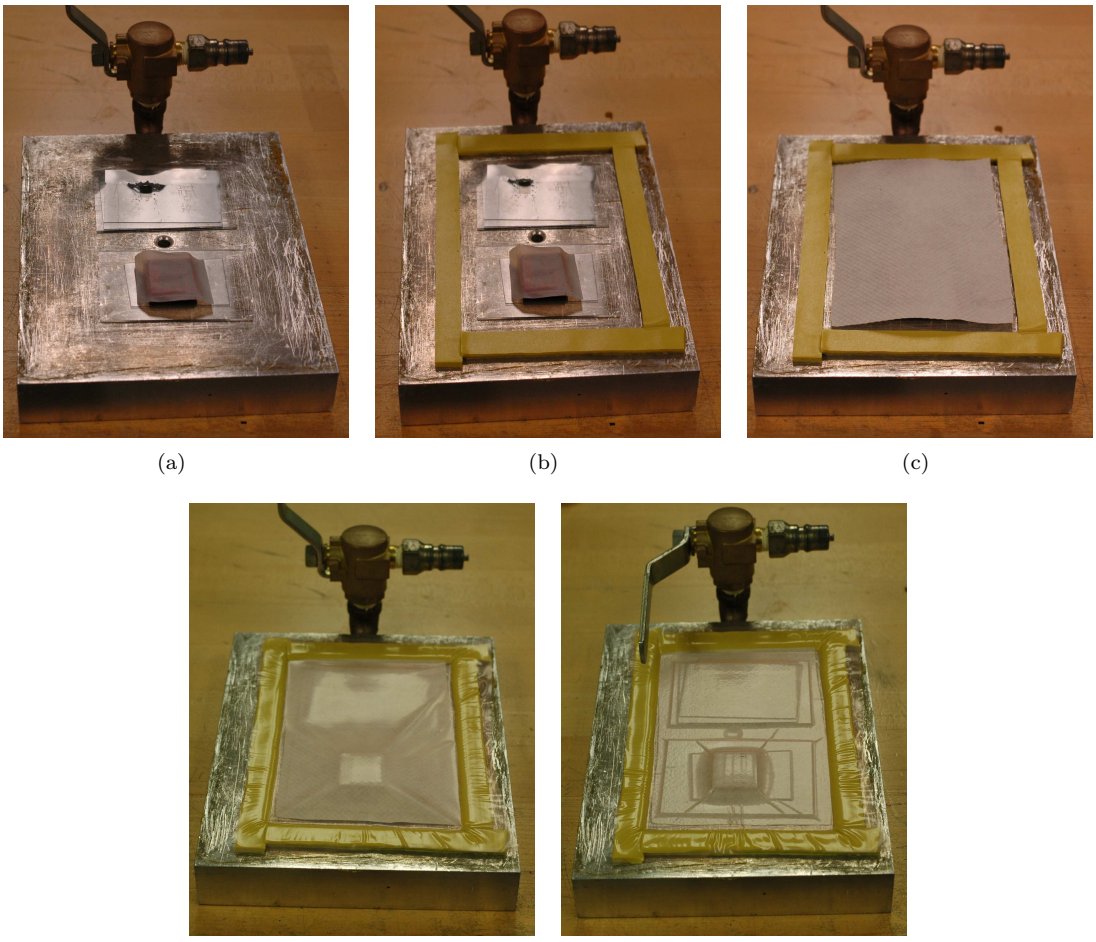

(a) (b) (c)

(d) (e)

Figure A.8: Vacuum bagging process detail

part. Along with following the recommended cure profile, peeling between the carbon fiber and Kapton is no longer observed. Also, though not quantitatively measured, carbon fiber cured in this manner has lower internal damping as seen through using it as an elastic layer of a piezoelectric bending actuator and observing the Q of the vibrational system.

A.5 Added Manufacturing Abilities

All the processes mentioned in this chapter yield greater speed and success rate in constructing composite flexure assemblies. In summary, using Kapton as a flexure layer allows the

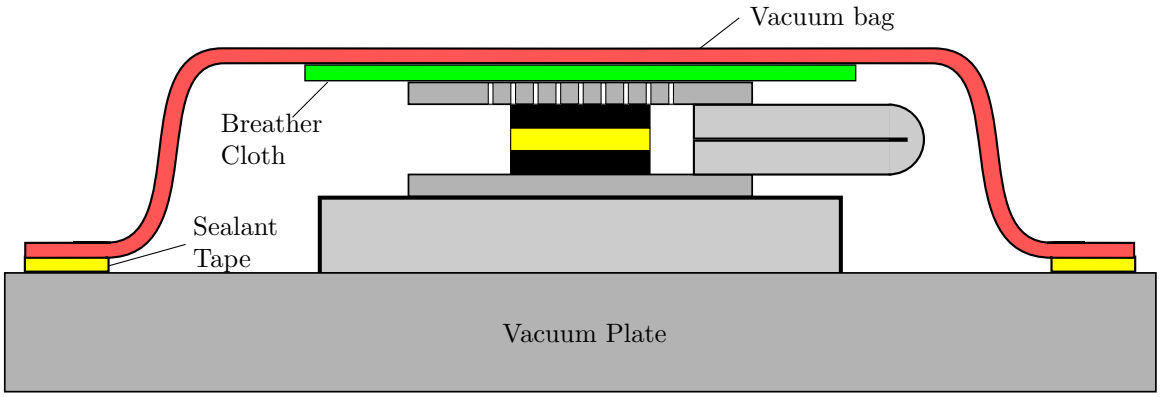

Figure A.9: Cross section of the vacuum bagging layup, shown assembled with a sample from the automated folding (see Fig. A.6).

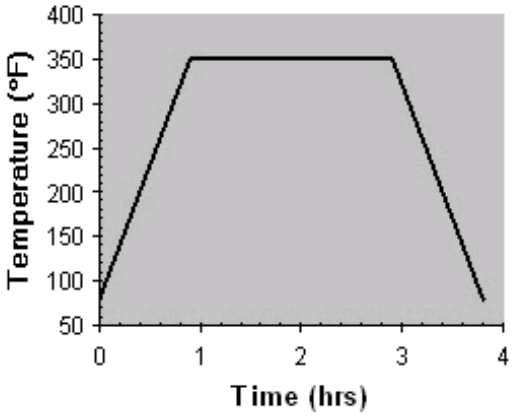

Figure A.10: Recommended cure profile for YLA RS-3C resin present in the UHM60J carbon fiber

carbon fiber to be cured at the recommended temperature so that resin bonding is strong and damping in the carbon fiber is low without damaging the flexure layer. Along with high temperature curing, vacuum bagging achieves strong bonding between the carbon fiber and the Kapton layer. Flexure peeling has been basically eliminated due to vacuum bagging, high temperature curing, and improved laser cutting processes. Automated folding eliminated misalignments in flexures, also increasing part yield significantly. Finally, it is interesting to note that vacuum bagging now allows molding of three dimensional composite parts. Using high temperature rubber as a mold (Dupont 3120 RTV Silicone Rubber), the carbon fiber can be shaped by being tightly held against the rubber mold by the vacuum bag. An example of this process is the curved side beams shown in

Chapter 5 and the dynamometer spring in Chapter 3.

Appendix B

Miniature Millirobot Control Board and Power Supplies

Many millirobots need some amount of control for operation, whether it be closed or open loop control. Considering the light weight of the robots and the desire for untethered mobility, off the shelf control boards are too heavy and consume too much power for use. A lightweight, low power control board is designed here first for use on the autonomous glider of [72] but modified later for millirobot control in general. The control board was made in a modular way so that different power supplies (for instance, a piezoelectric power supply or shape memory alloy power supply) could be easily integrated with the controller. The design of the controller is first described, followed by the design of two millirobot power supplies that attach to the control board.

B.1 Control Board

A block diagram of the control board is shown in Fig. B.1. It is centered around a PIC 8-bit 18LF2520 processor, chosen for its power efficiency, light weight (90mg), and internal oscillator. The processor is capable of 10MIPS using its internal oscillator at 40MHz. Signaling LEDs and a

manual switch were included with the processor for debugging and user interface.

Two other circuit sections were included in the control board with the processor, as shown in the diagram of Fig. B.2. The power conditioning section utilizes two 3.3V ZXCL330 regulators in light SC-70-5 packages, one for the processor and one available for a separate sensor power supply. It also incorporates an MN1382 battery supervisor to detect the battery voltage and signal when it is low. The third section of the circuit is for IR communication via the IrDA standard common in laptops and PDAs. Infrared communication (rather than RF communication) was chosen for its low power and light weight (no antenna).

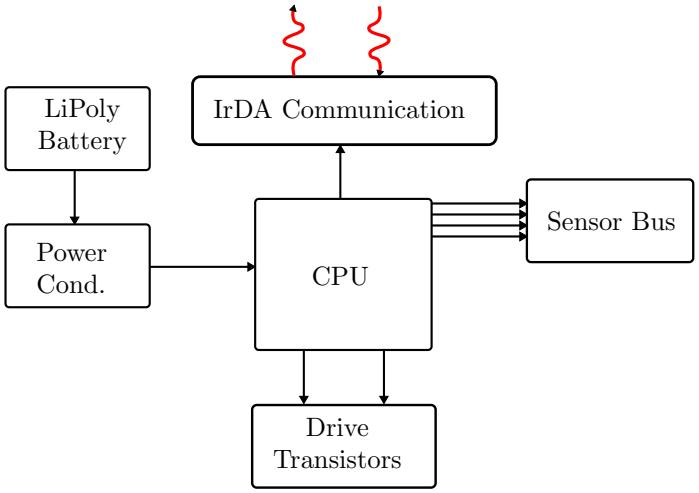

Figure B.1: Control electronics board block diagram.

A sensor bus and connector (with I2C communication, interrupts, A/D converters, and digital I/Os) were included in the manufacturing of the board so that sensor "daughter" cards could be developed and added. Daughter cards currently exist for a magnetic sensor (compass), a gyroscope, and an accelerometer. A power connector was included at the end of the board to attach a variety of power supplies, depending on the actuator technology of the millirobot. The manufactured board is shown in Fig. B.3 and weighs 440mg.

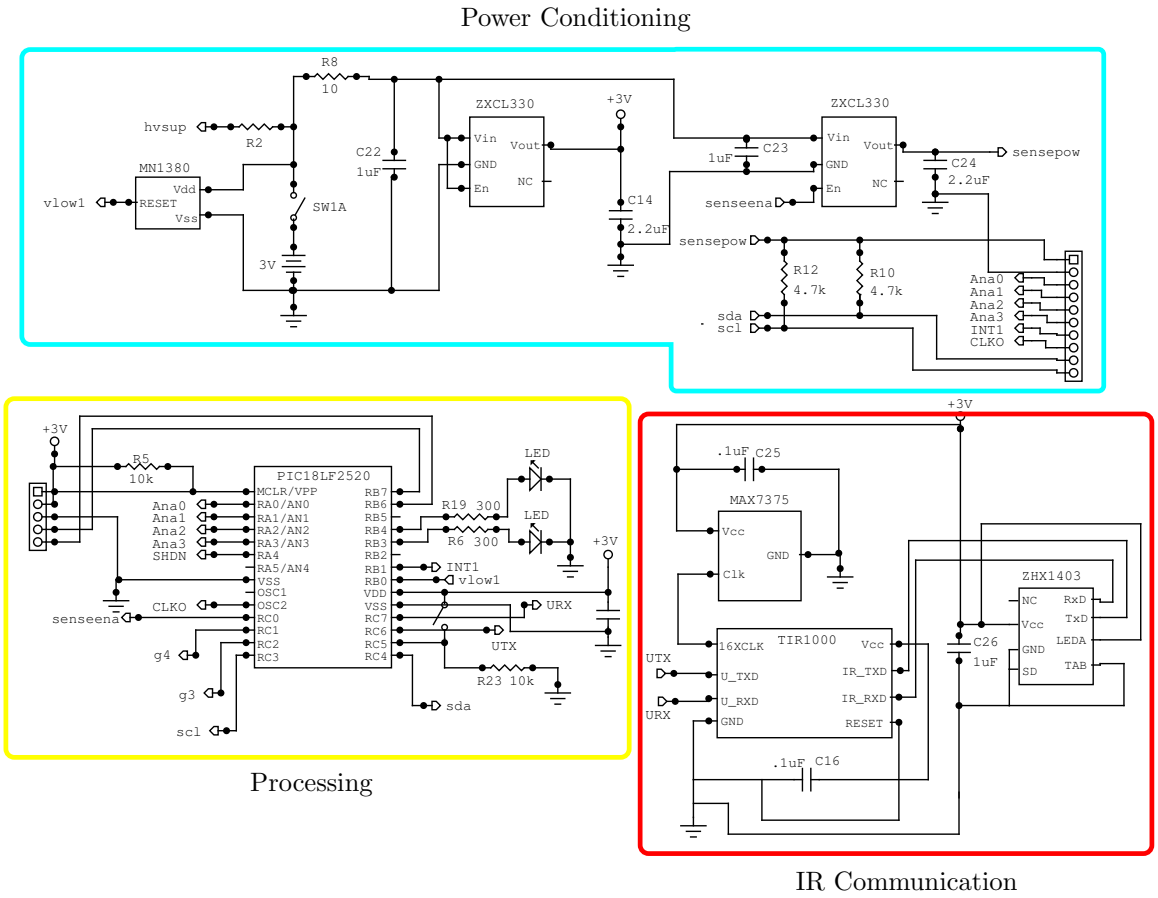

Figure B.2: Control board circuit schematic.

B.2 Piezoelectric High Voltage Power Supply

One disadvantage of using piezoelectric actuators is the high voltage required to drive them. This problem was addressed when making the autonomous microglider with piezoelectric steering actuators in [72]. The bending actuators for that vehicle required a 250V bias; the power source was a 3.7V lithium polymer battery. Analysis was performed by Steltz and Seemang to determine the best topology for this purpose in [56]. It was determined in that work that a hybrid boost converter/charge pump circuit was the best DC to DC converter technology for the application. A Linear Technology boost converter IC (LT1615-1) was combined with capacitors and diodes as shown in Fig. B.4 to achieve the 250V bias.

The efficiency, weight, and power output of the converter are all dependent on the capaci-

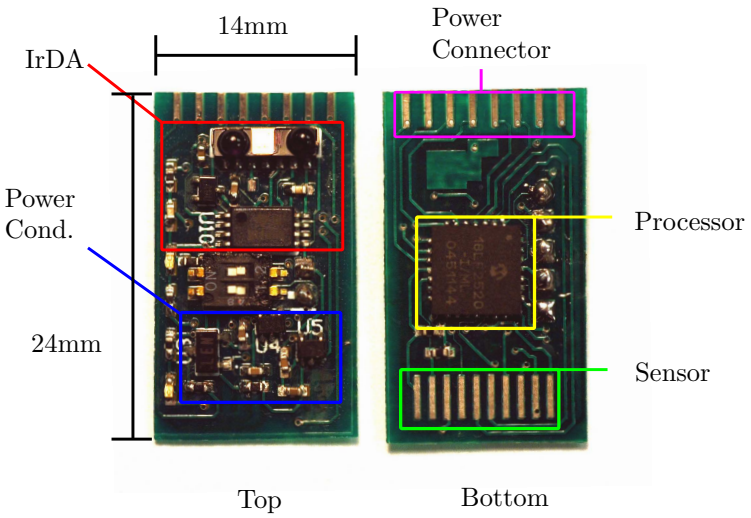

Figure B.3: Top and bottom of the control electronics PC board.

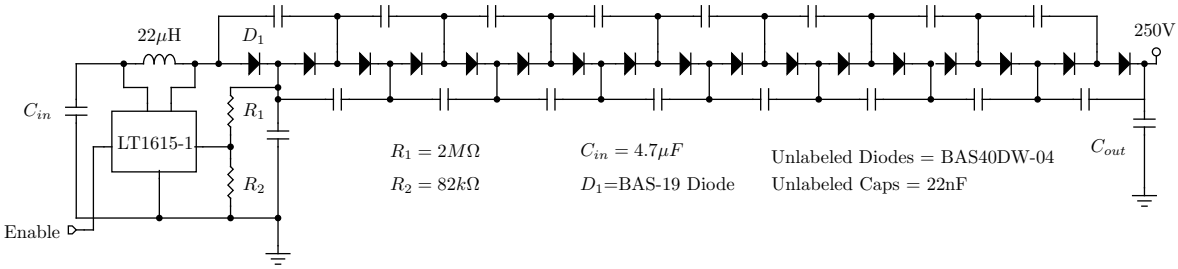

Figure B.4: Hybrid piezoelectric power supply circuit. C_{out} is an application specific component depending on capacitance of the actuator being driven along with the tolerable bias droop.

tance of the small surface mount capacitors in the design. A converter was constructed and tested using 0402 22nF capacitors (the largest value 0402 capacitors capable of withstanding 50V); its efficiency is experimentally plotted in Fig. B.5. Also plotted is the predicted efficiency of the circuit using the analysis in [52] and the predicted efficiency and power output if 0603, 220nF capacitors are used. Since only two very small piezoelectric bending actuators are used on the glider for which this converter was designed, 0402 capacitors provided enough power output.

The high voltage converter was built on one side of a two sided custom pc board with a 1 mil thick FR4 fiberglass core and appears in Fig. B.6. The top side of the board contains all the electronics for the 250V bias; the bottom side contains two channels of the drive circuitry in Fig.

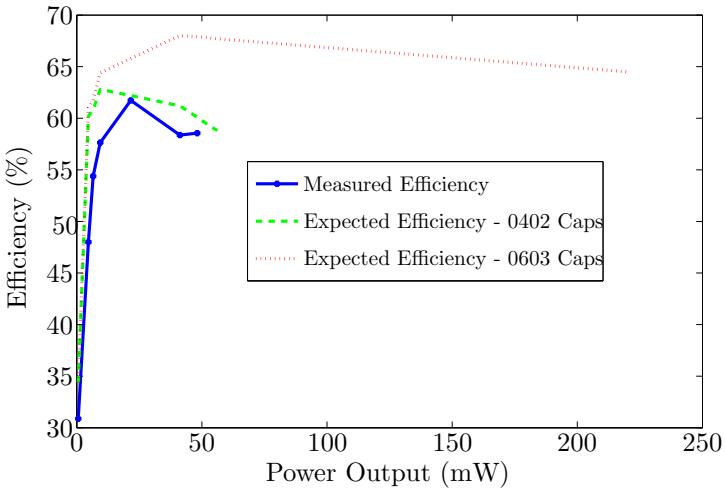

Figure B.5: Efficiency of miniature piezoelectric power supply.

B.7. The drive circuitry uses several high voltage transistors (Supertex TN2124 NMOS and Zetex FMMT558 PNP). All resistor values are chosen based on the necessary drive bandwidth and the capacitance of the actuator. The entire populated board weighs only 427mg. It interfaces to the control board via PWM to drive two piezoelectric actuators independently.

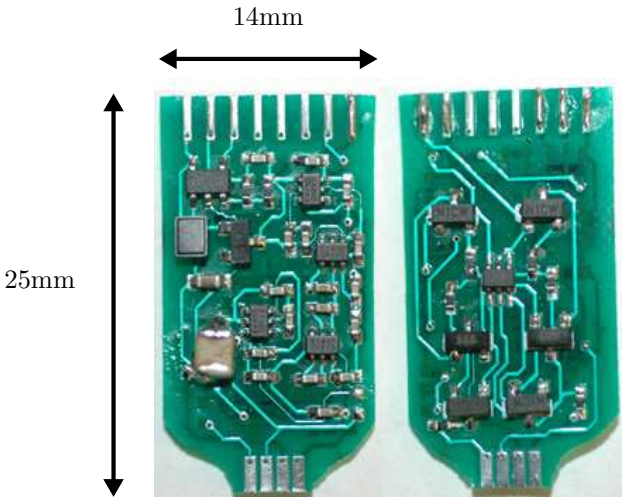

Figure B.6: Miniature piezoelectric power supply.

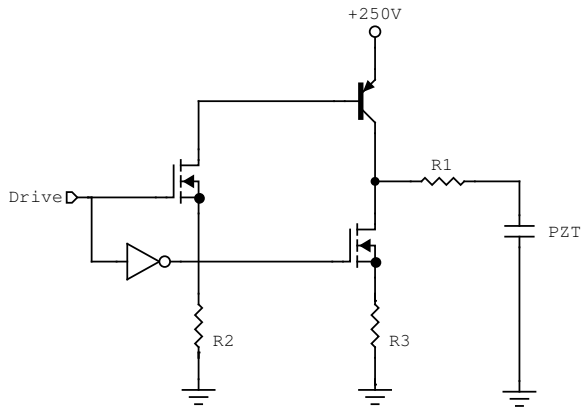

Figure B.7: Piezoelectric drive circuitry.

B.3 Shape Memory Alloy Power Supply

Another power supply to drive shape memory alloy wires was needed for use on the crawling robot in [27]. The same control board was used on the robot as has been previously described; the SMA power supply however was specifically created for this robot. The power supply was designed to drive a variety of sizes of SMA wire; the most difficult to drive wires are those that are high resistance, notably 1 mil diameter Flexinol wire because the battery voltage must be boosted to achieve proper current levels. Knowing that a maximum of 60mA is needed through a 200 Ω maximum resistance (for each of the two channels), the maximum voltage needed for the converter is 12V and it must be able to produce a maximum of 1.44W output power.

A standard boost converter topology was adopted using a Linear Technology LT3580 boost converter IC and a lightweight inductor (Coilcraft LPS4018) that only weighs 97mg but can handle up to 0.86A with only a 10% inductance drop. The converter was manufactured like the control and piezoelectric power supply board on a 1 mil core, double sided FR4 pc board shown in Fig. B.8.

The populated power supply board weighs only 340mg and interfaces to the control board discussed earlier to independently control two channels of SMA wire. The output voltage was set to 13.6V; the converter's efficiency was tested at two different IC switching frequencies as shown in Fig. B.9. The higher switching frequency is less efficient as is expected; however if very high powers

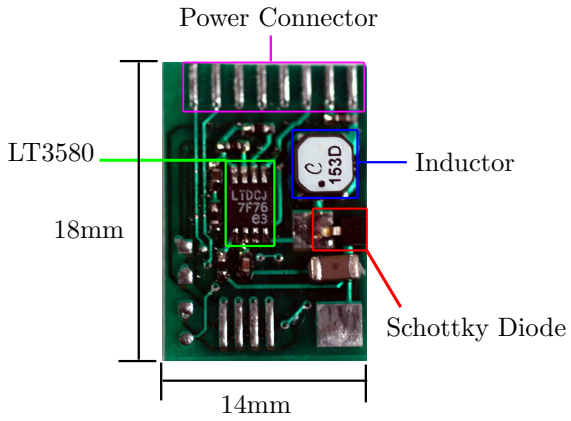

Figure B.8: Miniature boost converter pc board.

are necessary (>1.5W) the high switching frequency converter is more stable and was used on the RoACH crawling robot.

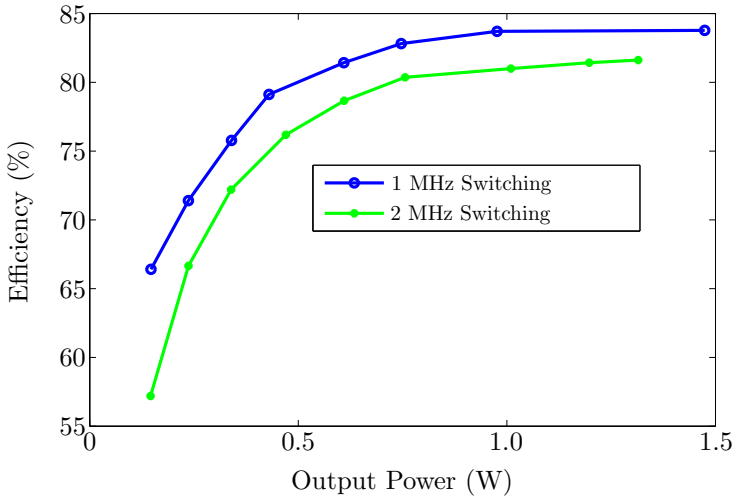

Figure B.9: Miniature power supply efficiency for 1MHz and 2MHz switching frequencies.

The shape memory alloy wire was driven through an NMOS transistor via PWM from the control board; the simple drive circuit is shown in Fig. B.10. A sensing resistor R_{sens} can be used for precise current control through an A/D of the control processor. Losses in this resistor are kept low by making the resistance value much smaller than the resistance of the shape memory alloy

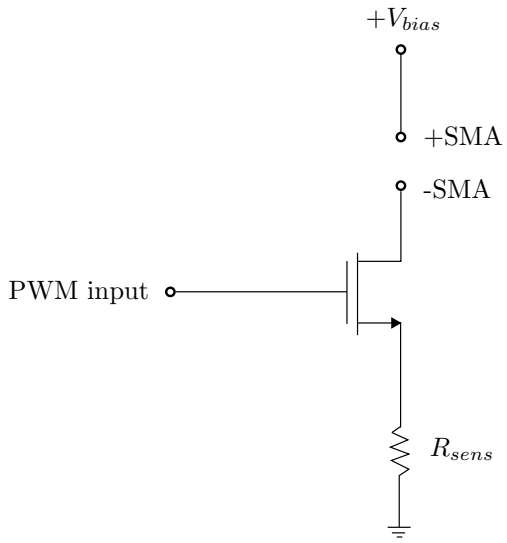

Figure B.10: Transistor drive scheme for SMA.

(typically 1 Ω for the sensing resistor vs on the order of 100 Ω for the shape memory alloy wire).

B.4 Conclusion

Although a custom ASIC for control and power electronics for a millirobot would be the lightest and most efficient solution, the PC board discussed here with different power supplies is a lightweight and flexible solution that can quickly and inexpensively add some level of autonomy to a mobile millirobot.

Bibliography

[1] A.N. Ahn, K. Meijer, and R.J. Full. In situ muscle power differs without varying in vitro mechanical properties in two insect leg muscles innervated by the same motor neuron. *J. Exp. Biol.*, 209:3370–3382.

[2] S. Avadhanula. *Design, Fabrication and Control of the Micromechanical Flying Insect.* PhD thesis, University of California, Berkeley, 2006.

[3] S. Avadhanula and R.S. Fearing. Flexure design rules for carbon fiber microrobotic mechanisms. In *IEEE Int. Conf. on Robotics and Automation*, 2005.

[4] Y. Bar-Cohen, editor. *Electroactive Polymer (EAP) Actuators as Artificial Muscles: Reality, Potential, and Challenges.* SPIE - The Int. Soc. for Optical Eng., 2001.

[5] Y. Bar-Cohen. Electroactive polymers (EAP) as actuators for potential future planetary mechanisms. In *Proceedings of the NASA/DoD Conf. on Evolution Hardware*, 2004.

[6] M.G. Borgen, G.N. Washington, and G.L. Kinzel. Design and evolution of a piezoelectrically actuated miniature swimming vehicle. *IEEE/ASME Transactions on Mechatronics*, 8:66–76, 2003.

[7] N. Bradshaw and D. Lentink. Aerodynamic performance of a bio-inspired flapping micro air vehicle with flexible wings. *Comparative Biochemistry and Physiology - Part A: Molecular and Integrative Physiology*, 146, 2007.

[8] G. Caprari, T. Estier, and R. Siegwart. Fascination and down scaling - Alice the sugar cube robot. *J. of Micromechatronics*, 1:177–189, 2002.

[9] P. Chai and D. Millard. Flight and size constraints: Hovering performance of large hummingbirds under maximal loading. *J. Exp. Biol.*, 200:2757–2763, 1997.

[10] A. Cox, D. Monopoli, D. Cveticanin, M. Goldfarb, and E. Garcia. The development of elastodynamic components for piezoelectrically actuated flapping micro-air vehicles. *J. of Intelligent Material Systems and Structures*, 13:611–615, 2002.

[11] M.H. Dickinson, C.T. Farley, R.J. Full, M.A.R Koehl, R. Kram, and S.Lehman. How animals move: An integrative view. *Science*, 288:100–106, 2000.

[12] M.H. Dickinson, F. Lehmann, and S.P. Sane. Wing rotation and the aerodynamic basis of insect flight. *Science*, 284:1954–1960, June 18 1999.

[13] A. Dogan, J.F. Fernandez, K. Uchino, and R.E. Newnham. The "cymbal" electromechanical actuator. In *Proc. of the Tenth IEEE Int. Symposium on Applications of Ferroelectrics*, 1996.

[14] R. Dudley. *The Biomechanics of Insect Flight.* Princeton University Press, 2000.

[15] T. Ebefors, J.U. Mattsson, E. Kalvesten, and G. Stemme. A walking silicon micro-robot. In *IEEE 10th Intl Conf on Solid-State Sensors and Actuators*, 1999.

[16] J. Eckerle, J.S. Stanford, J. Marlow, Roger Schmidt, S. Oh, T. Low, and V. Shastri. A biologically inspired hexapedal robot using field-effect electroactive elastomer artificial muscles. In *Proc. SPIE, Smart Structures and Materials 2001: Industrial and Commercial Applications of Smart Structures Technologies*, volume 4332, 2001.

[17] C.P. Ellington, C. Van den Berg, A.P. Willmott, and A.L.R. Thomas. Leading-edge vortices in insect flight. *Nature*, 384:626–630, 1996.

[18] A.H. Epstein. Millimeter-scale, MEMS gas turbine engines. In *ASME Turbo Expo*, 2003.

[19] A.C. Fernandez-Pello, A.P. Pisano, K. Fu, D.C. Walther, A. Knobloch, F. Martinez, M. Senesky, D. Jones, C. Stoldt, and J. Heppner. Mems rotary engine power system. In *Int. Workshop on Power MEMS*, 2002.

[20] A.M. Flynn and S.R. Sanders. Fundamental limits on energy transfer and circuit considerations for piezoelectric transformers. *IEEE Transactions on Power Electronics*, 17:8–14, 2002.

[21] T. Fukushima, K. Asaka, A. Kosaka, and T. Aida. Fully plastic actuator through layer-by-layer casting with ionic-liquid-based bucky gel. *Angew. Chem.*, 117:2462–2465, 2005.

[22] R.J. Full. *Invertebrate locomotor systems, in Handbook of Physiology Section 13: Comparative Physiology*. Oxford Univ. Press, 1997.

[23] R.J. Full and M.S. Tu. Mechanics of six-legged runners. *J. Exp. Biol.*, 148:129–146, 1990.

[24] M. Goldfarb, M. Gogola, G. Fischer, and E. Garcia. Development of a piezoelectrically-actuated mesoscale robot quadraped. *J. of Micromechatronics*, 1:205–219, 2002.

[25] G. H. Haertling. Rainbow actuators and sensors: a new smart technology. In *Proceedings of the SPIE - Smart Structures and Materials 1997: Smart Materials Technologies*, 1997.

[26] S. Hollar, A. Flynn, C. Bellew, and K.S.J. Pister. Solar powered 10mg silicon robot. In *IEEE Int. Conf. on MEMS*, 2003.

[27] A. Hoover, E. Steltz, and R.S. Fearing. RoACH: An autonomous 2.4g crawling hexapod robot. In *In Review: IEEE Int. Conf. on Intelligent Robots and Systems*, 2008.

[28] L.L. Howell. *Compliant Mechanisms*. John Wiley and Sons, Inc., 2001.

[29] http://home.comcast.net/ gordon johnson/mmidget.htm.

[30] http://micro.seas.harvard.edu/.

[31] http://www.bsdmicrorc.com.

[32] http://www.cedrat.com.

[33] http://www.delfly.nl.

[34] http://www.didel.com.

[35] http://www.dynalloy.com.

[36] http://www.microbrushless.com.

[37] http://www.piezo.com.

[38] Burleigh Instruments. The technology behind Burleigh inchworm systems. Technical report, Burleigh Instruments, Fishers, NY, 1998.

[39] N. Kamamichi, M. Yamakita, K. Asaka, and Z. Luo. A snake-like swimming robot using ipmc actuator/sensor. In *IEEE Int. Conf. on Robotics and Automation*, 2006.

[40] Y. Kawamura, S. Souda, S. Nishimotor, and C.P. Ellington. *Bio-mechanisms of Swimming and Flying: Fluid Dynamics, Biomimetic Robot, and Sports Science*, chapter 26: Clapping-wing Micro Air Vehicle of Insect Size, pages 319–330. Springer, 2008.

[41] B. Lambrecht, A. Horchler, and R. Quinn. A small, insect-inspired robot that runs and jumps. In *IEEE Int. Conf. on Robotics and Automation*, pages 1240–1245, 2005.

[42] K. Meijer, M. Rosenthal, and R.J. Full. Muscle-like actuators? a comparison between three electroactive polymers. In Y. Bar-Cohen, editor, *Smart Structure and Materials 2001: Electroactive Polymer Actuators and Devices. Proc. SPIE*, volume 4329, pages 7–15, 2001.

[43] C.D. Near. Piezoelectric actuator technology. In *Proc. of the Smart Struct. and Mat. Conf*, volume 2717, 1996.

[44] C. Niezrecki, D. Brei, S. Balakrishnan, and A. Moskalik. Piezoelectric actuation: State of the art. *The Shock and Vibration Digest*, 33:269–280, 2001.

[45] K. Onitsuka, A. Dogan, J.F. Tressler, Q. Xu, S. Yoshikawa, and R.E. Newnham. Metal-ceramic composite transducer, the "Moonie". *J. of Intelligent Material Systems and Structures*, 6:447–455, 1995.

[46] S. Park and T.R. Shrout. Ultrahigh strain and piezoelectric behavior in relaxor based ferroelectric single crystals. *J. Appl. Phys.*, 82:1804–1811, 1997.

[47] J.S. Plante and S. Dubowsky. On the properties of dielectric elastomer actuators and its implications for their design. *J. of Smart Materials and Structures*, 16:227–236, 2007.

[48] R. Pomirleanu and V. Giurgiutiu. High-field characterization of piezoelectric and magnetostrictive actuators. *J. of Intelligent Matl. Sys. and Struct.*, 15:161–180, 2004.

[49] T.N. Pornsin-Sirirak, Y.C. Tai, C.H. Ho, and M. Keennon. Microbat - a palm-sized electrically powered ornithopter. In *NASA/JPL Workshop on Biomorphic Robotics*, 2001.

[50] L.C. Rome and D. Swank. The influence of temperature on power output of scup red muscle during cyclical length changes. *J. Exp. Biol.*, 171:261–281, 1992.

[51] R. Sahai, E. Steltz, S. Avadhanula, R.J. Wood, and R.S. Fearing. Towards a 3g crawling robot through the integration of microrobot technologies. In *IEEE Int. Conf. on Robotics and Automation*, 2006.

[52] M. Seeman and S. Sanders. Analysis and optimization of switched-capacitor dc-dc converters. In *IEEE Workshops on Computers in Power Electronics (COMPEL)*, pages 216–224, 2006.

[53] M. Shahinpoor and K.J. Kim. Ionic polymer-metal composites: I. Fundamentals. *Smart Mater. Struct.*, 10:819–833, 2001.

[54] R. Shankar, T. K. Ghosh, and R.J. Spontak. Dielectric elastomers as next-generation polymeric actuators. *Soft Matter*, 3:1116–1129, 2007.

[55] E. Steltz, S. Avadhanula, and R.S. Fearing. High lift force with 275Hz wing beat in MFI. In *IEEE Int. Conf. on Intelligent Robots and Systems*, 2007.

[56] E. Steltz, M. Seeman, S. Avadhanula, and R.S. Fearing. Power electronics design choice for piezoelectric microrobots. In *IEEE/RSJ Int. Conf. on Intelligent Robots and Systems*, 2006.

[57] E. Steltz, R.J. Wood, S. Avadhanula, and R.S. Fearing. Characterization of the micromechanical flying insect by optical sensing. In *IEEE Int. Conf. on Robotics and Automation*, 2005.

[58] R.D. Stevenson and Robert K. Josephson. Effects of operating frequency and temperature on mechanical power output from moth flight muscle. *J. Exp. Biol.*, 149:61–78, 1990.

[59] Y. Sugawara, K. Onitsuka, S. Yoshikawa, Q. Xu, R.E. Newnham, and K. Uchino. Metal-ceramic composite actuators. *J. of the American Ceramic Society*, 75:996–998, 1992.

[60] K. Uchino, J. Zheng, A. Joshi, Y. Chen, and S. Yoshikawa. High power characterizatin of piezoelectric materials. *J. of Electroceramics*, 2:33–40, 1998.

[61] J. Ueda, T. Secord, and H.H. Asada. Design of pzt cellular actuators with power-law strain amplification. In *Proceedings of the 2007 IEEE/RSJ Int. Conf. on Int. Robots and Systems*, 2007.

[62] J.W. Waanders. *Piezoelectric Ceramics - Properties and Applications*. Philips Components, Marketing Communications, 1991.

[63] Q. Wang, Q. Zhang, B. Xu, R. Liu, and L.E. Cross. Nonlinear piezoelectric behavior of ceramic bending mode actuators under strong electric fields. *J. Appl. Physics*, 86:3352–3360, 1999.

[64] T. Waram. *Actuator Design Using Shape Memory Alloys*. 1993.

[65] T. Weis-Fogh. *Dimensional analysis of hovering flight. In Scale Effects in Animal Locomotion*. London: Academic Press, 1977.

[66] R.J. Wood. Design, fabrication, and analysis of a 3DOF, 3cm flapping wing MAV. In *IEEE/RSJ Int. Conf. on Intelligent Robots and Systems*, 2007.

[67] R.J. Wood. Liftoff of a 60mg flapping-wing MAV. In *IEEE/RSJ Int. Conf. on Intelligent Robots and Systems*, 2007.

[68] R.J. Wood and E. Steltz and. Nonlinear performance limits for high energy density piezoelectric bending actuators. In *Int. Conf. on Robotics and Automation*, 2005.

[69] R.J. Wood, S. Avadhanula, M. Menon., and R.S. Fearing. Microrobotics using composite materials: The micromechanical flying insect thorax. In *IEEE International Conference on Robotics and Automation*, pages 1842–1849, Taiwan, 2003.

[70] R.J. Wood, S. Avadhanula, R. Sahai, E. Steltz, and R.S. Fearing. Microrobot design using fiber reinforced composites. *J. Mechanical Design*, 130:052304, 2007.

[71] R.J Wood, S. Avadhanula, E. Steltz, M. Seeman, J. Entwistle, A. Bachrach, G. Barrows, S. Sanders, and R.S. Fearing. Design, fabrication and initial results of a 2g autonomous glider. In *The 31st Annual Conference of the IEEE Industrial Electronics Society*, 2005.

[72] R.J. Wood, S. Avadhanula, E. Steltz, M. Seeman, J. Entwistle, A. Bachrach, G. Barrows, S. Sanders, and R.S. Fearing. Enabling technologies and subsystem integration for an autonomous palm-sized glider. *IEEE Robotics and Automation Magazine*, 14:82–91, 2007.

[73] R.J Wood, E. Steltz, and R.S. Fearing. Optimal energy density piezoelectric bending actuators. *Sensors and Actuators A*, 119/2:476–488, 2004.

[74] J. Yan, S. Avadhanula, J. Birch, M.H. Dickinson, M. Sitti, T. Su, and R.S. Fearing. Wing transmission for a micromechanical flying insect. *J. of Micromechatronics*, 1:221–238, 2002.

[75] A. Yumaryanto, J. An, and S. Lee. A cockroach-inspired hexapod robot actuated by LIPCA. In *IEEE Conf. on Robotics, Automation, and Mechatronics*, 2006.